Modélisation de lentilles gravitationnelles et designs optiques non-obstrués pour les sondages grands champs

Balasubramanian Singaravelu

Université de Toulouse

THÈSE

En vue de l'obtention du

DOCTORAT DE L'UNIVERSITÉ DE TOULOUSE

Délivré par :

Université Toulouse 3 Paul Sabatier (UT3 Paul Sabatier)

Présentée et soutenue par :

BALASUBRAMANIAN SINGARAVELU

Le 3 Novembre 2014

Titre :

Modélisation de lentilles gravitationnelles et Design de télescopes non-obstrués pour les sondages grands champs

---

ED SDU2E : Astrophysique, Sciences de l'Espace, Planétologie

Unité de recherche :

Institut de recherche en astrophysique et planétologie (IRAP)

Directeur(s) de Thèse :

Rémi CABANAC (Astronome Adjoint, IRAP)
Geneviève SOUCAIL (Astronome, IRAP)

Rapporteurs :

Jean-Paul KNEIB (Professeur, EPFL, Suisse)
David VALLS-GABAUD (DR CNRS, Observatoire de Paris-Meudon)

Autre(s) membre(s) du jury :

Alain BLANCHARD (Professeur Université de Toulouse 3 Paul Sabatier)
Leon KOOPMANS (Associate Professor, Univerté de Gronigen)

Gravitational Lens Modelling And Unobstructed Telescopes For Wide Field Surveys

Balasubramanian Singaravelu

Résumé

Les lentilles gravitationnelles fortes sont des sondes importantes pour étudier la cosmologie, et l'univers extragalactique, mais la modélisation des lentilles gravitationnelles est un problème inverse complexe. Dans une première partie nous étudions une nouvelle méthode d'inversion des arcs gravitationnels pour déduire les caractéristiques physiques des objets physiques. Habituellement, dans la modélisation de lentilles gravitationnelles, la lentille d'avant-plan est décrite par un modèle paramé--trique, alors que la source d'arrière-plan n'est modélisée que par sa position et son flux. Dans ce travail, Nous améliorons l'approche paramétrique existante en modélisant en même temps la lentille et la source par des modèles paramétriques. Nous utilisons un modèle d'ellipsoïde isotherme non singulière (NIE en anglais) pour décrire les lentilles et un modèle de Sersic pour la source. Notre méthode est d'abord vérifiée sur simulations. Elle donne des résultats rigoureux sur des arcs simulés. Nous appliquons ensuite notre méthode à des données réelles à haut rapport signal-à-bruit: un sous-ensemble du Strong Lensing Legacy Survey (SL2S) et du Sloan Lensing ACS Survey (SLACS). Nous présentons ici les caractéristiques physiques des lentilles et sources que nous avons obtenus avec notre méthode d'inversion. A partir de ces objets, nous étudions la distribution de la matière noire aux échelles des halos de galaxies et la morphologie des sources à redshift élevé. Nous trouvons que la fraction de matière sombre à l'intérieur du rayon Einstein est de 20%±8. Nous pouvons également contraindre pour la première fois la fraction de masse présente dans le coeur des lentilles mésurées de l'ordre de 5%±2.

Dans une deuxième partie, nous étudions les caractéristiques optiques de télescopes hors-axes en vue de leur application pour des projets spatiaux demandant une qualité d'image à très haute résolution sur de grands champs (par exemple la mesure d'effets de lentille faible). Les télescopes présentant une pupille non-obstruée (optique hors-axe) sont connus pour fournir des fonctions d'étalement ponctuelles (PSF de l'anglais Point spread function) piquées et "propres" dans leur plan focal, contrairement

aux télescopes traditionnels présentant une obstruction de leur pupille (par exemple les types Cassegrain, Ritchey-Chrétien). Les progrès récents dans la fabrication et l'assemblage de surfaces asphériques favorise télescopes non-obstrués sur les télescopes obstruées, au moins en théorie. Dans ce travail, nous comparons quantitativement la qualité d'image de deux designs optique à trois miroirs (en anglais Three Mirror Anastigmat TMA), un design non-obstrué et un design obstrué. Les deux modèles ont le même miroir primaire, la même longueur focale, le même champ de vue et les mêmes détecteurs. Nous construisons des simulations réalistes de galaxies pour tester la performance des deux designs. Nous démontrons que les deux les designs peuvent mesurer les caractéristiques morphologiques observables en jeu dans les effets de lentille faible avec la même précision. Dans le cas du design obstrué cette performance est atteinte uniquement si la PSF est reconstruite à moins de 12 minutes d'arc de la galaxie mesurée. Dans le cas du design non-obstrué, cette précision optimale est atteinte même si la PSF est reconstruite à plus de 50 minutes d'arc de la galaxie mesurée. Finalement, nous discutons les avantages et inconvénients des designs respectifs.

Abstract

Strong gravitational lenses are an important probe to study the cosmology of the extragalactic universes but gravitational lens modelling is an ill–posed problem. Usually in gravitational lens modelling the lens is described using a parametric model but the background source is not. We improve the existing parametric approach by modelling both the lens and the source using a parametric model. We use a non-singular isothermal ellipsoid model to describe the lens and a Sérsic light profile to describe the source. Our method yields rigorous results on simulated gravitational arcs. We also applied our method to a set of high S/N gravitational arcs in the SL2S and SLACS database. We present the lens and source parameters we obtained for these lenses. Using these parameters we study the distribution of dark matter in galaxy scale halos and the morphology of high redshift sources. We find the fraction of dark matter within the Einstein radius to be 0.2 ± 0.08 and the lens mass present in the core is in the order of $5\pm2\%$.

Telescopes with unobstructed pupil are known to deliver clean point spread function (PSF) to their focal plane, in contrast to traditional telescopes with obstructed pupil. Recent progress in the manufacturing aspheric surfaces and mounting accuracy favors unobstructed telescopes over obstructed telescopes for science cases that demand stable and clean PSF over the entire field–of–view. We compare the image quality of an unobstructed Three–Mirror–Anastigmat (TMA) design with that of an obstructed TMA. Both the designs have the same primary mirror, effective focal length, field–of–view and detector characteristics. We demonstrate using simulated images of faint elliptical galaxies imaged through the two designs, that both the designs can measure weak lensing observables with same precision, if the PSF is reconstructed within 12 arc-minutes from the source. We also demonstrate that, the unobstructed design delivers desirable precision even if the PSF is reconstructed 50 arc-minutes away from the source.

Contents

List of Figures

List of Tables

Part I

Introduction

Chapter I.1

Introduction en Français

Le but de notre travail est d'améliorer les méthodes disponibles pour étudier l'univers extragalactique en utilisant l'effet de lentille gravitationnelle. Nous nous adressons à deux défis à relever dans études lenticulaires. Par souci de clarté, la thèse est divisée en trois parties. La première partie est une revue de la cosmologie contemporaine dite de concordance et les objectifs de notre travail, la partie II est liée à la modélisation lentilles fortes et de la partie III est liée à la mesure de précision de l'effet de lentilles faibles observables.

Effet de lentille gravitationnelle

La gravité newtonienne et la relativité générale d'Einstein prédisent que le chemin de lumière se dévie en présence d'une masse ou d'un champ gravitationnel.Einstein (1936) a calculé la valeur correcte de l'angle de détection et a montré que la lumière d'une étoile d'arrière-plan sera détecté par une étoile de premier plan dans un anneau lumineux si les étoiles et observateur sont alignés. Einstein a noté que ce phénomène ne peut jamais être observé car la probabilité d'un tel alignement est rare. Plus tard Zwicky (1937) a souligné que la probabilité de trouver des galaxies d'avant-plan la détection de la lumière des galaxies d'arrière-plan est dans les limites d'observation de l'astronomie. Ce phénomène est maintenant connu sous le nom de lentille gravitationnelle.

Zwicky (1937) a proposé que l'effet de lentille gravitationnelle peut être utilisé comme un outil pour trouver la masse totale (stellaire + de matière noire) de galaxies et des amas. Plus tard Refsdal (1964) a dérivé l'équation des lentilles (minces) et a montré que l'effet de lentille gravitationnelle peut également être utilisé pour déterminer la constante de Hubble à partir des mesures de délai temporel entre plusieurs images de la même source. En fonction de la position de l'observateur, la lentille (masse d'avant-plan) et la source de fond, l'effet de lentille est divisée en deux catégories. Les lentilles fortes et les lentilles faibles (cf. Blanford and Narayan, 1992).

Lentilles fortes

Si l'observateur, la lentille et la source sont colinéaires. Les lentilles gravitationnelles (galaxies massives ou groupes de galaxies) imagent les sources ponctuelles d'arrière-plan (quasars) en plusieurs images et les sources étendues (galaxies) en arcs allongés (ou anneaux). Ce type de lentille est appelée lentille forte. Le premier quasar lentille forte a été découvert par Walsh et al. (1979). Ce quasar (QSO 09571+561) est magnifié en deux images distantes de 5,7 secondes d'arc par une galaxie elliptique intermédiaire. Le premier arc gravitationnel allongé a été découvert indépendamment par Lynds and Petrosian (1986) et Soucail (1987) dans l'amas de galaxies Abell 370.

Dans la modélisation des lentilles fortes, le problème direct consiste à trouver les images d'une source de fond magnifiée par une lentille gravitationnelle donnée. Le problème inverse consiste à trouver la distribution de masse de la lentille, le profil de lumière et la position de la source à partir des mirages gravitationnels observés. Le problème direct est bien posé, puisqu'une solution unique existe. En revanche, le problème inverse est mal posé, il existe une infinité de solution et sa résolution pose plusieurs défis. Afin d'obtenir une solution du problème inverse, on procède généralement en deux étapes; une étape de reconstruction de source et une étape de reconstruction de l'image magnifiée de cette source. Finalement, l'ensemble des images reconstruites est comparé à l'image observée et la sélection de la reconstruction la plus probable se fait part inférence. L'inférence statistique nous

sert à trouver à la fois le profil de masse de la lentille et le profil de lumière de la source.

Dans le passé les images basse résolution et de faible profondeur ne permettaient pas de reconstruire à la fois les lentilles et les sources. En effet, dans les arcs gravitationnels observés à l'époque, en raison du bruit et de la faiblesse intrinsèque des sources de fond, la partie extraite d'un arc ne constituait qu'une sous-partie de la source. Lorsque des méthodes de reconstruction de source étaient appliquées à ces sous-parties extraites des arcs, seulement une sous-partie des sources était reconstruite dans le plan des sources. Ces pseudo-sources reconstruites étaient en réalité des distributions aléatoires de pixels (ou chaque pixels pouvaient être considérées comme une source ponctuelle dans le plan de la source). La qualité des données observées ne permettaient donc pas de déduire un modèle physique des sources magnifiées à partir des arcs reconstruits.

Au cours des dernières années les images du télescope spatial Hubble (HST) des lentilles connues ont produit des arcs avec une résolution plus élevée et un meilleur rapport signal-à-bruit. La qualité de ces images permet de commencer à modéliser les sources en conjonction avec les lentilles. Dans cette thèse, nous développons une méthode originale pour modéliser les lentilles et les sources de façon en parallèle. Nous appliquons notre méthode à un ensemble d'arcs gravitationnels observés pour obtenir une meilleure compréhension du profil de masse des galaxies lentille et des sources à grand redshift.

Lentilles faibles

Si les sources d'arrière-plan ne sont pas colinéaires avec l'observateur et la lentille, elles sont légèrement distordues en petits arcs au lieu d'être démultipliées en arcs allongés. Ce phénomène est appelé "effet de lentille faible" et a été étudié de façon pionnière par Tyson et al. (1990) dans l'amas Abell 1689 et CL 1490 + 52. Au cours de ces dernières années, les lentilles faibles ont été utilisées pour sonder l'évolution de la matière sombre dans les galaxies.

Si une population faible et lointaine de galaxies est observée à travers une lentille

gravitationnelle, la morphologie des galaxies d'arrière-plan est déformée par le champ gravitationnel de la lentille et le "grossissement" associé à lentille gravitationnelle modifie la luminosité apparente des sources d'arrière-plan. Si la forme intrinsèque d'une galaxie d'arrière-plan était connue, elle pourrait être utilisée pour calculer le champ de gravité local responsable de sa déformation et de son agrandissement. Malheureusement, la forme intrinsèque de la galaxie d'arrière-plan est une inconnue, de sorte que le champ gravitationnel local ne peut être étudiée qu'en effectuant ces mesures de façon statistique sur un échantillon de galaxies sélectionnées dans un domaine choisi, en supposant que les propriétés moyennes de cet échantillon sont connues.

L'un des importants paramètres observables de l'effet de lentille gravitationnelle faible est la forme d'une galaxie. Pour des galaxies elliptiques, la forme est donnée par le rapport des axes de l'ellipse et l'angle de position de l'axe majeur par rapport à des coordonnées fixes. Les observables des lentilles faibles sont assez subtils et posent de nombreux défis à l'astronomie d'observation. Un défi majeur des lentilles faibles est la correction de la fonction ponctuelle d'étalement (PSF de anglais Point Spread Function) due aux effets instrumentaux et atmosphériques qui provoquent un étalement spatial artificiel des images observées. En autre, cet étalement a tendance à rendre les petits objets plus ronds, détruisant une partie de l'information sur leur véritable ellipticité. En sus, les anisotropies spatiales des PSF ajoute généralement un petit niveau d'ellipticité parasite aux objets, effet non-aléatoire qui peut imiter un signal de lentille. Les effets atmosphériques sont surmontés dans les télescopes spatiaux, mais les défauts instrumentaux persistent. Finalement, les images des galaxies observées sont stockés et ré-échantillonnées sur des pixels de CCD. Une certaine attention doit être apportée à l'ajustement de profils elliptiques sur des images pixelisées (sujettes au sous-échantillonnage).

Une des solutions proposées pour surmonter les défis posés par la PSF est d'opter pour un télescope avec une pupille non-obstruée (optique hors axe). Au cours des dernières années, les designs de télescopes non-obstrués (e.g. Lampton et al., 2010; Levi et al., 2011) ont été proposées pour augmenter la vitesse des sondages du ciel et d'améliorer la précision de mesure des observables des lentilles faibles. Ces premiers

travaux présentent des arguments qualitatifs intéressants, mais n'offre pas d'approche permettant de comparer quantitativement les designs classiques et les design non-obstrués. Notre objectif est donc de quantifier la précision avec laquelle les deux designs de télescopes peuvent mesurer l'angle de position et le raport des axes de galaxies faibles.

Chapter I.2

Concordance Cosmology

The aim of our work is to improve the methods available to investigate the extra-galactic universe using gravitational lensing. We address two challenges faced in lensing studies. For sake of clarity, the thesis is divided into three parts. Part I is on concordance cosmology and objectives of our work, Part II is related to modelling strong gravitational lenses and Part III is related to precision measurement of weak lensing observables.

In Part I we set our work in context of concordance cosmology. First, we discuss some of the major discoveries in cosmology. Next, we recall the important characteristics of gravitational lensing. Then, we discuss the challenges in gravitational lens modelling and measuring lensing observables. Finally, we present our objectives to overcome these challenges.

Expanding Universe

In the early twentieth century Albert Einstein published his theory of general relativity, which provided a unified description of gravity as a geometric property of space and time. Einstein's field equations predicted either the universe should be expanding or contracting. Due to lack of observational evidence Einstein believed that the universe is static. He introduced a *cosmological constant* to counteract the attractive forces of gravity and describe a static universe. When Lemaître (1927)

and Hubble (1929) showed that the radial velocity of galaxies (derived from Doppler shift) is directly proportional to their distance from us, the static universe model was rejected in favour of an expanding universe. The proportionality constant is now known as Hubble's constant and denoted by H_0.

Cosmic Microwave Background

An expanding universe implied that at some point in the past all the matter in the observable universe was contained in an infinitesimal point. The expansion of the universe from a hot dense region was proved by the discovery of the 3.5K uniform background radiation measured by Penzias and Wilson (1964). This cosmic microwave background (CMB) radiation is the relic of the thermal radiation due to the expansion of all the matter in the observable universe from a singular point at the dawn of time. The isotropic nature of the CMB is a robust evidence in favour of the *cosmological principle*, which states that the distribution of matter in the universe is homogeneous and isotropic when viewed on a large enough scale.

Dark Matter

A few decades before the discovery of CMB, Zwicky (1937) estimated that the mass of the clusters of galaxies (especially the coma cluster) is 400 times the luminous (stellar) mass observable. From this result he inferred that there must be some invisible matter holding the cluster together. Also, observations by Rubin and Ford (1970) and Rubin et al. (1980) showed that the mass of galaxies are not centrally concentrated but located at large radii. Even at the edge of the optical observation the mass does not converge to a limiting value. These results led to the fact that invisible matter exists at large radii and beyond the optical edge of galaxies. This invisible mass is now called as *dark matter*, sometimes abbreviated as DM or CDM for cold dark matter.

Table I.2.1: Cosmological Parameters from *Planck* mission

Parameter	Value (68% CL)
Matter density, Ω_M	0.314±0.020
Dark energy density, Ω_Λ	0.686±0.020
Hubbles constant, $H_0\,[km\,s^{-1}Mpc^{-1}]$	67.4±1.4
Age of universe [Gyr]	13.813±0.058

Dark Energy

One of the important discoveries of modern cosmology is the rate of expansion of the universe. Riess et al. (1998) and Perlmutter et al. (1999) used Type Ia supernovae as standard candles to find that the expansion of universe is accelerating. The simplest explanation for an accelerated expansion is the presence of *dark energy*, a mysterious form of energy whose nature is not yet known. This dark energy is often modelled as a cosmological constant (Λ) in Einstein's field equations.

Standard Model of Cosmology

The equations governing the expansion of space for a homogeneous and isotropic universe were derived by Friedmann (1924) and Lemaître (1933). These equations became the *standard model* or concordance cosmology, which assumes a spatially flat expanding universe whose major constituents are cold dark matter (CDM) and dark energy. In the standard model the dark matter and dark energy are denoted by Ω_M and Ω_Λ, which corresponds to their density at this epoch. The standard model is also known as the ΛCDM model of cosmology. We present in table I.2.1 some of the key cosmological parameters obtained from the measurements made by the *Planck* mission (Planck Collaboration, 2014).

N–body Simulations

The equations governing the formation of large scale structures and evolution of galaxies are nonlinear in nature. Advancements in computational science has allowed

cosmologists to solve these equations using N–body simulations, where N stands for the number of fictitious discrete particles (CDM particles). For finite time steps the evolution of each particle is solved for by calculating the gravitational field due to all other particles. The results of these simulations are used to verify whether the theoretical predictions of the ΛCDM cosmology are reproduced by simulations. Springel et al. (2005) performed N-body simulations (N= 2160^3) and predicted the position, velocities and intrinsic properties of galaxies comparable to current surveys. Kim et al. (2009) performed similar simulations (N= 4120^3) to study the three dimensional distribution of luminous red galaxies in our universe.

Gravitational Lensing

In N–body simulations the dark matter is assumed to be a point particle of mass $\sim 10^{11} M_{\odot}$. Real dark matter halos in the same mass range have a finite size and quantifiable mass distribution. In recent years, a new cosmological probe called gravitational lensing has provided an independent means to study the nature of dark matter and dark energy. Gravitational lensing can extract precise measurements of the distribution of mass (stellar + dark matter) in galaxies and galaxy clusters. In this thesis we are interested in improving the tools available to probe extragalactic universe using gravitational lensing. In the next section we give a brief account on gravitational lensing.

I.2.1 Introduction to Gravitational Lensing

Newtonian gravity and Einstein's general relativity predict that the path of light will deflect in the presence of a mass or a gravitational field. Einstein (1936) calculated the correct value of the deflection angle and showed that the light from a background star will be deflected by a foreground star into a luminous ring if the stars and observer are collinear. Einstein noted that this phenomenon may never be observed because the chance alignment is rare. Zwicky (1937) pointed out that the probability of finding foreground galaxies deflecting the light from background galaxies is within

the observational limits of astronomy. This phenomena is now known as *gravitational lensing*.

Zwicky (1937) proposed that gravitational lensing can be used as a tool to find the total mass (stellar + dark matter) of galaxies and clusters. Refsdal (1964) derived the lensing equation and showed that gravitational lensing can be also be used to determine the Hubble's constant from the time delay measurements between several lensed images of the same background source.

Depending upon the position of the observer, lens (foreground mass) and background source, gravitational lensing is split into two categories – strong lensing and weak lensing (cf. Blanford and Narayan, 1992).

Strong Lensing

If the observer, lens and source are collinear gravitational lenses (viz. galaxy or groups of galaxies) image point sources (viz. quasars) into multiple images and extended sources (galaxies) into elongated arcs (or rings). This type of lensing is called *strong lensing*. The first strongly lensed quasar was discovered by Walsh et al. (1979). The quasar QSO 09571+561 is split into two images 5.7 arc secs apart by an intermediate elliptical galaxy. And the first elongated arc was discovered independently by Lynds and Petrosian (1986) and Soucail (1987) in Abell 370 cluster.

Over the years strong lensing has been used to answer questions related to mass structure and substructure in galaxies and cosmography. Using strong lensing the total mass distribution in galaxies is found to be consistent with an isothermal density profile e.g. Treu and Koopmans (2002). Strong lensing has been used to constrain the fraction of dark matter within the effective radius and within the Einstein radius e.g. Treu and Koopmans (2004). Strong lensing is also used to study the substructure in lens galaxies e.g. Dalal and Kochanek (2002), Koopmans et al. (2002). Time delay measurements from the lensed images were used to constrain the Hubble's constant e.g. Coles (2008).

Weak Lensing

If the background sources are not collinear with the observer and lens, they are distorted into small arclets instead of elongated arcs. This phenomenon is called *weak lensing* and was first studied by Tyson et al. (1990) in the Abell 1689 and CL 1490+52 cluster. In the recent years weak lensing has been used to probe the evolution of dark matter and galaxies.

Weak lensing is used to estimate the average mass–to–light ratio in a given field, which in turn is used to estimate Ω_M e.g. Hoekstra et al. (2003). Weak lensing is used to study the evolution of different types of galaxies and the correlation between stellar mass and halo mass as a function of redshift e.g. Mandelbaum et al. (2006). Weak lensing is used to probe the mass density profile of early type galaxies to 100 times the effective radii e.g. Gavazzi et al. (2007). Weak lensing is used to study the evolution of dark matter halos as a function of redshift e.g. Parker et al. (2007).

We discuss in brief the strong and weak lensing phenomena before we set down the aim of our work.

I.2.2 Strong Gravitational Lensing

Among other reviews, Schneider et al. (1992), Kochanek (2004) and Treu (2010) give elaborate accounts of strong lensing from an historical perspective to current advancements in the field. We summarize below the important facts about strong lensing relevant for our thesis. We begin with a basic workings of the optics of strong lensing and then explain the methods used to model strong gravitational lenses.

Observables for Strong Lensing

The optics of strong gravitational lensing is well understood (cf. Schneider et al., 1992). The lensing equation gives the relation between the source position and image position for a given gravitational lens. As dictated by Liouville's theorem gravitational lensing preserves the surface brightness of the source. The observables for strong gravitational lensing are the image positions, relative luminosities and time

delays between multiple images. Time delays are not measured for most of the lenses because photometric follow-ups are observationally expensive and most background sources do not show variation on short time scales (cf. COSMOGRAIL Eigenbrod et al., 2005).

Strong Lens Modelling

In strong lens modelling the forward problem is the task of finding the lensed images for a given gravitational lens and background source. The inverse problem in lens modelling is to find the lens mass distribution, source light profile and source position for given image position and relative luminosities.

The forward problem in strong lens modelling is well posed, meaning a unique solution exists and it can be obtained in a straight forward manner. On the other hand the inverse problem is ill posed and raises three main challenges. Firstly, arbitrarily small errors in the observables will lead to indefinitely large errors in the solution. Secondly, the lensing equation is nonlinear even for simple lens models (e.g. isothermal models), a given source position can have multiple image positions, these cannot be solved for in a straight forward manner. Thirdly, a wide range of lens mass distributions, source light profiles and source positions can give rise to same lensing observables. In order to obtain a solution the inverse problem is usually split into two steps, the source reconstruction and image reconstruction. The reconstructed image is compared with the observed image and Bayesian inference is used to find the lens mass profile and source light profile. In the section below we briefly discuss some of the well-known approaches to solve the inverse problem.

I.2.2.1 Existing Methods for Inverting Strong Gravitational Lenses

There are two families of approaches widely used to solve the inverse problem. They are parametric and non–parametric approach. In parametric approach (e.g. Keeton, 2010) the mass profile of the lens is described by a physical model with a modest number of free parameters. The mass profile is chosen based on observational and

theoretical studies of galaxies. In non–parametric approach (e.g. Saha and Williams, 1997) the lens is modelled as a pixellated mass distribution. The lensing equation is solved for each pixel to obtain the mass distribution. By applying astrophysical constraints (positive mass, smooth gradient, etc.) a finite family of mass profiles are obtained. In this work we favour the parametric approach because parametric models simplify gravitational lens interpretation and allows us to generalize the results to all strong gravitational lenses.

The parametric approach has been used a number of times for solving the inverse problem in lens modelling e.g. Treu and Koopmans (2004), Dye and Warren (2005), Suyu et al. (2006), Jullo et al. (2007) and etc. The lens is usually modelled as isothermal ellipsoids (e.g. Kormann et al., 1994), power law model (e.g. Chae et al., 1998), or NFW (e.g. Keeton, 2010). Observational studies motivate an isothermal or power law model for galaxy-scale dark matter halos and NFW profile for cluster-scale dark matter halos. Once the lens model is chosen, the next step in solving the inverse problem is source reconstruction. Usually in parametric approach the source is reconstructed using grid-based models or as smeared collection of point sources. Suyu et al. (2006) use regular grids and Dye and Warren (2005) use irregular (or adaptive) grids in the source plane to reconstruct the source. Jullo et al. (2007) reconstruct the source as a smeared collection of point sources. In the above mentioned source reconstruction techniques, the reconstructed sources cannot be compared with real sources because they do not have a physical model.

Methods developed earlier did not physically model the source for the following reason. In observed gravitational arcs due to the presence of noise and intrinsic faintness of the background sources, the extracted portion of the gravitational arc does not constitute the whole source. When source reconstruction methods are applied to this extracted arc, only a part of the source is reconstructed in the source plane. This reconstructed source is just a random distribution of pixels or point sources in the source plane and sufficient data was not available to infer the physical model of the whole source from just the reconstructed portion. In recent years HST follow-up images of known lenses have produced arcs with higher resolution and better S/N. For these images the source can be modelled in conjunction with the

lens. Brewer et al. (2012) report an inversion method in which they reconstruct the source with a Sérsic light profile. They tailored their method to study one particular observed lens CSWA 31. In this thesis, we develop our own method to model the lens and source in conjunction, which we apply to a larger set of observed gravitational arcs to obtain a better understanding of the mass profile of galaxies. A similar approach for reconstructing the sources was also adopted by Kostrzewa-Rutkowska et al. (2014).

I.2.3 Weak Gravitational Lensing

Bartelmann and Schneider (1996) give an elaborate review on theory and applications of weak gravitational lensing. We present below some facts from their review, which we find relevant to the scope of our work. We explain weak gravitational lensing, its cosmological applications, the observables and the challenges faced by current missions probing cosmology using weak lensing.

If a faint and distant galaxy population is observed through a gravitational lens, the appearance of background galaxies are distorted by the gravitational field of the lens and the magnification associated with gravitational lensing changes the apparent brightness of the background sources. If the intrinsic shape of a background galaxy is known, it can be used to compute the local gravitational field responsible for the distortion and magnification of the galaxy. Unfortunately the intrinsic shape of the background galaxy is an unknown, so the local gravitational field can only be studied by performing statistical measurements on an ensemble of galaxies in a chosen field, assuming that the average properties of the ensemble is known.

Observables for Weak Lensing

One of the important observable for weak gravitational lensing is the shape of a galaxy. For galaxies with elliptical isophotes, the shape is given by the axis ratio of the ellipse and the position angle of the major axis with respect to some fixed coordinates. The shape of a galaxy is often denoted by the term *ellipticity*. A naive

definition of ellipticity is the axis ratio subtracted from one. Hence, the ellipticity of a spherical galaxy is zero. Since it is not possible to fit elliptical isophotes for irregular galaxies Bartelmann and Schneider (1996) define a complex ellipticity using the second moments of the galaxy image. In this work we use only the axis ratio and position angle of a galaxy to define its shape.

I.2.3.1 Challenges Faced in Measuring the Weak Lensing Observables

Weak lensing observables are quite subtle and pose numerous challenges in the field of observational astronomy. Major challenge for weak lensing is correction for the point spread function (PSF) due to instrumental and atmospheric effects, which causes the observed images to be smeared. This smearing tends to make small objects more round, destroying some of the information about their true ellipticity. As a further complication, the PSF typically adds a small level of spurious ellipticity to objects in the image, which is not random, and can mimic a true lensing signal. Atmospheric effects are overcome in space-based telescopes but instrumental errors persist. Also, observed galaxy images are given in terms of pixel brightness in CCDs so care must be taken when fitting isophotal ellipticals to pixellated images.

One of the solutions proposed to overcome the challenges posed by the PSF is to opt for a telescope with an unobstructed pupil. In recent years telescopes with unobstructed pupils (e.g. Lampton et al., 2010; Levi et al., 2011) have been proposed to increase the speed of survey and improve the precision in weak lensing observables. But sufficient work has not been done to quantify the gain in moving from telescopes with obstructed pupil to telescopes with unobstructed pupil. Our objective is to quantify the precision with which both the telescopes can measure the axis ratio and position angle of galaxies.

I.2.4 Outline of this Thesis

In Part II we present a new method to invert strong gravitational lenses and model both the gravitational lens and the background source in conjunction. In chapter II.1 we present our procedure to solve the forward problem in lens modelling i.e. to find the lensed images for a given lens and background source. In chapter II.2 we present our procedure to solve the inverse problem i.e. to find the lens and source parameters for given gravitational arcs using statistical inference. In chapter II.3 we test our inverse method on simulated gravitational arcs to verify how rigorously our method can recover the simulated lens and source parameters. In chapter II.4 we apply our lens inversion method on observed gravitational arcs and compute the lens and source parameters. In chapter II.5 we use the computed lens and source parameters to probe the extragalactic universe namely the galaxy-scale halos and high redshift sources.

In part III we develop a method and use it to test whether telescopes with unobstructed pupils can measure weak lensing observables with greater precision when compared against telescopes with obstructed pupils. In chapter III.1 we present the theoretical arguments in favour of an unobstructed pupil for weak lensing surveys. In chapter III.2 we design and optimise three mirror anastigmat telescopes with obstructed and unobstructed pupil. In chapter III.3 we use the PSFs of the optimised telescopes to simulate quasi–realistic galaxy images and also describe various methods to measure the axis ratio and position angle of the simulated galaxy images. In chapter III.4 we measure the axis ratio and position angle of the simulated galaxies for various scenarios. In chapter III.5 we discuss the precision with which unobstructed pupils measure weak lensing observables when compared against obstructed pupils.

Part II

Inverting Strong Gravitational Lenses

Chapter II.1

The Forward Problem in Lens Modelling

In section I.2.1 we gave an introduction to strong gravitational lensing and stated that our goal is to improve the method used to solve the inverse problem in gravitational lens modelling. Before we present our method to solve the inverse problem, we recall some basic concepts related to strong gravitational lensing in this chapter. Using these concepts we develop a method to solve the forward problem in gravitational lensing. It is imperative to understand the method for solving the forward problem because the procedure to solve the inverse problem heavily uses the ideas and concepts used in solving the forward problem.

We begin with the brief description of the lensing equation. Next, we show how to solve the lensing equation for a singular isothermal sphere. Then, we present the model we use for our lens mass profile and source light profile. Finally, we present the procedure to solve the forward problem in lens modelling and simulate gravitational arcs for some arbitrary lens and source parameters. We use the simulated arc to test the rigorousness with which our method can solve the inverse problem in lens modelling.

Table II.1.1: Values for the constants

Constant	Symbol	Value
Newton's gravitational constant	G	4.302×10^{-3} pc $M_{\odot}^{-1}km^2s^{-2}$
Speed of light	c	3×10^5 km s^{-1}
Hubble's constant	H_0	70 km $s^{-1}Mpc^{-1}$
Matter density	Ω_M	0.3
Dark energy density	Ω_Λ	0.7

II.1.1 Lensing Equation

In this section we briefly discuss the lensing equation. A more detailed account can be found in Schneider et al. (1992). The schematics of the gravitational lens system is shown in figure II.1.1. The quantities $\vec{\theta_I}$ and $\vec{\theta_S}$ denote the image position and source position, D_d, D_s and D_{ds} denote the observer–deflector, observer–source and deflector–source angular diameter distances. The deflection angle α is given as a function of ξ the impact distance of a light ray and $M(\xi)$ the lens mass profile (cf. Refsdal, 1964).

$$\hat{\alpha}(\xi) = \frac{4G}{c^2}\frac{M(\xi)}{\xi} \tag{II.1.1}$$

The expressions for the angular diameter distances D_d (same for D_s) and D_{ds} are given below (cf. Peebles, 1993).

$$D_d = \frac{1}{1+z_d}\frac{c}{H_0}\left[\int_0^{z_d}\frac{dz'}{E(z')}\right] \tag{II.1.2}$$

$$D_{ds} = \frac{1}{1+z_s}\frac{c}{H_0}\left[\int_0^{z_s}\frac{dz'}{E(z')} - \int_0^{z_d}\frac{dz'}{E(z')}\right] \tag{II.1.3}$$

Where z_d, z_s are the redshifts of the deflector and source, and $E(z) = \sqrt{\Omega_M(1+z)^3+\Omega_\Lambda}$. The values for the constants are given in table II.1.1.

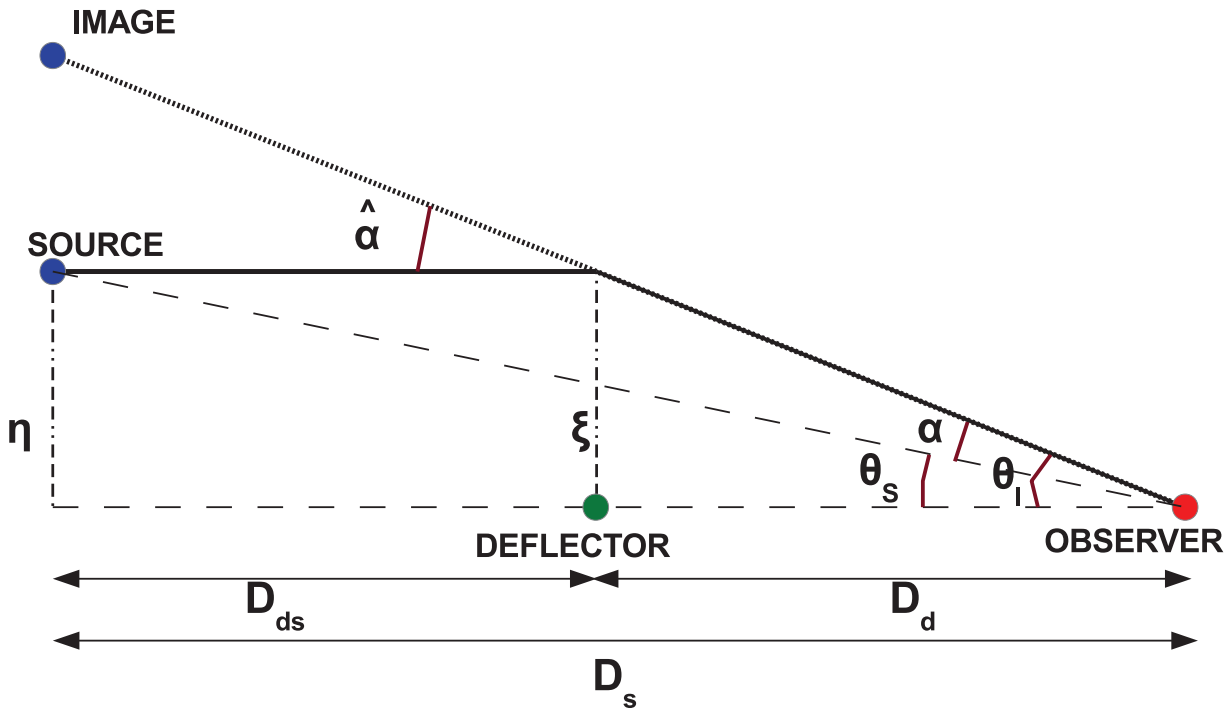

Figure II.1.1: **Illustration of a gravitational lens system:** This figure shows the observer, the gravitational lens (or deflector), the background source and image positions for a typical gravitational lens system. The quantities D_d, D_s and D_{ds} are the observer–deflector, observer–source and deflector–source angular diameter distances respectively. The quantity θ_S is the angular position of the source, θ_I is the angular position of the image and $\hat{\alpha}$ is the deflection angle. η denotes the source position and ξ denotes the photon impact distance from the center of deflector. NOTE: All angles are exaggerated in the figure.

II.1.1.1 Assumptions for a Thin Lens

Before we proceed to write the lensing equation, we list the standard assumptions for modelling the lens (cf. Gorenstein et al., 1988). The assumptions are as follows.

1. *Geometrical Optics* – The deflector is transparent, and the wavelength of the deflected radiation is small compared with all other relevant length scales (D_d, D_s and D_{ds}).

2. *Sudden Approximation* – Light deflection is assumed to occur wholly in the deflector plane.

3. *Small–angle approximation* – All deflection angles are small i.e. they are in the order of arc-seconds.

4. *Static, smooth lens system* – The positions of the source, deflector, and observer are stationary with respect to comoving coordinates, and the distribution of the deflection mass in its plane is time–independent and has smooth spatial variation.

5. *Center of mass* – We assume the center of brightness of the deflector to be coincident with its center of mass. This assumption can be relaxed at the cost of increasing the number of unknowns in the lensing equation.

6. *Metric* – Other than in the deflector, matter is everywhere isotropically and homogeneously distributed, consistent with Robertson Walker (RW) metric.

II.1.1.2 Lensing Equation in Dimensionless form

The lensing equation gives the relation between the source position and image position for a given gravitational lens. In this section we give a brief account on how to obtain the lensing equation in dimensionless form and then rewrite it using complex representation. Since the positions in the image plane are measured in arcsecs it is convenient to work using the dimensionless form of the lensing equation. We find the complex representation of the lensing equation useful because we can use the tools to

study functions of complex variables to analyse the lensing equation. For a detailed derivation of the lensing equation we refer the reader to Schneider et al. (1992).

If the angles $\vec{\theta_S}, \vec{\theta_I}$ and $\hat{\vec{\alpha}}$ (cf. figure II.1.1) are small, the lensing equation is written as follows (cf. Refsdal, 1964).

$$\vec{\theta_S} D_s = \vec{\theta_I} D_s - \hat{\vec{\alpha}} D_{ds} \tag{II.1.4}$$

In units of parsecs the source position and image positions are given by $\vec{\eta} = \vec{\theta_S} D_s$ and $\vec{\xi} = \vec{\theta_I} D_d$. Substituting these in equation II.1.4 one can get the following equation.

$$\vec{\eta} = \frac{D_s}{D_d}\vec{\xi} - \hat{\vec{\alpha}} D_{ds} \tag{II.1.5}$$

By introducing a length scale $\xi_0 = \frac{2\pi}{1296000} D_d$ and defining $\vec{x} = \frac{\xi}{\xi_0}$, $\vec{y} = \frac{\eta}{\eta_0}$, where $\eta_0 = \frac{D_s}{D_d}\xi_0$, one can obtain the dimensionless form of the lensing equation, which is given below.

$$\vec{y} = \vec{x} - \vec{\alpha}(\vec{x}) \tag{II.1.6}$$

$$\vec{a}(\vec{x}) = \frac{D_{ds} D_d}{\xi_0 D_s}\hat{\vec{\alpha}}(\vec{\xi}) \tag{II.1.7}$$

Complex representation of the lensing equation

Bourassa and Kantowski (1975) provided a complex representation of equation II.1.6 which is

$$\mathrm{y} = \mathrm{x} - \mathrm{a(x)} \tag{II.1.8}$$

where $\mathrm{y}(= \mathrm{y_1} + \mathrm{iy_2})$ is the source-plane coordinates and $\mathrm{x}(= \mathrm{x_1} + \mathrm{ix_2})$ is the image plane coordinates. The deflection angle $\mathrm{a(x)} = \mathrm{a_1} + \mathrm{ia_2}$ a function of the lens parameters depends on the lens model. We define a(x) in section II.1.4, after introducing

the parametric model for the lens.

II.1.1.3 Lensing Equation for Special Cases

The lensing equation given above needs to be modified for some special instances. The lens galaxies are not isolated from the rest of the universe. There may be galaxies or clusters near the lensing galaxy or along the line of sight. The presence of other massive objects will affect the lensing equation as follows.

Presence of external shear

Massive objects in the neighbourhood of the primary lens galaxy act as a source of external shear. In the presence of external shear ($\gamma = \gamma_1 + i\gamma_2$) the lensing equation II.1.8 becomes (Keeton et al., 1997)

$$\mathrm{y} = \mathrm{x} - \mathrm{a}(\mathrm{x}) + \gamma \mathrm{x}^* \tag{II.1.9}$$

where $\mathrm{x}^* (= \mathrm{x}_1 - \mathrm{ix}_2)$ is the complex conjugate of x.

n lenses in the lens plane

If there is more than one lens in the lens plane significantly affecting the deflection angle and flux amplification, the lensing equation is written as the summation of all the deflection angles.

$$\mathrm{y} = \mathrm{x} - \sum_{n=1}^{N} \mathrm{a_n}(\mathrm{x} - \mathrm{x_{lens}}) \tag{II.1.10}$$

where $\mathrm{x_{lens}}$ is the complex representation of the position of the lens in the lens plane.

Two lenses at different redshifts

If there are two lenses at different redshifts along the line of sight between the observer and the source, the transformation map between the image plane and the source plane is given below (cf. Gavazzi et al., 2008).

$$y_1 = x - a_1(x - x_{\text{lens}\,1}) + \gamma x^* \tag{II.1.11}$$

$$y_2 = y_1 - a_2(y_1 - x_{\text{lens}\,2}) \tag{II.1.12}$$

The lens labeled '1' is nearest to the observer and the lens labeled '2' is the farthest. The shear term is included only for the lens nearest to the observer.

We use the lensing equation to find the transformation map and flux amplification map. We explain these maps and how we obtain them in the next section.

II.1.2 Procedure to Compute the Transformation Map

The transformation map is a mapping between the image plane and the source plane. It shows where each pixel in the image plane is mapped on to the source plane. The transformation map can be obtained by solving the lensing equation II.1.8 for each pixel in the lens plane. We obtain the transformation map using the method presented in Newbury and Spiteri (2002). They construct a square grid on the image plane with N^2 number of pixels and pixel size Δ and solve the lensing equation to find the mapping between the image plane and source plane. In figure II.1.2 we show the transformation map for a singular isothermal sphere (SIS). We can see that the square pixels in the image plane are transformed into quadrilaterals in the source plane. For a SIS lens the lensing equation II.1.8 becomes (cf. Kormann et al., 1994)

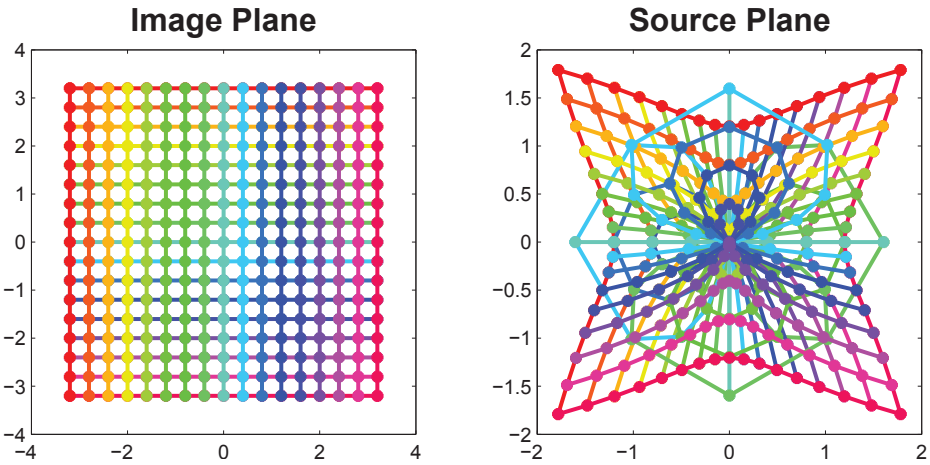

Figure II.1.2: **Mapping between image plane and source plane:** This figure shows the transformation map between the image plane and source plane for a SIS lens. The Einstein radius of the lens is set to be $2''$ and pixel size is chosen as $0.4''$. Square pixels in the image plane are mapped into quadrilaterals in the source plane.

$$\mathrm{y} = \mathrm{x} - R_{Ein}\frac{\mathrm{x}}{|\mathrm{x}|} \tag{II.1.13}$$

where Einstein radius (R_{Ein}) is the angular radius of the ring shaped structure formed when the observer, lens and source are in exact alignment. In the next section we use the transformation map to compute the flux amplification map.

II.1.3 Procedure to Compute the Flux Amplification Map

We recall that gravitational lensing conserves surface brightness as dictated by Liouville's theorem. Therefore, the flux received from the background source is amplified in the presence of a massive foreground object. The flux amplification map shows

the amplitude by which the flux in the source plane is amplified in the image plane. Generally the amplification is calculated from the inverse magnification tensor, whose components are second order derivatives of the lens potential (cf. Schneider et al., 1992). The flux amplification μ(x) is written as a function of convergence (κ) and shear (γ) as follows

$$\mu(\mathrm{x}) = \frac{1}{|(1-\kappa)^2 - \gamma^2|} \tag{II.1.14}$$

Critical Curves and Caustics

The amplification factor will tend to infinity when the denominator in the above equation tends to zero. The locus of points in the image plane where $\mu(x)$ is infinite is called the *critical curve*. When this curve is mapped to the source plane it is called a *caustic*. The critical curve for a SIS lens is a circle whose radius is the Einstein radius (R_{Ein}) and the caustic is a singular point at the center of the source plane. Real gravitational lenses do not produce infinite magnification due to diffraction.

An alternate method to find the amplification factor

In equation II.1.4 the convergence (κ) and shear (γ) are not simple analytical expressions for sophisticated lens models. Therefore we use an alternate method to find the amplification factor. Since gravitational lensing conserves surface brightness as dictated by Liouville's theorem, we approximate the amplification factor μ(x) as the ratio between the area of the pixel in the image plane and the area enclosed by the same pixel when mapped to the source plane. We recall from figure II.1.2 that the square pixels in the image plane are transformed into quadrilaterals in the source plane. The amplification μ(x) is therefore the ratio between the area of the square in the image plane and the corresponding quadrilateral in the source plane.

The flux amplification factor near the caustics

The quadrilaterals in the source plane are not always well defined. Figure II.1.3 shows an example of how the pixels close to the critical region are transformed for an SIS lens with Einstein radius 3″. In the left panel of figure II.1.3 both the image and source plane are shown to same scale. In the right panel the source plane is scaled to show the ill-defined quadrilaterals.

Due to badly mapped quadrilaterals we underestimate or overestimate the amplification factor near the critical regions on the image plane while equation II.1.14 leads to an infinite magnification in these regions. We know that this problem occurs only near the critical regions in the image plane. So we resample all pixels that have an amplification factor above a given threshold into finer pixels and recalculate the amplification factor for these again. This method allows us to reduce the error in the amplification factor near the critical regions. Using this method we also avoid infinite amplification that would occur otherwise.

In the next section we present the lens model we chose for our study. We will use the above methods to compute the transformation map and flux amplification map for the lens model chosen.

II.1.4 Parametric Model for the Lens Mass Profile

The parametric model chosen to represent the lens should be in agreement with the mass profile of observed galaxies in general. A number of evidences e.g. spiral galaxy rotation curves (cf. Rubin et al., 1980), stellar dynamics of elliptical galaxies (cf. Rix et al., 1997) and X-ray halos of elliptical galaxies (cf. Fabbianno, 1989) suggest an isothermal mass profile for the lens.

In this work we model our lens as a nonsingular isothermal ellipsoid (NIE). The NIE model is an extension of the isothermal sphere and can have a flat or cuspy core. Our assumption is that the combination of stellar and dark matter in galaxy lenses follow such a profile. Results obtained by Treu and Koopmans (2004), Gavazzi et al. (2007) and others support this assumption. To account for the gravitational

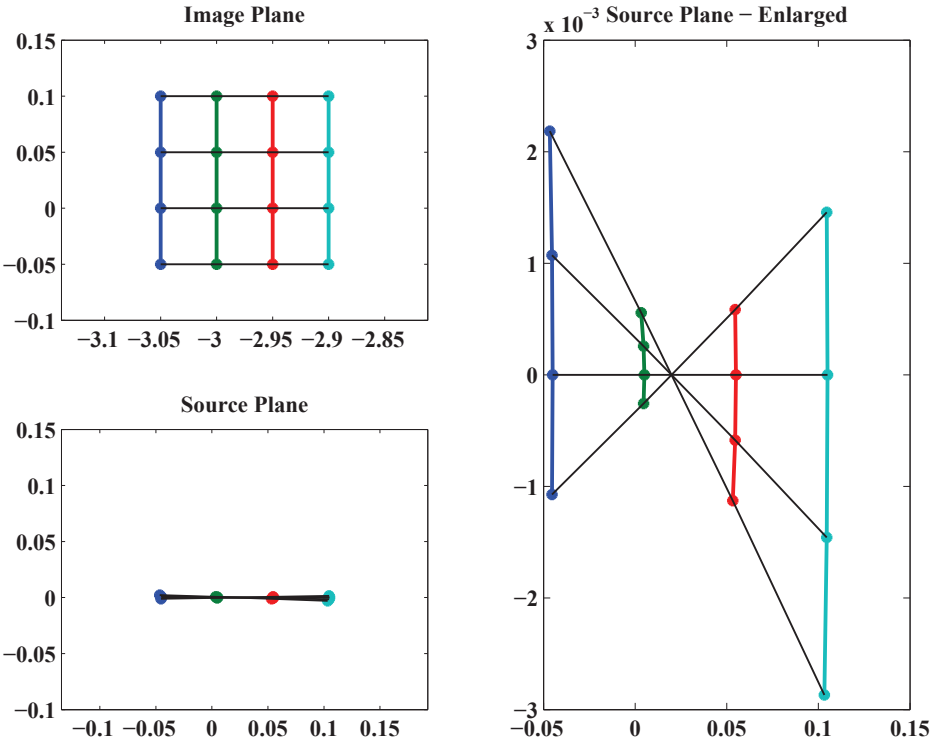

Figure II.1.3: **Flux amplification near the caustics:** This figure shows the transformation map for 9 pixels in the image plane lying close to the critical curve. The pixel size is $0.05''$ and the lens is a singular isothermal sphere with Einstein radius $3''$. In the left panels of the figure both the image and source plane are shown in same scale. In the right panel the vertical axis of the source plane is scaled to show the ill-defined quadrilaterals.

Table II.1.2: Description of the Lens Parameters

Parameter	Definition	Limits
R_{Ein}	The Einstein radius	
σ_v	Dispersion velocity along line of sight	
f	Axis ratio of the lens	$0 < f \leq 1$
b_c	Core radius of the lens	$0 < b_c \leq 0.5$
θ	Position angle of the lens	$-\pi/2 < \theta \leq \pi/2$
γ	Complex external shear, $\gamma = \gamma_1 + i\gamma_2$	
f'	$\sqrt{1-f^2}$	
b^2	$x_1^2 + f^2 x_2^2$	
$(b^2)_{,x^*} \equiv \frac{\partial b^2}{\partial x^*}$	$x_1 + \mathrm{i} f^2 x_2$	

$\mathrm{x} = \mathrm{x}_1 + \mathrm{i}\mathrm{x}_2$ is the center of a pixel in the image plane

effects of massive neighbours, we add an external shear to the NIE model. The NIE model and its limiting cases were studied in detail by Kormann et al. (1994). The parameters that define the NIE model are given in table II.1.2.

Characteristics of a NIE lens

Consider a NIE lens whose projected axis ratio is f ($f = 1$ for circle), core radius is b_c and dispersion velocity along the line of sight is σ_v. Kormann et al. (1994) give the projected surface mass density $\Sigma(x)$ of this lens as

$$\Sigma(x) = \frac{\sigma_v^2}{2G} \frac{\sqrt{f}}{\xi_0 \sqrt{x_1^2 + f^2 x_2^2 + b_c^2}} \tag{II.1.15}$$

For the surface mass density given by equation II.1.15, Kormann et al. (1994) compute the complex conjugate of the deflection angle $\mathrm{a}^*(\mathrm{x})$ as

$$\mathrm{a}^*(\mathrm{x}) = R_{Ein}\frac{\sqrt{f}}{f'}\left[\operatorname{arctanh}\frac{f'\sqrt{b^2+b_c^2}}{(b^2)_{,x^*}} - \operatorname{arctanh}\frac{f'b_c}{f\mathrm{x}}\right] \tag{II.1.16}$$

$$R_{Ein} = 4\pi\frac{\sigma_v^2}{c^2}\frac{D_{ds}}{D_s}\frac{360*60*60}{2\pi}[arcsec] \tag{II.1.17}$$

Einstein radius (R_{Ein}) is the angular radius of the ring shaped structure formed when the observer, lens and source are in exact alignment. The angular diameter distances D_{ds} and D_s are given by equations II.1.2 and II.1.3. By taking appropriate limits for the equation II.1.16 (cf. Kormann et al., 1994), the deflection angle can be calculated for a singular isothermal sphere (SIS: $f \to 1$, $b_c \to 0$), non-singular isothermal sphere (NIS: $f \to 1$) and singular isothermal ellipsoid (SIE: $b_c \to 0$).

The complex representation of the lensing equation for a NIE lens in the presence of external shear ($\gamma = \gamma_1 + i\gamma_2$) is given by the equation below.

$$\mathrm{y} = \mathrm{x} - \mathrm{a}(\mathrm{x})e^{i\theta} + \gamma\mathrm{x}^* \tag{II.1.18}$$

Keeton (2001) proposes a list of parametric models for modelling the lens mass profile. Other lens mass profiles mentioned in Keeton (2001) can be studied by inserting the appropriate deflection angle, a(x) into the above equation. But the deflection angle is not a simple analytical expression for all the lens models.

II.1.5 Parametric Model for the Source

The parametric models chosen for the source light profile should be in agreement with the observed sources at similar redshifts. The projected surface brightness of most galaxies are fitted well using the Sérsic profile (cf. Ciotti, 1991; Trujillo et al., 2004). Therefore, we assume a reasonable fraction of the gravitational arcs in strong lensing cases should follow a Sérsic light profile in their unlensed state. The Sérsic profile describing the intensity of a galaxy at some radius R from the center is given below (Sérsic, 1963).

Table II.1.3: Description of the Source Parameters

Parameter	Definition	Limits
I_e	The intensity at R_e	
R_e	Effective radius enclosing half total light	
n	shape parameter	$0.5 < n < 8$
b_n	1.992n – 0.327	
$y_{src} = y_{1src} + iy_{2src}$	Position of the source in the source plane	

$n = 4$ for de Vacouleur profile
$n = 1$ for exponential profile

$$I(R) = I_e \exp\left(-b_n \left[\left(\frac{R}{R_e}\right)^{1/n} - 1\right]\right) \tag{II.1.19}$$

The parameters of the Sérsic profile are explained in table II.1.3. Sérsic profile is a generalization of the other profiles viz. de Vacouleur and exponential profile.

II.1.6 Procedure to Solve the Forward Problem

In this section we illustrate the forward problem in lens modelling. We show how to find the lensed images of a background source for a given lens mass profile and source light profile. For the given lens parameters, we solve the lensing equation and obtain the transformation map as described in section II.1.2. Then, we set the source's position and light profile in the source plane. The source is described by a ellipse with some cut-off radius beyond which the flux is below the observational limit.

We use the transformation map and ray trace every pixel from the image plane to the source plane. If the pixel in the image plane is mapped to a region inside the cut-off radius, we back trace the surface brightness of the source from that point to the image plane. We thus obtain all the lensed images of the source in the image

Table II.1.4: Lens and Source Parameters for a Simulated Gravitational Arc

Lens		Source	
Parameter	Value	Parameter	Value
R_{Ein}	$1.6''$	I_e	1
f	0.8	R_e	$0.2''$
b_c	$0.2''$	n	4
θ	0.698	e_{src}	0.3
γ	$0.05 - 0.00i$	θ_{src}	0
		$y_{1src} + iy_{2src}$	$-0.14 + 0.14i$

e_{src} and θ_{src} are ellipticity and position angle of the source
cf. section 2.1 and 2.2 for the definition of other parameters

plane.

II.1.6.1 Example of a Simulated Gravitational Arc

Figure II.2.1 shows the simulated gravitational arc for a set of arbitrary lens and source parameters presented in table II.1.4. We added two different levels of noise to the simulated arc to study the influence of noise in our reconstruction technique. After the addition of noise the S/N of the extracted portion of the arc is ∼10 and ∼3 respectively. In these arcs we only use the pixels with S/N above 5 for lens inversion. The S/N of individual pixels in the arc can be greater than that of the whole arc. The image with S/N=10 has 336 pixels available for inversion and the image with S/N=3 has only 68 pixels available for inversion.

II.1.7 Summary

In this chapter we presented the lensing equation, the procedure to compute the transformation map and the procedure to compute the flux amplification map. We justified our choice of the lens mass profile and source light profile. Finally, we used the methods developed to simulate gravitational arcs for an arbitrary set of lens

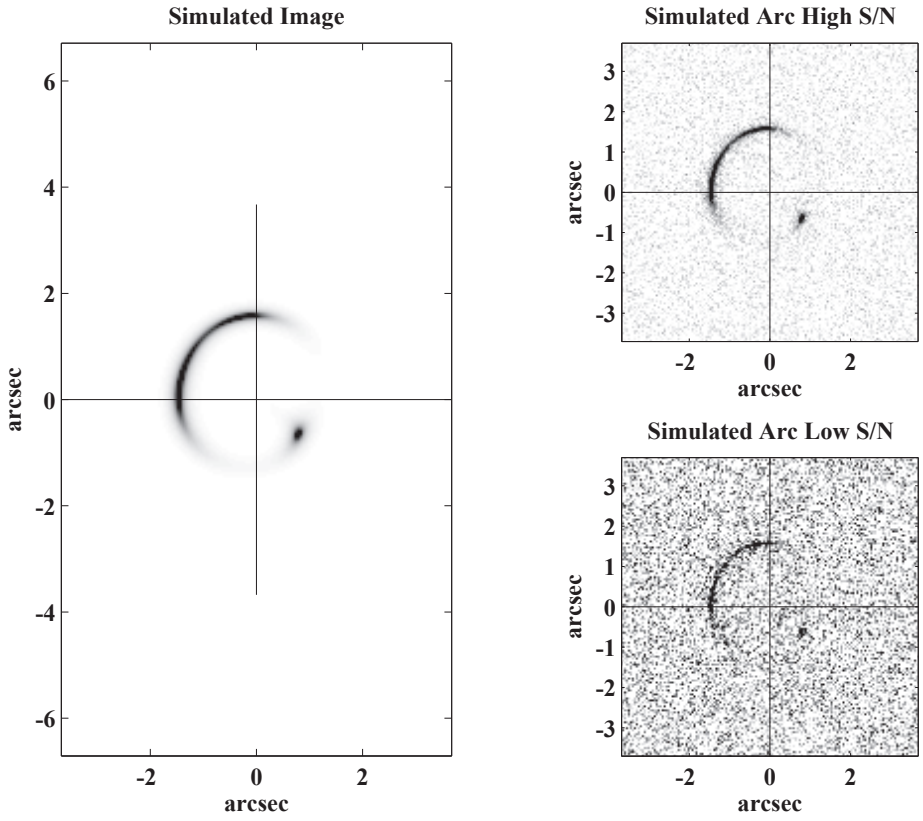

Figure II.1.4: **Example of a simulated gravitational arc:** The image on the left panel is the gravitational arc simulated using the lens and source parameters in table II.1.4. The panels on the right show the same arc with two different levels of noise.

and source parameters. In the next chapter we present our method to solve the inverse problem in lens modelling. We use the simulated arc to test our inversion method and quantify the precision with which we can recover the lens and source parameters for an observed gravitational arc. The actual MATLAB[1] and PYTHON[2] routines we wrote to compute the transformation map, flux amplification map and simulate gravitational arcs can be found at GITHUB. In the APPENDIX we present brief guidelines for using the routines.

[1]https://github.com/balaonspace/invertStrongLens–Matlab
[2]https://github.com/balaonspace/invertStrongLens–Python

Chapter II.2

The Inverse Problem in Lens Modelling

In this chapter we present the method we developed to solve the inverse problem in lens modelling. We recall that in gravitational lens modelling the inverse problem is the task of finding the lens mass profile, the source light profile and source position for an observed gravitational arc. The outline of the chapter is as follows. In section II.2.1 we give a brief account on the challenges faced while solving ill-posed problems. In section II.2.2 we use statistical inference to solve the inverse problem.

II.2.1 Brief Account on Ill-Posed Problems

An ill-posed problem is one for which there is no unique solution and small uncertainties in the observables will lead to wildly different solutions. In this section we describe why the inverse problem in lens modelling is ill-posed and how ill-posed problems are handled. First, we recall the lensing equation II.1.8 which is

$$\mathrm{y} = \mathrm{x} - \mathrm{a}(\mathrm{x})e^{i\theta} + \gamma \mathrm{x}^*$$

where a(x) = $f(R_{Ein}, f, b_c, \mathrm{x})$, is nonlinear in all variables. This equation is nonlinear in x and all the lens parameters, therefore there is no unique solution to the lens parameters.

The logical approach to solve the inverse problem is to reconstruct the source for random lens parameters, compute the gravitational arcs for the reconstructed source, find the chi-squared between observed arc and computed arc, and finally the best fit solution is the set of parameters with the smallest chi-squared value. The major issues with this approach are, the phase space of the lens parameters is vast and all possible combinations cannot be explored. Second, due to errors in the observables, a reasonable fraction of the lens parameters can give rise to comparable values of chi-squared and the best solution might be far from the real solution. Finally, no constraint has been placed on the reconstructed source and this source could be a physically meaningless one.

Since it is not possible to explore the full phase space of possible lens parameters, we need to infer the solution from a finite sample in the phase space. In this finite sample, the solution with the lowest chi-squared might not be the best solution because the right combination of lens parameters may not be present in this finite sample. Therefore, we introduce statistical inference which will give us a probability distribution for all the lens and source parameters. We explain statistical inference in the next section.

II.2.2 Procedure to Solve the Inverse Problem Using Statistical Inference

Statistical inference is commonly used to find the posterior distribution of the solution based on prior probability, likelihood and evidence. We use the Bayes' rule to obtain the posterior probability for an hypothesis (H) and given evidence (E).

$$\overbrace{P(H|E)}^{Posterior} = \frac{\overbrace{P(H)}^{Prior}\overbrace{P(E|H)}^{Likelihood}}{\underbrace{P(E)}_{Evidence}} \tag{II.2.1}$$

In our study, the hypothesis (H) is the lens model and lens parameters and P(H) is the prior probability for the lens parameters. The evidence E is the observed image and P(E) is same for all cases. Since we always choose a uniform prior for the lens parameters and the probability of evidence is same for all the cases, the posterior probability is just proportional to the likelihood.

$$\overbrace{P(H|E)}^{Posterior} \propto \overbrace{P(E|H)}^{Likelihood} \tag{II.2.2}$$

We obtain the posterior distribution for the lens and source parameters by following the steps below.

Step 1 – Select a lens model and choose a prior for the lens parameters.

Step 2 – Reconstruct the source for a set of lens parameters randomly chosen from the prior distribution.

Step 3 – Solve the forward problem and reconstruct the lensed images for the chosen lens and reconstructed source.

Step 4 – Define likelihood as a function of the summed squared residuals (SSE) for the source and the reduced chi-squared (χ^2_{image}) between the observed and reconstructed image.

Step 5 – Compute the posterior probability distribution for the lens and source parameters by creating a Markov Chain using the Metropolis–Hastings algorithm (cf. Metropolis et al., 1953; Hastings, 1969).

We describe each step in detail below.

II.2.2.1 Step 1 – Prior Distribution for Lens parameters

We recall from II.2.1 that it is not possible to explore the whole phase space of the lens parameters. A finite sample is randomly chosen from the phase space as follows. We bound the lens parameter in some interval $[a, b]$ and assign equal probabilities to all possible values in that interval. We assign a uniform prior for all the lens parameters in the chosen interval because the uniform distribution has the highest entropy. In the absence of any evidence to assign higher probabilities to some values the uniform prior is a conservative choice. For example the core radius b_c is bounded in the interval $0 < b_c < 0.5$, which includes all the realistic values of the core radius. The uniform prior assigns equal probability for all values of the core radius in the interval $[0, 0.5]$. We randomly sample a finite number of values in that interval for the core-radius. Similar bounds are chosen for all the lens parameters. We will discuss the prior distribution in detail when testing our method on simulated arcs in section II.3.2.

II.2.2.2 Step 2 – Source Reconstruction

In this section we show how we reconstruct the source for an observed gravitational arc and given lens parameters. Then, we demonstrate the method on the gravitational arc simulated in section II.1.6.

Procedure to reconstruct the source

The first task in source reconstruction is to extract the arc from the observed image. Then, for some randomly sampled lens parameters, we compute the transformation map and flux amplification map as detailed in sections II.1.2 and II.1.3. We divide the extracted pixels of the arc by the flux amplification factor, and obtain their appropriate intensity in the source plane. Next, we use the transformation map to ray trace the pixels of the arc from the image plane to the source plane. After this the source is reconstructed using grid based models or as smeared collection of point sources. We recall that Suyu et al. (2006) use regular grids and Dye and Warren

(2005) use irregular (or adaptive) grids in the source plane to reconstruct the source. Jullo et al. (2007) reconstruct the source as a smeared collection of point sources. On the other hand we physically model the source using a Sérsic light profile.

In the source plane, we choose the point with maximum intensity as the centre of our source. It is reasonable to assume that the centre, an intrinsically bright region of the source is always observed in the image plane. We compute the distance between the assumed centre and the other ray-traced pixels in the source plane. Then, we plot the intensity of the ray-traced pixels as a function of their distance from the centre, and fit a Sérsic profile for this plot.

Due to the presence of noise and the intrinsic faintness of the background source, it will not be possible to extract the whole arc from the observed image. Therefore, when source reconstruction methods are applied to this extracted arc, only a part of the source is reconstructed in the source plane. In order to limit the impact of noise from dominating Sérsic fit, we only use the extracted pixels of the arc whose S/N are above five. If the threshold is relaxed to a lesser value (say pixels with S/N above 3), the inclusion of several noisy pixels, results in a reconstruction with poor goodness of fit. Also, to take into account the uncertainty in the flux of the arc due to the contamination by the flux of the lensing galaxy, we prefer to use only pixels whose S/N are above five.

Example for Source Reconstruction

In figure II.2.1 we show the reconstructed source for the gravitational arc simulated in section II.1.6. The sources were reconstructed using the simulated lens parameters given in table II.1.4. In figure II.2.1 the left panels show the simulated arcs with different noise levels, the centre panels show the reconstructed sources in the source plane and right panels show the Sérsic fit for the source. In the source plane image (centre panels figure II.2.1), we can see that only the intrinsically bright center and regions near the caustic are reconstructed for the source. A one dimensional Sérsic profile is fitted to the reconstructed source as described above. Even though the simulated source is ellipse there is not sufficient information in the reconstructed

Table II.2.1: Sérsic fit for source parameters

Parameter	Simulated Value	Fitted Value	
		S/N=10	S/N=3
Intensity at R_e, I_e	6	11.9	30.3
Effective radius,R_e	$0.2''$	$0.115''$	$0.043''$
Sérsic index, n	4	3.22	2.62
Position of source, $y_{1src} + iy_{2src}$	$-0.14 + 0.14i$	-0.15+0.13i	-0.16 +0.14i
SSE		0.053	0.042

source to fit a 2-D profile. We approximate the shape of the reconstructed source to a circle whose radius is the distance from the centre (pixel with maximum intensity) to the farthest ray-traced pixel in the reconstructed source.

In table II.2.1 we show the precision with which we can reconstruct the source for both the images if the exact lens parameters are known. The systematic error is smaller if more pixels are available for inversion or if the S/N is high. The systematics show that the intensity I_e is overestimated and the effective radius R_e and index n are underestimated for the exact lens parameters. The error between the simulated and fitted parameter is smaller for the image with S/N=10 when compared with the image with S/N=3.

Summed square error for the Sérsic fit

We calculate the summed square error (SSE) between the reconstructed source and the Sérsic profile fitted for the reconstructed source. This value serves as an indicator of the goodness of fit and is used in the likelihood calculation. We observe that the SSE is lower for the arc with S/N 3. This is because there are fewer pixels in this arc for inversion compared to arc with higher S/N. We show in sections II.3.3.1 and II.3.3.2 that the SSE of the low S/N arc does not change significantly for change in the lens parameters. Hence, it will not act as an efficient Occam's razor in ruling out the wrong solutions.

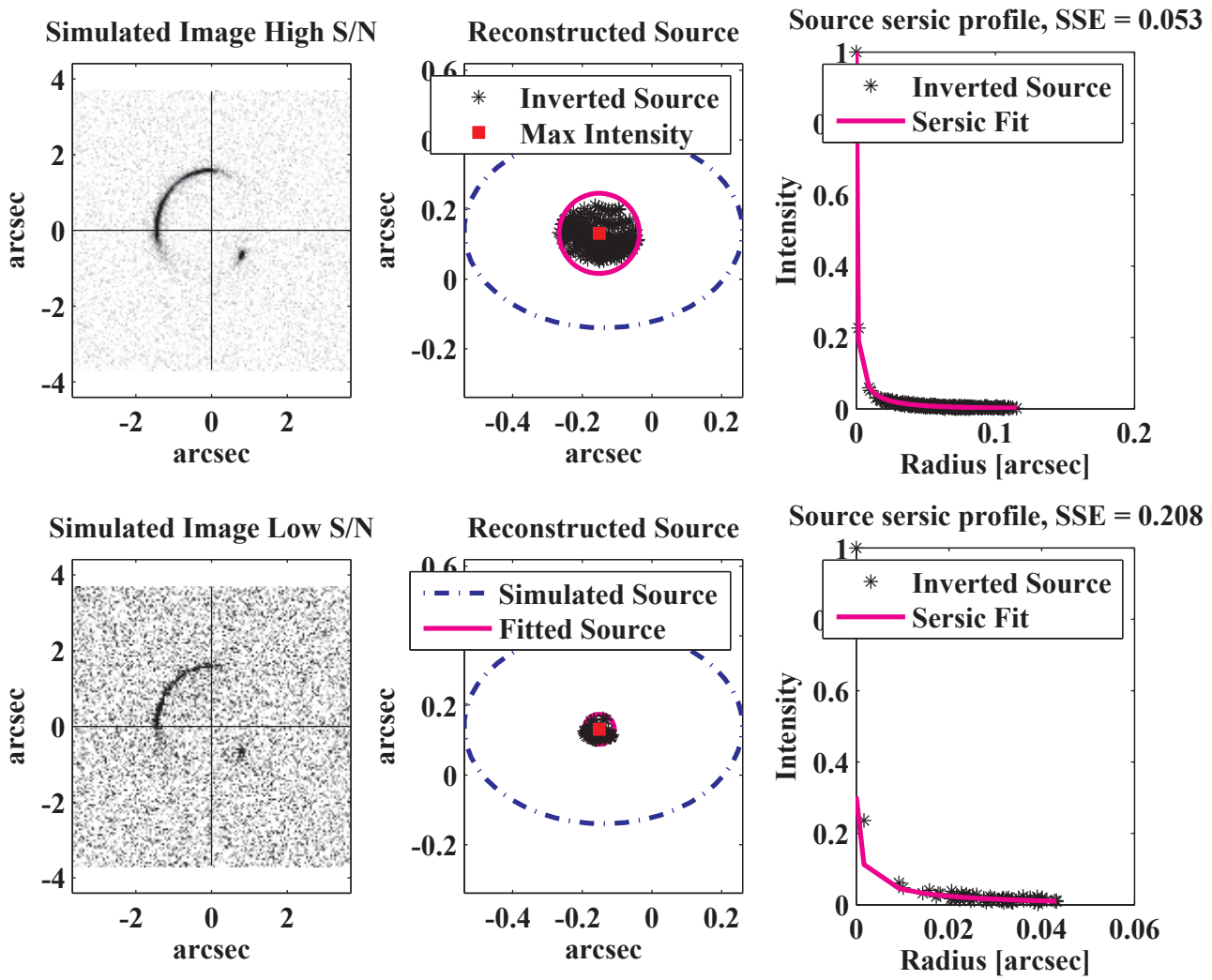

Figure II.2.1: **Sérsic fit for the reconstructed source:** The left panels show the simulated image with two different noise levels. The central panels show the reconstructed source in the source plane for the gravitational arc extracted from the left panel. The central panels also show the simulated source, the fitted source and the point of maximum intensity in the reconstructed source. The right panels are the Sérsic fit for the reconstructed source. The source was reconstructed using the exact simulated lens parameters.

II.2.2.3 Step 3 – Image Reconstruction

After reconstructing the source, we verify whether the reconstructed source produces all and only the observed arcs with observed luminosities. For the given lens parameters and the reconstructed source, we solve the forward problem in lens modelling and find all the lensed images of the source. We recall that the reconstructed source here is the circular approximation made for the Sérsic fit (cf. previous section). The procedure to find the lensed images is same as the one explained in section II.1.6.

Definition of the Reduced Chi–squared

We compute the chi-squared between the observed arcs and the reconstructed arcs, to verify whether the reconstructed source produces all and only the observed arcs. The reduced chi-squared is given by

$$\chi^2_{image} = \frac{1}{N' - n - 1} \sum \frac{(\text{observed image - reconstructed image})^2}{\sigma^2} \qquad \text{(II.2.3)}$$

where N' is the total number of pixels N^2 in the image, n is the total number of fitted parameters and σ^2 is the variance of the noise in the image. If any pixels are masked, the number is subtracted from N^2. The χ^2_{image} value is used in the Likelihood computation for the MCMC analysis.

Example for Image Reconstruction

In figure II.2.2 we show the reconstructed image and the residue image for the gravitational arc simulated in section 2.4. We use the exact lens parameters (cf. table II.1.4) and the reconstructed source (cf. previous section) to reconstruct the image. The reduced chi-squared is close to one in both the cases of S/N.

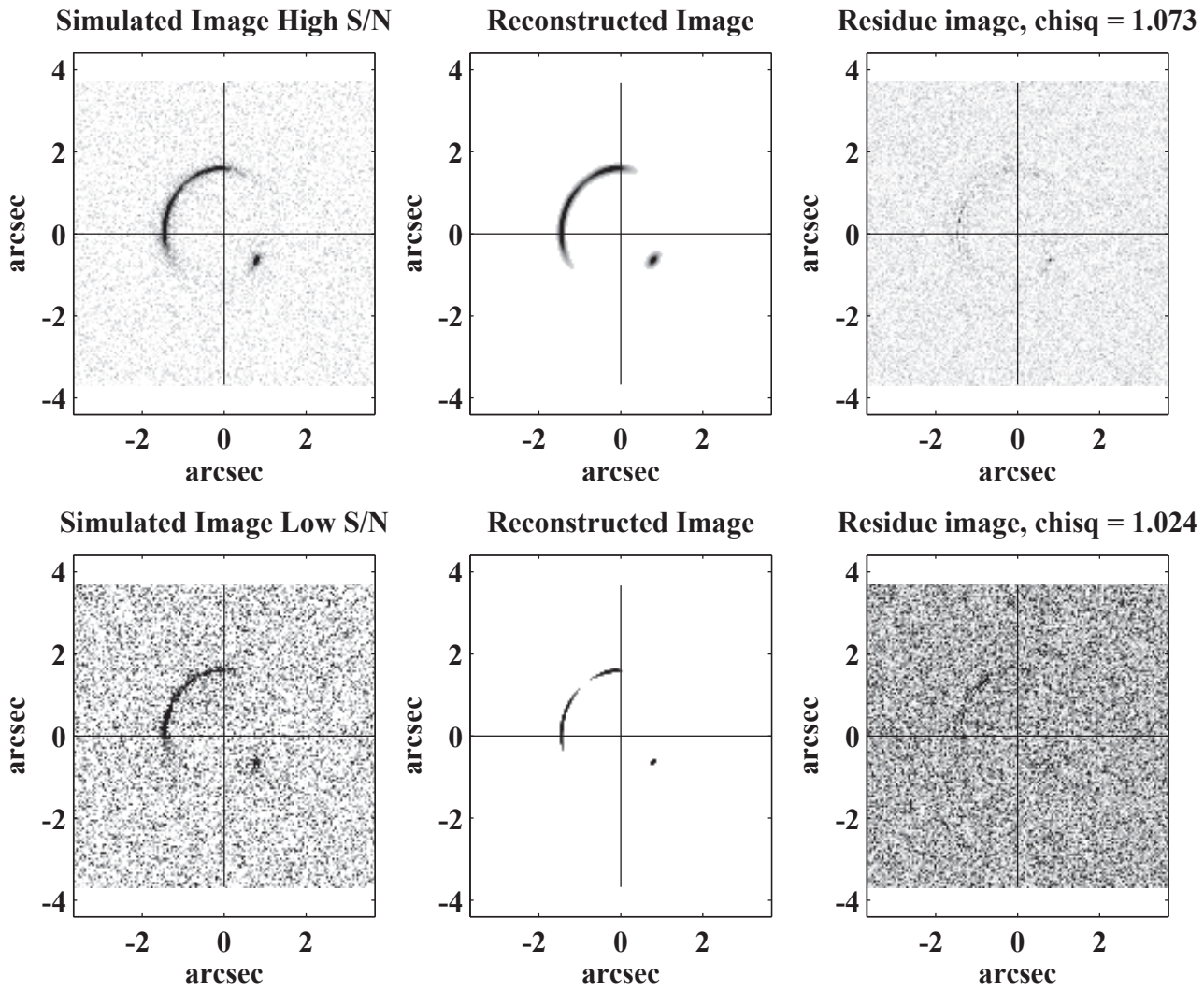

Figure II.2.2: **Residue image between the simulated arc and reconstructed arc:** The left panels show the simulated arc with different levels of noise. The centre panels show the arcs computed using the reconstructed source and the exact lens parameters. The right panels show the residue image between the simulated arc and reconstructed arc.

II.2.2.4 Step 4 – Compute the Likelihood Function

We recall from the beginning of section II.2.2 that the posterior probability is directly proportional to the likelihood. Different definitions of likelihood lead to different posterior distributions for the lens and source parameters. We define this likelihood as a function of the SSE of the source and reduced chi-squared of the image.

$$Likelihood = \exp\{-|1 - \chi^2_{image}| - SSE\} \tag{II.2.4}$$

The Likelihood is defined in such a way that it is equal to one when reduced chi-squared $\chi^2_{image} = 1$ and summed squared residuals SSE ≈ 0. These values correspond to the best fit for the lens and source. This definition of likelihood does not enforce rigorous regularization. But we find that the posterior distributions computed using this likelihood is sufficient to constrain the lens and source parameters. We compute the likelihood for a large but finite sample of lens parameters in the prior. In the next section we explain how we compute the posterior distribution for the lens and source parameters.

II.2.2.5 Step 5 – Posterior Distribution for the Lens and Source Parameters

We use the likelihood of the large number of randomly sampled lens parameters from the prior distribution and compute the posterior distribution for the lens and source parameters by creating a Markov Chain using the Metropolis–Hastings algorithm (cf. Metropolis et al., 1953; Hastings, 1969). The algorithm is used to accept or reject each sample based on its likelihood. A brief description of the algorithm is as follows. For two consecutive samples s_i and s_{i+1} in the prior distribution, the sample s_{i+1} is accepted unconditionally if the likelihood of s_{i+1} is greater than the likelihood of s_i. Otherwise s_{i+1} is accepted with a probability that is the ratio of the likelihood of s_i to the likelihood of s_{i+1}. About 15% of the accepted samples at the start of the Markov-Chain are discarded to allow the chain to set into a equilibrium

state. The distribution of the remaining accepted samples is the posterior probability distribution for the lens and source parameters.

II.2.3 Summary

In this chapter we presented our method to find a solution to the inverse problem in gravitational lens modelling. We showed how we compute a probability distribution for the lens and source parameters using statistical inference. The actual MATLAB[1] and PYTHON[2] routines we wrote for finding the probability distribution for the lens and source parameters of a given gravitational arc can be found at GITHUB. In the APPENDIX we present brief guidelines for using the routines. In the next chapter we test our method on simulated gravitational arcs to verify the precision with which we can recover the simulated parameters. Once we understand the systematics in our method we can use it to model real observed gravitational lenses.

[1] https://github.com/balaonspace/invertStrongLens–Matlab
[2] https://github.com/balaonspace/invertStrongLens–Python

Chapter II.3

Demonstration of our Method on Simulated Gravitational Arcs

In this chapter we apply our method for solving the inverse problem to simulated gravitational arcs. We study with what accuracy and precision we can recover the simulated parameters using our method. This exercise is important to convince ourselves that our method provides rigorous results, and hence can be used to study real gravitational lenses. We invert the gravitational arc simulated in section II.2.2 and obtain a probability distribution for its lens and source parameters. We test how the number of samples in the prior, the S/N of the arc and degeneracies between various parameters affect the results obtained.

The outline of the chapter is as follows. We begin by recalling some relevant information about the simulated arc. Next, we describe how we choose the prior distribution for all the lens parameters. Then, we compute the posterior distribution for the lens and source parameters using the method described in section II.2.2. Finally, we discuss the results and the major factors that affect our analysis.

II.3.1 Notes on the Simulated Gravitational Arcs

In section II.1.6 we described our method to simulate gravitational arcs for a given lens and source parameters. In figure II.1.4 we showed the simulated arcs for a set of arbitrary lens and source parameters presented in table II.1.4. We added two different levels of gaussian noise to the simulated arcs. The noise levels were chosen to show how the results of the inversion technique are affected by the presence of noise and number of pixels used for inversion. The S/N of the extracted arcs are 10 and 3 after the addition of noise. We recall that in the observed arc, we use only the pixels whose S/N is above 5 for source reconstruction. There were 336 pixels available for inversion in simulated arc with S/N=10 and 68 pixels for simulated arc with S/N=3. The S/N of individual pixels are higher than that of the extracted arc. In the next section we describe how we choose a prior distribution for all the lens parameters.

II.3.2 Prior Distribution for the Lens Parameters

The prior distribution is chosen only for the lens parameters. There are no explicit priors for the source parameters. As previously mentioned in section II.2.2.1, we choose a uniform distribution in a finite interval $[a, b]$ as the prior for the lens parameters. The uniform distribution is a maximum entropy probability distribution. By choosing a uniform prior we assign equal probability for all the values in the interval $[a, b]$. In absence of any evidence to assign higher probabilities to some values, uniform prior is the conservative option. The guidelines used to choose the interval $[a, b]$ for each lens parameter is detailed below.

The Einstein radius is constrained by the distance between the center of the lensing galaxy and position of the counter images.

The axis ratio is constrained between $0.5 < f < 1$. Expected values for most lenses lie in this regime. We recall that $f = 1$ corresponds to a spherical lens. Care should be taken if the observation suggests an unusually slender lens i.e. f<0.5.

The core radius is constrained between $0 < b_c < 0.5$, which includes all possible

values for the core radius.

The position angle can be constrained by the position angle of an isophotal ellipse of the lens galaxy or a broader constraint would be to sample between $[-\pi/2, \pi/2]$, which includes all possible values for the position angle.

The external shear $\gamma = \gamma_1 + i\gamma_2$ is unknown but is assumed to be small unless a massive object is identified close to the lens. Therefore, it is constrained between $-0.1 \leq \gamma_1, \gamma_2 \leq 0.1$. If very high shear is needed to model the lens, the source for the shear should be identified by analysing the wide field image for massive neighbouring groups and clusters.

We calculate the mean μ and standard deviation σ for the chosen prior distribution.

II.3.3 Posterior Distribution of the Lens and Source Parameters

The posterior distribution is obtained by following the method described in section II.2.2. The likelihood is computed for a set of randomly chosen lens parameters from the prior distribution defined in the previous section. Then using Metropolis–Hastings algorithm defined in section II.2.2.5 the samples in the prior distribution are either accepted or rejected. Around 15% of the accepted samples at the beginning of the Markov-Chain are discarded to allow the chain to set into a equilibrium state. The remaining samples form the posterior distribution of the lens parameters. The posterior distribution of the source parameters are given by the parameters of reconstructed source for the accepted lens parameters. The mean and standard deviation of the posterior distribution is calculated and the values are compared with the prior distribution and the simulated parameters. We present the posterior results for the two simulated arcs in table II.3.1.

In general the posterior distribution is accepted if the variance[1] of the posterior

[1]We would like to clarify that in tables we provide the standard deviation σ of the posterior distribution, and in the text we use the term variance which is simply σ^2.

Table II.3.1: Posterior Distribution of Lens and Source Parameters for Simulated Gravitational Arcs with S/N=10 and S/N=3

Parameter	Simulated	Prior Distribution			Posterior Distribution S/N=10		S/N=3	
		Uniform	μ	σ	μ'	σ'	μ'	σ'
R_{Ein}	1.60	$[1, 2]$	1.5	0.29	1.74	0.06	1.66	0.19
f	0.80	$[0.5, 0.99]$	0.75	0.14	0.79	0.06	0.81	0.07
b_c	0.20	$[0, 0.5]$	0.25	0.14	0.31	0.03	0.25	0.15
θ_{LENS}	0.69	$[0, \pi/2]$	0.78	0.45	0.66	0.11	1.04	0.29
γ_1	0.05	$[-0.1, 0.1]$	0	0.06	0.05	0.01	0.02	0.02
γ_2	0.00	$[-0.1, 0.1]$	0	0.06	0.02	0.02	0.02	0.06
n	4				3.47	0.07	3.00	0.13
R_{eff}	0.20				0.13	0.06	0.12	0.02
y_1	0.14				-0.13	0.02	-0.12	0.03
y_2	0.14				0.11	0.03	0.15	0.03
I_e	6				7.28	0.74	19.06	5.12

The horizontal line in the middle of the table separates the lens parameters (top) from the source parameters (bottom).
cf. section 2.1 and 2.2 for the definition of the parameters.

distribution is lesser than the variance of the prior distribution. Smaller variance implies a higher confidence limits on the lens and source parameters. In table II.3.1 we can see that the posterior variance is smaller than the prior variance for most of the lens parameters in both the cases. For these lens parameters the value is constrained by the posterior distribution. Because, no prior can possibly be made for the source parameters, our rejection criteria on source models are physically motivated by the expected parent population of the galaxies at similar redshifts.

We discuss the posterior results for the lens and source parameters separately below. We compare the posterior results between the simulated arc with S/N=10 and S/N=3.

II.3.3.1 Posterior Results for the Lens Parameters

In figures II.3.1 and II.3.2, we present the posterior distribution of the lens parameters for the simulated arc S/N=10 and S/N=3 respectively. We discuss below how rigorously each parameter has been constrained for two different noise levels S/N=10 and S/N=3.

The Einstein radius and axis ratio of the lens are constrained for both S/N 10 and S/N 3. The posterior variance is smaller than the prior variance and the simulated value is recovered within 1σ deviation of the posterior distribution.

In case of the core radius the posterior variance is strongly constrained for S/N 10 but it is not constrained S/N 3. The simulated value of the core radius is not recovered within the 1σ deviation for both the cases. The shift in the mean of the posterior distribution compared to prior, suggests our method can distinguish between a flat core and cuspy one. We discuss the degeneracy between the Einstein radius and core radius in section II.3.3.3.

The position angle of the lens is constrained for S/N 10 and the simulated value is recovered within 1σ deviation. But for S/N 3 the posterior variance is only slightly lesser than the prior variance, hence it is only weakly constrained. We highlight the degeneracy between the position angle and external shear in section II.3.4.3.

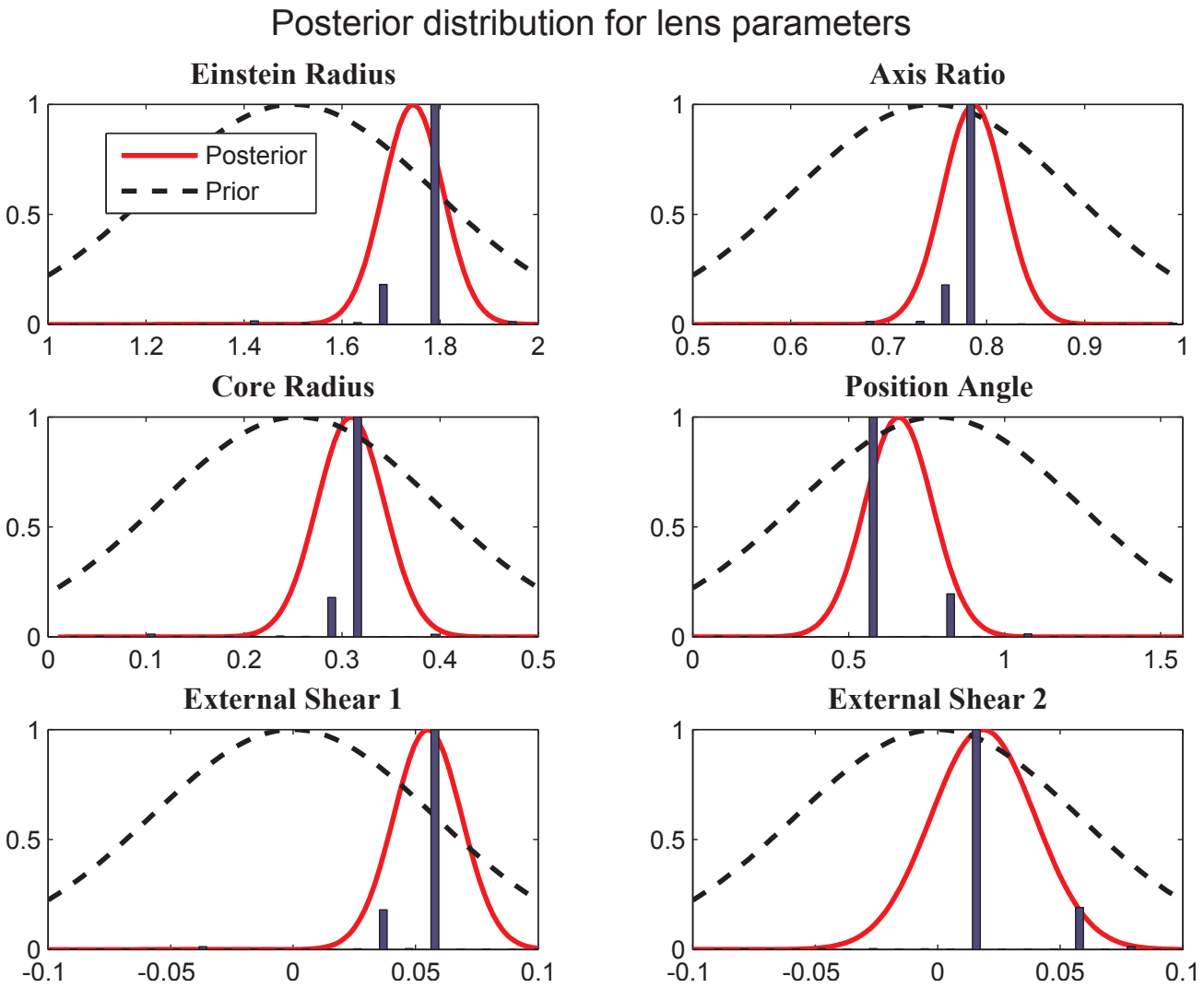

Figure II.3.1: **Posterior distribution for the lens parameters of the simulated arc with S/N 10:** The black–dotted line is a normal approximation for the prior distribution. The histogram is obtained using the method described in section II.2.2. The red–solid line is a normal approximation for the histogram. Since only ∼50 out of the 10^5 samples were accepted for the posterior distribution, the histogram does not look Gaussian for all the parameters. Consult section II.3.3.1 for interpretation of results.

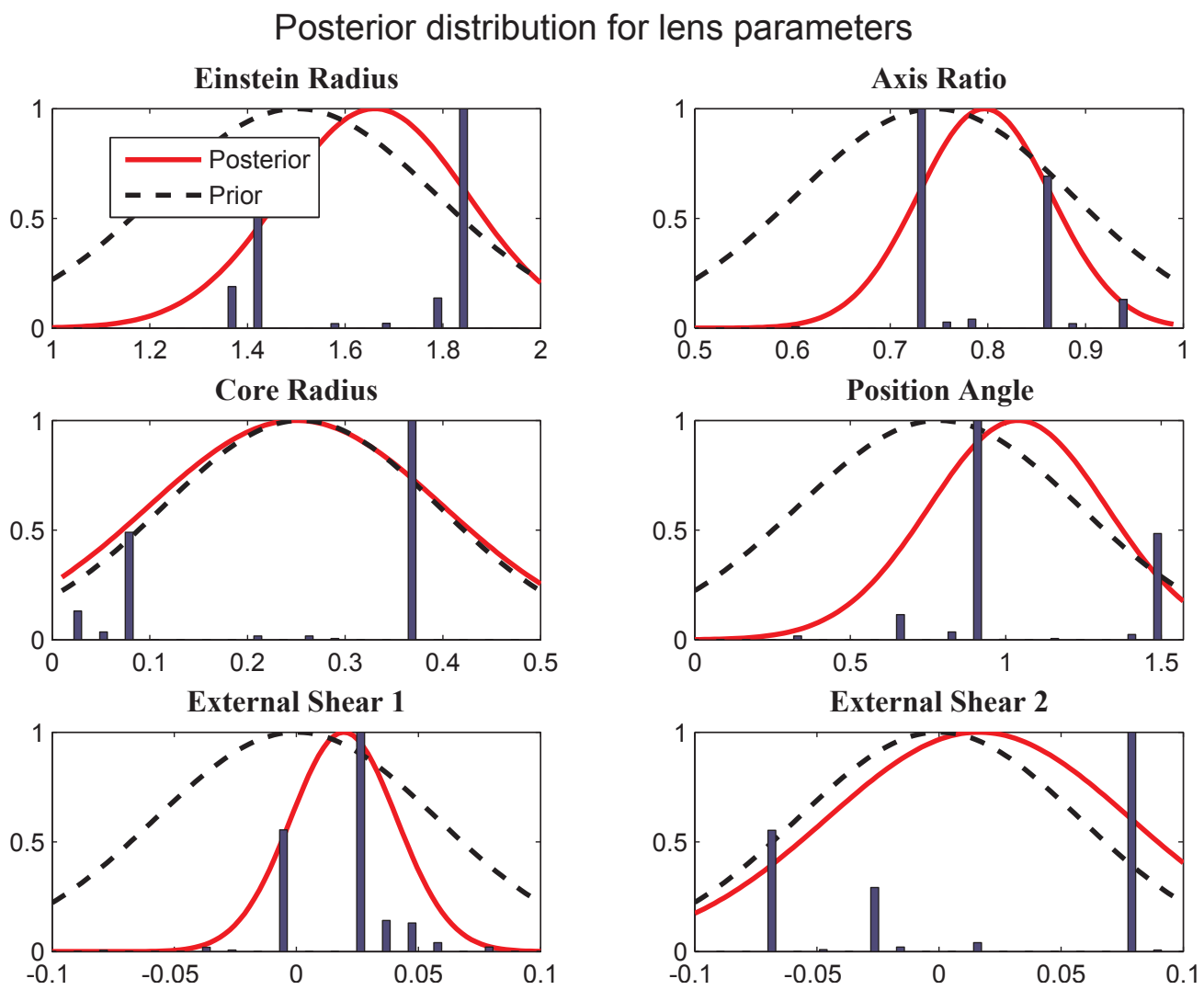

Figure II.3.2: **Posterior distribution for the lens parameters of the simulated arc with S/N 3:** The black–dotted plot is a normal approximation for the prior distribution. The histogram is obtained using the method described in section II.2.2. The red–solid plot is a normal approximation for the histogram. Since ∼1600 out of the 10^5 samples were accepted for the posterior distribution, the histogram resembles a Gaussian for all the parameters. Consult section II.3.3.1 for interpretation of results.

The external shear is constrained for S/N 10 and the simulated value is recovered within 1σ deviation. But for the S/N 3 the posterior cannot be distinguished from the prior, hence no constraint can be place on the shear.

In general, we learn from the above results, that the constraint on the lens parameters is stronger for the image with high S/N. The posterior variance of all the lens parameters are smaller for S/N 10 when compared to the case S/N 3. We discuss the effect of S/N and number of pixels available for inversion in section II.3.4.3.

II.3.3.2 Posterior Results for the Source Parameters

In figures II.3.3 and II.3.4, we present the posterior distribution of the source parameters for the simulated arc. We discuss below how rigorously each parameter has been constrained for the two different noise levels S/N=10 and S/N=3.

The position of the center of the source is constrained to within a pixel for S/N 10 and within few pixels for S/N 3. And the simulated value is within the 1σ deviation for both S/N.

We recall from section II.1.5 that the Sérsic index can vary between $0.5 < n < 10$. We find the posterior variance of the Sérsic index sufficiently small to constrain the Sérsic index from the posterior distribution obtained. But we find that the simulated value is not recovered within the 1σ deviation for both S/N, but systematically falls below the simulated value. This implies that the value of Sérsic index is underestimated. In section II.3.3.3 we show that we can distinguish between sources with Sérsic index $n = 1$ and $n = 4$.

The posterior variance of the effective radius R_{eff} suggests that this value is constrained to within a few arcsecs for both S/N 10 and S/N 3. But the simulated value is not recovered within the 1σ deviation in the case of S/N=3. This is because the reconstructed portion of the source does not extend up to the effective radius in the case of S/N=3.

The posterior variance of the intensity is reasonably constrained when S/N=10, and the simulated value is recovered within 1σ deviation. For S/N=3, the posterior variance is too large to constrain the intensity.

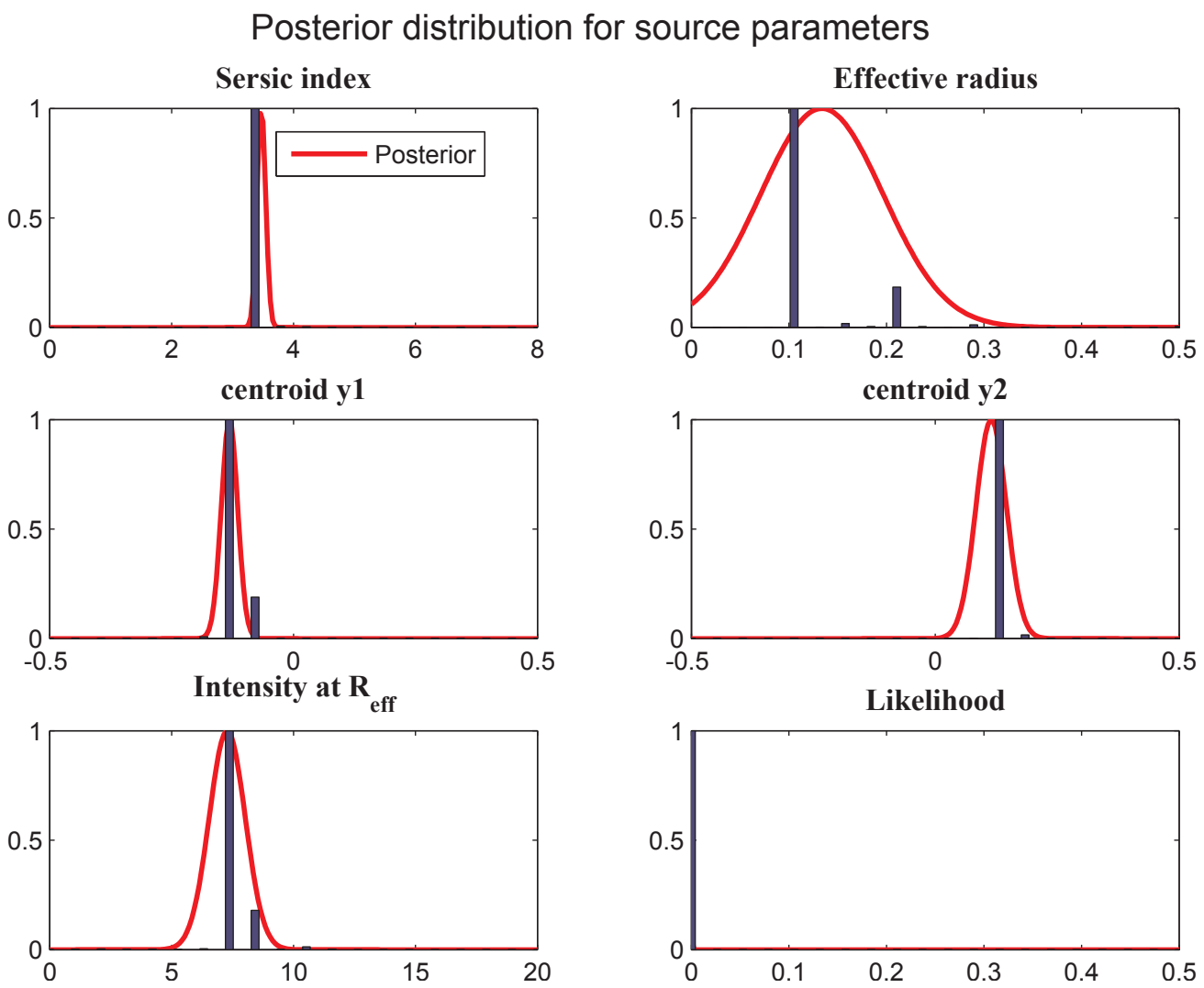

Figure II.3.3: **Posterior distribution for the source parameters of the simulated arc with S/N 10:** The histogram is obtained using the method described in section II.2.2. The red–solid line is a normal approximation for the histogram. Since only $\sim$50 out of the 10^5 samples were accepted for the posterior distribution, the histogram does not look Gaussian for all the parameters. Consult section II.3.3.2 for interpretation of results.

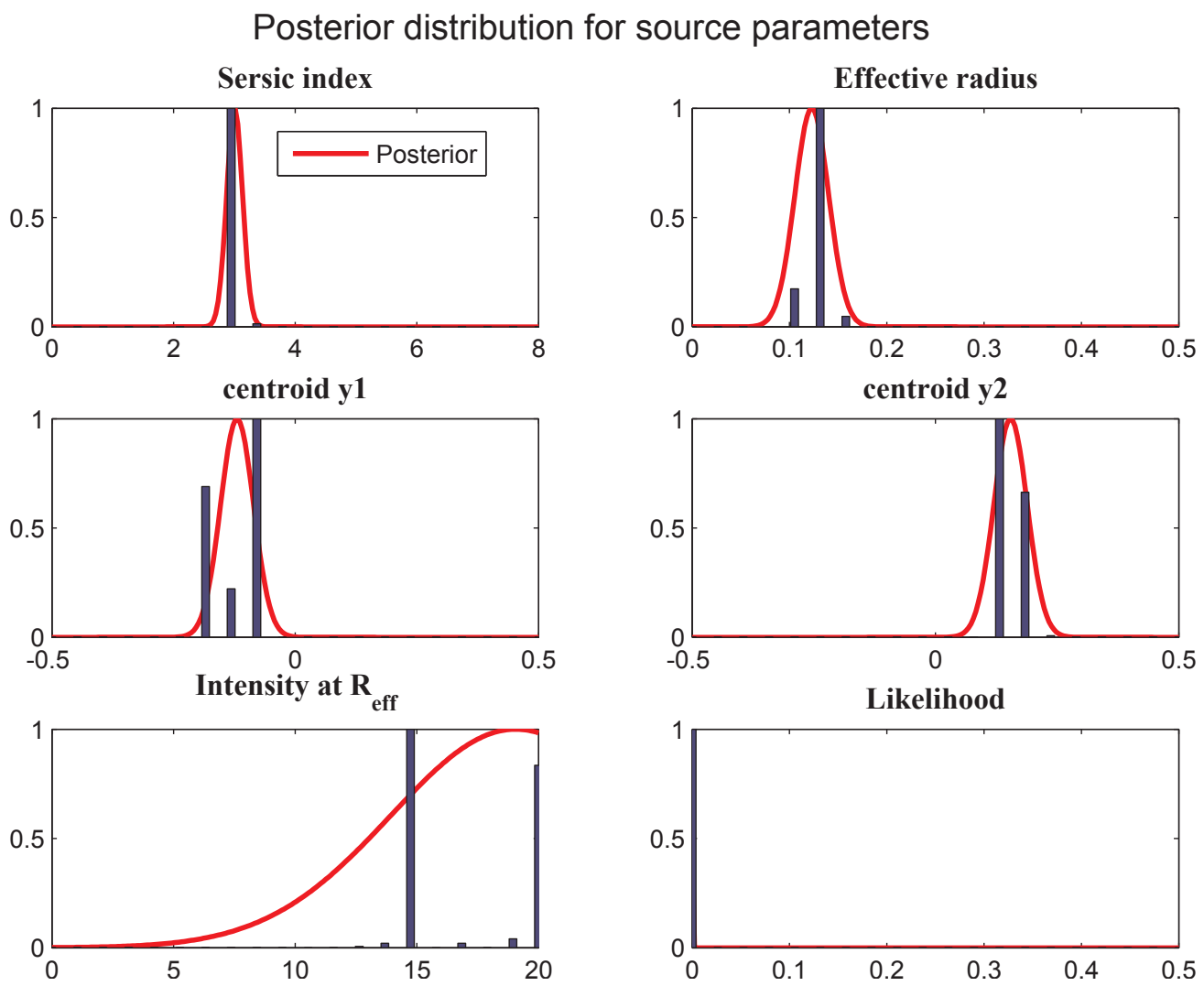

Figure II.3.4: **Posterior distribution for the source parameters of the simulated arc with S/N 3:** The histogram is obtained using the method described in section II.2.2. The red–solid line is a normal approximation for the histogram. Since ∼1600 out of the 10^5 samples were accepted for the posterior distribution, the histogram resembles a Gaussian for all the parameters. Consult section II.3.3.1 for interpretation of results.

Table II.3.2: Posterior Distribution of Sérsic index for various simulated values

Simulated value	Posterior Distribution	
Sérsic index,n	μ'	σ'
1	1.27	0.15
4	3.47	0.07

II.3.3.3 Constraining the Sérsic index

We mentioned in the previous section that the simulated value of the Sérsic index is not recovered within the 1σ deviation of the posterior distribution for both S/N=10 and S/N=3. But the variance of the posterior is small when compared to the range of possible values for the Sérsic index $0.5 < n < 10$. We simulated sources with different values of Sérsic index to study how precisely they were constrained by our method. We simulated gravitational arcs with same lens and source parameters given in table II.1.4, except for the Sérsic index. We chose Sérsic index, $n = 1$, and repeated the analysis to find how well they were recovered. We present the results in table II.3.2.

We find that the mean value of the Sérsic index is slightly overestimated for $n = 1$, and underestimated for $n = 4$. The discrepancy in Sérsic index estimation could be attributed to under sampling of the intensity in the source plane and presence of noise. Even though we will not be able to constrain the exact Sérsic index, using table II.3.2 as a reference we can distinguish between galaxies with exponential profile ($n = 1$) and de Vacouleur profile ($n = 4$).

II.3.4 Factors Affecting the Posterior Distribution

The major factors that influence the posterior distributions are the number of prior samples in the MCMC method, signal-to-noise ratio of the arc, number of pixels available for inversion and degeneracies intrinsic to lensing. We discuss the effects of these on the results obtained for our simulated gravitational arcs.

II.3.4.1 Number of Samples in MCMC

Ideally the histogram of the posterior distribution will tend towards a smooth distribution as the number of samples in the prior increases. But practical difficulties impose a upper bound on the number of samples. We find the optimal number of samples to be $\sim 10^5$. For 10^5 samples, the total number of samples accepted for the posterior distribution is in the order of 50 for S/N 10 and 1600 for S/N 3. This implies that only 0.05% and 1.6% of the initial samples were accepted. The posterior distribution was fitted for this proportion of the samples. It is computationally expensive to increase the samples by an order of magnitude to 10^6. For a sample size lesser than 10^5, there will not be sufficient samples in the posterior to define its mean and variance. Therefore, we always perform MCMC analyses with 10^5 samples.

II.3.4.2 S/N and Number of Pixels

In gravitational lensing the presence of noise and the intrinsic faintness of the background source affect the number of pixels extracted from the arc for inversion. We added different amount of noise to the same gravitational arc and found as expected that the number of pixels available for inversion decreases with decrease in S/N. Instead if a bright and a faint arc are simulated with same noise, the brighter arc will have a higher S/N compared to the fainter and we will find that the number of pixels available for inversion is lesser for the fainter arc.

From the results given in table II.3.1, we conclude that the variance of the posterior distribution will be larger for the image with low S/N. We also conclude that the the variance of the posterior distribution will be larger if only few pixels can be extracted from the arc for inversion. The results also suggest as S/N or number of pixels decreases, at some point the posterior distribution will become indistinguishable from the prior. We recall that for the simulated arc with S/N=3, which had 68 pixels in the extracted arc for inversion, the posterior distribution is not distinguishable from the prior for most of the lens parameters (cf. figure II.3.2). With this in mind, we applied our method to real lenses for which there were at least 50 pixels in the extracted arc available for inversion.

II.3.4.3 Degeneracies in the Lens Model

We have already stated that the mean or mode of the posterior distribution is not exactly equal to the simulated value for any of the lens and source parameters. The main cause for such deviation is the presence of correlation between various lens parameters. In figure II.3.5 we show the existence of strong correlation between some of the lens parameters.

In left panel of the figure II.3.5, we show the existence of strong correlation between the Einstein radius and the core radius. The correlation coefficient computed between these two parameters is 0.99. For the simulated arcs, the posterior variance of the core radius is only slightly smaller than the prior variance, but the mean of the posterior distribution has shifted towards the simulated value. Even though we cannot constrain the core radius, we can say whether the lens has a flat core or a cusp at the centre.

In the right panels of the figure II.3.5, we show the correlation between axis ratio and external shear, and the correlation between position angle and external shear. This degeneracy can be lifted if the source of the external shear is identified.

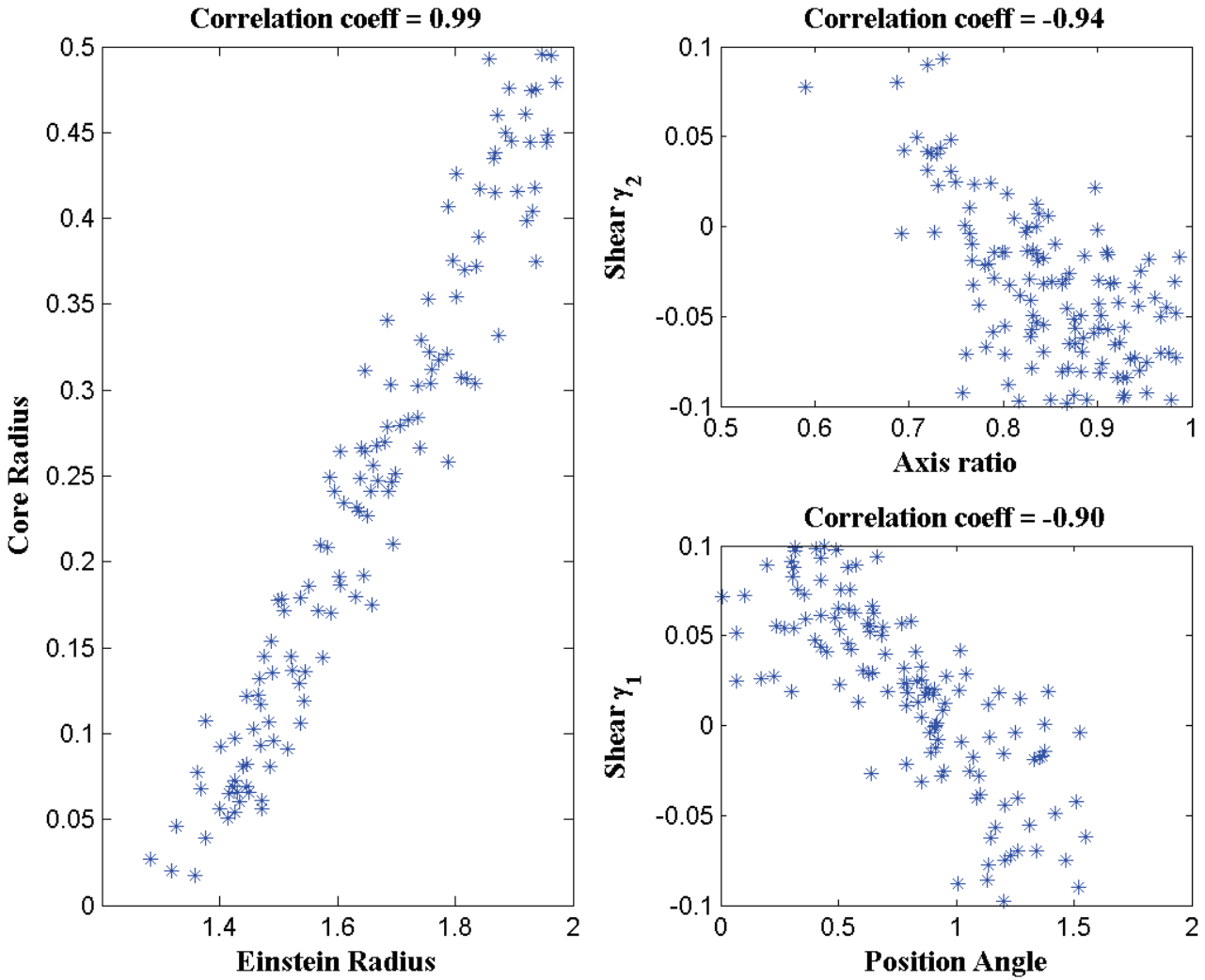

Figure II.3.5: **Correlation between various lens parameters:** The scatter plot on the left panel shows the existence of strong correlation between the Einstein radius and core radius of the lens. The scatter plots on the right panel show the existence of strong correlation between the axis ratio, position angle of the lens and shear.

II.3.5 Summary

In this chapter we applied our inversion method to simulated gravitational arcs and showed with what precision we recovered the simulated parameters. We find that the parameters are strongly constrained for simulated arcs with higher S/N. We discussed the degeneracies intrinsic to lensing, and how they can be lifted. In the next chapter we apply our method to real observed gravitational lenses and model their lens mass profiles and source light profiles.

Chapter II.4

Lens and Source Parameters of Observed Gravitational Arcs

In this chapter we apply our method to observed gravitational arcs and compute the mass profile of the lenses and light profile of the sources. We invert a selection of lenses from the *Strong Lensing Legacy Survey* (cf. Cabanac et al., 2007) and *Sloan Lens ACS Survey* (cf. Bolton et al., 2006). These two lens discovery programs combined together contain the largest fraction of known strong lenses. Therefore, we are more likely to find gravitational arcs with high S/N in them. We applied our method to a total of 9 lenses. We obtained acceptable results for 6 of them and we rejected the results obtained for the remaining 3.

The outline of this chapter is as follows. First, we present briefly the SL2S and SLACS discovery programs. Next, we present the chosen strong lenses and their observational properties. Then, we present the posterior distributions of the lens and source parameters by modelling the lens as a nonsingular isothermal ellipsoid (NIE) and nonsingular isothermal sphere (NIS). Both models have external shear added to them. Finally, we discuss the reasons for accepting or rejecting the posterior distribution of the lens and source parameters.

II.4.1 Brief Account on the Strong Lensing Discovery Programs

A comprehensive list of all strong lens discovery programs and all known strong lens candidates can be found in the MASTER LENS DATABASE[1]. We present here a brief description of two discovery programs the SL2S and the SLACS.

II.4.1.1 The Strong Lensing Legacy Survey

The Strong Lensing Legacy Survey (SL2S) provides a list of strong lenses discovered from the images gathered by the Canada-France-Hawaii Telescope Legacy Survey (CFHTLS). Cabanac et al. (2007) and More et al. (2012) used automated tools to detect gravitational arcs and rings in these images. Today the SL2S program has discovered 170 promising candidates and 60 confirmed lenses, after searching a total of 171 $\deg^2$ in four patches of the sky. CFHTLS provides images of the discovered lenses in at least 3 broadband filters. HST follow-up was carried out for more than half of the confirmed lenses in the sample. One important difference between the SL2S and SLACS program is, SL2S lenses have Einstein radius upto $15''$ (cf. Cabanac et al., 2007) , while the maximum value for the SLACS is limited to $3''$. We discuss the reason for the limitation in next section. Some interesting results obtained from SL2S lenses are presented below.

Limousin et al. (2009) performed a joint strong and weak lensing analysis on 13 group-scale lenses and constrained their dispersion velocities. Gavazzi et al. (2012) modelled 15 galaxy-scale lenses, and find that the lens model requires substantial amount of external shear ($\gamma = 0.12 \pm 0.05$) to explain the observed arcs. Ruff et al. (2011) modelled 11 lenses, and find the fraction of dark matter within half the effective radius to be $0.42^{+0.08}_{-0.08}$ with a scatter of $0.20^{+0.09}_{-0.07}$. Sonnerfeld et al. (2013a,b) investigate the cosmic evolution of the internal structure of massive early-type galaxies using the photometric and lensing measurements made using the SL2S sample.

[1] `http://masterlens.astro.utah.edu`

II.4.1.2 The Sloan Lens ACS Survey

The Sloan Lens ACS Survey (SLACS) provides a list of strong lenses discovered by analysing the spectroscopic data from the *Sloan Digital Sky Survey* (SDSS). The lens candidates were selected by looking for multiple nebular emission lines at a redshift significantly higher than that of the SDSS target. Bolton et al. (2008) followed up these candidates using HST and confirmed the discovery of 19 strong gravitational lenses. The HST/ACS images of the SLACS lenses consist of 420s Wide Field Channel (WFC) exposure in filters F435W and F814W. Today there are 88 confirmed lenses in the SLACS database. The reason why the Einstein radius of SLACS lenses are limited to $3''$ is because the diameter of the fiber used for spectroscopy in SDSS is only $3''$ wide. Some interesting results obtained from the SLACS lenses are given below.

Treu et al. (2006) discuss the selection effects in SLACS data and investigate the distribution of the lenses in the fundamental plane. Koopmans et al. (2006) find that the mass profile of SLACS lenses are well described by an isothermal profile, the average value of the Einstein radius is 4.2±0.4 kpc and the fraction of dark matter withing the Einstein radius is 0.25±0.06. Gavazzi et al. (2007) performed a joint strong and weak lensing analysis on the SLACS lenses. Treu et al. (2009) study the relation between the environment and internal structure of early type galaxies. Auger et al. (2009) compute the the stellar mass of all the SLACS lenses and use the value to estimate the fraction of dark matter present in the lenses.

II.4.2 Notes on the Selected Lenses

We selected 1 lens from the SL2S and 8 lenses for which the S/N of the arc is high enough to model both the lens and the source. Table II.4.1 presents the known observational properties for the selected lenses. The properties listed are the deflector redshift z_d, source redshift z_s, dispersion velocity σ_v and the HST image used for inversion. The values were obtained from Bolton et al. (2006) for the SLACS lenses and Tu et al. (2009) for the SL2S lens. Below we discuss the notable features of the

Table II.4.1: Observed properties of the lenses

Lens	z_d	z_s	σ_v $[km\,s^{-1}]$	Image Used
SL2S J0217–0513	0.6459	1.8470	na	HST/ACS F606
SLACS J0737+3216	0.3223	0.5812	310±15	HST/ACS F814
SLACS J0959+0410	0.1260	0.5350	212±12	HST/ACS F435
SLACS J1205+4910	0.2150	0.4808	234±10	HST/ACS F435
SLACS J1420+6019	0.0629	0.5350	194±5	HST/ACS F814
SLACS J1627–0053	0.2076	0.5241	275±12	HST/ACS F814
SLACS J0956+5100	0.2405	0.4700	299±16	HST/ACS F435
SLACS J2303+1422	0.1553	0.5170	260±15	HST/ACS F814
SLACS J2321–0939	0.0819	0.5324	236±07	HST/ACS F814

We obtained acceptable results for the first 6 lenses and rejected the posterior distribution of the last 3.

extracted the arcs in the selected lenses.

II.4.2.1 SL2S J0217-0513

Tu et al. (2009) present the discovery and observational properties of SL2S J0217-0513. They also modelled SL2S J0217-0513 as a singular isothermal sphere using LENSTOOL(Jullo et al., 2007). In figure II.4.1 we show the HST/ACS F606 image of the lens, observed as a part of SL2S follow-up programme SNAP10876 (PI Kneib). We used the tool SEXTRACTOR (Bertin and Arnouts, 1996) to extract the main lensing galaxy from the image, and the extracted lensing galaxy is used as a mask on the observed image (cf. figure II.4.1). This allows us to see the gravitational arc and counter images clearly. For solving the inverse problem we select only the pixels above S/N of 5 from the extracted arc. Spurious pixels above the S/N threshold but away from the arc were removed by visual inspection.

Photometric data presented in Tu et al. (2009) suggests that the main lensing galaxy L0 images two sources S1 and S2 at different redshifts ($z_{S1} = 1.847$ and $z_{S2} = 2.9$). Also the redshift of S2 suggests that it could be lensed by both the

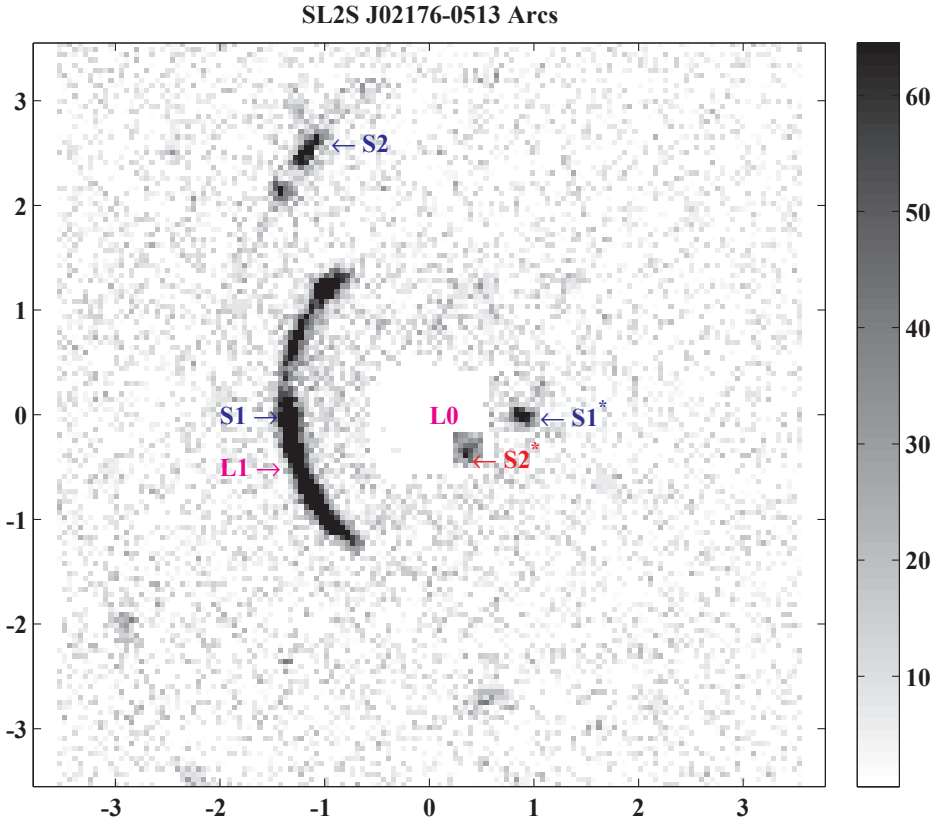

Figure II.4.1: **Gravitational Lens SL2S J02176-0513:** This figure shows the lensed images of SL2S J02176-0513. The main lens labeled L0 is masked in the figure and the images are labeled {S1, S1*, S2, S2*}. The redshifts of the sources S1 and S2 suggest that source S1 will also act as a lens (L1) for source S2.

primary lens L0 and an intermediate lens L1 which is the source of the bright arc S1. This allows us to perform four separate analysis on the image and obtain independent constraints on the lenses {L0,L1} and sources {S1,S2} .

First, we inverted the arc S1 using a NIE model for the lens L0. This allows us to constrain the lens and source parameters of L0 and S1. Second, we inverted both $\{S1, S1^*\}$ using a NIE model for the lens L0. Assuming that $\{S1, S1^*\}$ are counter images provides stronger constraints on the lens and source parameters of L0 and S1. Third, we inverted $\{S2, S2^*\}$ using a NIE model for lens L0. This allows us to obtain an independent constraint on the lens parameter L0, which can compared with $\{S1, S1^*\}$ inversion. It also gives the source parameters of the source S2. Finally, we inverted $\{S2, S2^*\}$ using double plane lens configuration. Now, we have 3 separate constraints on the lens L0 and one constraint on the lens L1.

The S1 and $\{S1, S1^*\}$ inversion using NIE model for the lens yielded comparable results. The constraints on the lens parameters and source parameters were better for $\{S1, S1^*\}$. We present the results in detail in section II.4.3.1. We also inverted the $\{S1, S1^*\}$ configuration using a NIS lens model and compare the results to that of the NIE model.

The posterior results for $\{S2, S2^*\}$ inversion and the double plane inversion did not yield valuable results. The posterior distribution of the lens parameters were not distinguishable from the prior. The main reasons for obtuse results are, first there is no strong evidence to suggest that $S2^*$ is really a counter image of S2, second the of flux $S2^*$ is contaminated by the main lens galaxy and lastly the number of pixels available for $\{S2, S2^*\}$ inversion is only 50. We showed in section II.3.4 that the posterior distribution becomes indistinguishable from the prior distribution as the number of pixels available for inversion drops.

II.4.2.2 SLACS lenses

The discovery and observational properties of the 8 SLACS lenses we selected for inversion can be found in Bolton et al. (2006). We summarize the relevant facts here. Bolton et al. (2006) use a b-spline fit to model the radial profile of the main

lens galaxy. We use their fit to subtract the lensing galaxy from the observed image. In figure II.4.2 we present the HST/ACS images of the SLACS gravitational arcs we selected for inversion.

Spectroscopic and photometric data suggests the presence of only one foreground lens and one background source for theses lenses, as opposed to the SL2S case. The arcs are extracted for inversion by selecting the pixels which have a S/N above 5. Spurious pixels away from the arc are removed by visual inspection. Most lenses have an elongated arc and a counter image. SLACS J1627–0053 and SLACS J2321–0939 have a ring-shaped structure, implying the source is almost exactly behind the lens.

We modelled all the lenses using a NIE model. We obtained acceptable results for five of the lenses and rejected the results for the remaining three as unfeasible. We also inverted the lenses using a NIS model to compare the results. We present the results in detail in section II.4.3.2. For sake of convenience, we split the SLACS lenses we selected into two sets. The lenses for which we obtained acceptable results are placed in Set–1 and the others in Set–2.

The SLACS lenses in Set–1 are J0737+3216, J0959+0410, J1205+4910, J1420+6019 and J1627-0053.

The SLACS lenses in Set–2 are J0956+5100, J2302+1422 and J2321-0939.

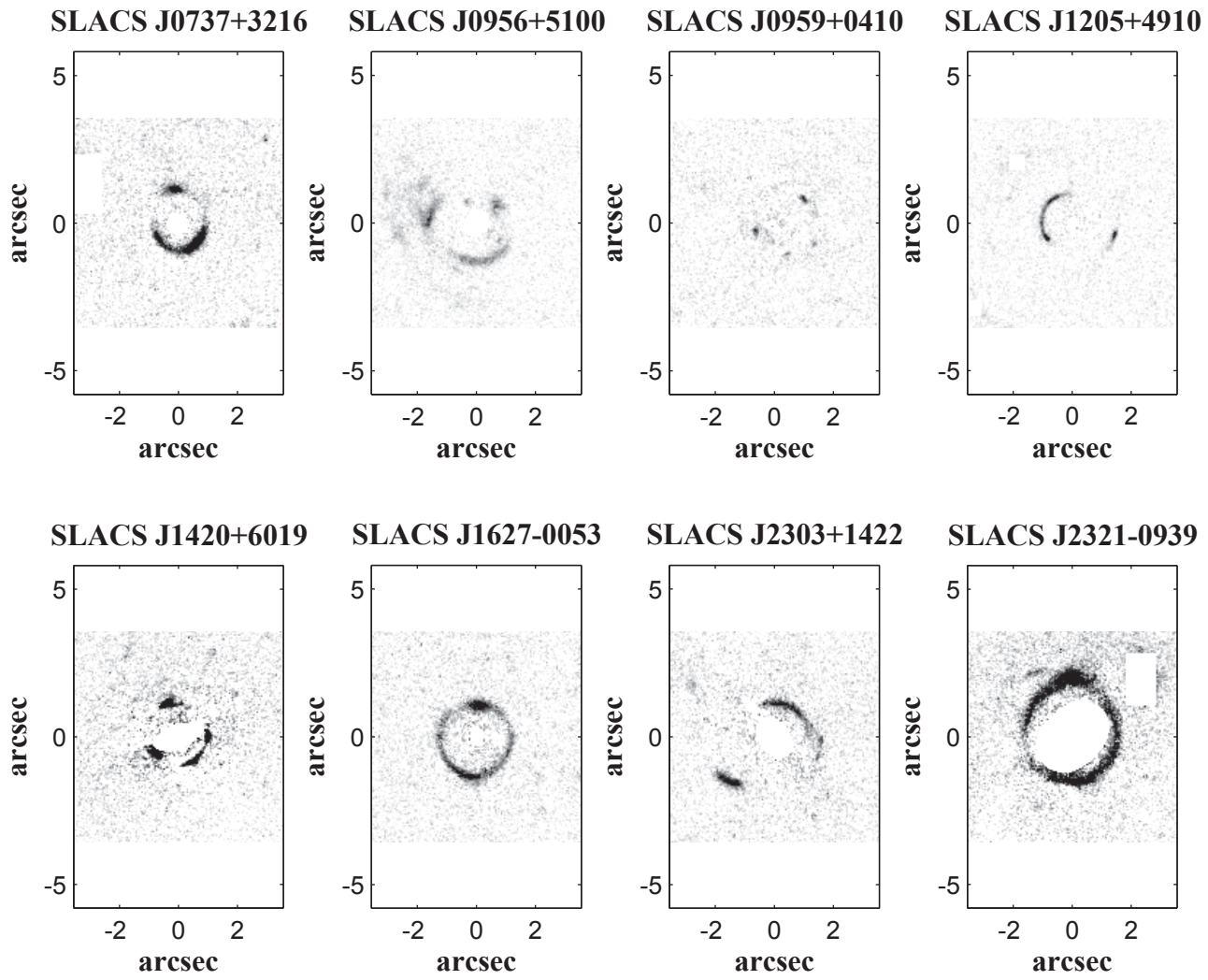

Figure II.4.2: **SLACS Lenses:** This figure presents 8 lenses in the SLACS survey for which we applied our inversion technique. The lens galaxy is subtracted and regions with obscure noise are masked in the image.

II.4.3 Results – The Posterior Distribution

II.4.3.1 Posterior distribution for lens and source parameters of SL2S J0217-0513

In table II.4.2 we present the posterior distribution of the lens and source parameters for the gravitational arc SL2S J0217-0513. We modelled the lens as both a nonsingular isothermal ellipsoid (NIE) and nonsingular isothermal sphere (NIS), with external shear added in both the models. The posterior distribution for the lens and source parameters are given in table II.4.2.

Posterior Results for Lens Parameters

For the NIE model the posterior variance is smaller than the prior variance for the Einstein radius, axis ratio and external shear. These parameters have been rigorously constrained. On the other hand, the core radius and position angle are only weakly constrained. The correlation coefficient between the Einstein radius and core radius is ~ 0.88. Therefore, the core radius is also not rigorously constrained, nevertheless the mean of the posterior reveals a tendency to a flatter core than a cuspy one. The position angle of the lens is not well constrained because the axis ratio of the lens is close to that of a circle. The NIE model requires a non negligible amount of shear to explain the observed arcs.

Since the NIE model suggested an almost spherical lens. We modelled the lens using a NIS model with external shear. We again find the posterior variance is smaller than the prior for Einstein radius, axis ratio and external shear. Hence, these parameters are considered to be rigorously constrained. Also the posterior variance is noticeably lesser for all the lens parameters compared to the NIE model.

Posterior Results for Source Parameters

For the NIE model, the posterior variance of the source parameters suggest that the Sérsic index, effective radius and centroid of the source are rigorously constrained. But the intensity at effective radius is not well constrained. Based on the posterior

distribution obtained for the Sérsic index, we infer the source has an exponential light profile, and the position of the source is close to the center of the lens. We compute similar posterior distributions for source parameters, when we model the lens as a NIS.

Comparison between NIE and NIS model

For SL2S J0217-0513, we find the posterior variance of the lens and source parameters are smaller for the NIS model compared to the NIE model. Also the likelihood of NIS model is higher compared to the NIE model. Hence, we conclude that the lens is more likely a NIS than NIE.

For the lens, we constrained the Einstein radius ($1.67'' \pm 0.15$), axis ratio (f=1) and external shear (0.07 ± 0.02,0.02 ± 0.02). We reckon the core is most likely a flat core ($0.36'' \pm 0.11$) than a cuspy one. For the source, we constrained the position to within a pixel ($-0.20 \pm 0.08''$,$0.06 \pm 0.04''$), the effective radius is in $0.15 \pm 0.1''$ and Sérsic index is close to that of an exponential profile. We infer the properties of the extragalactic universe from these parameters in the next chapter.

Table II.4.2: Posterior distribution of lens and source parameters for the SL2S J0217-0513 using NIE and NIS lens model with external shear

Parameter	Prior (NIE)			Posterior		Prior (NIS)	Posterior	
	Uniform	μ	σ	μ'	σ'	Uniform	μ'	σ'
Einstein Radius, R_{Ein} $[arcsec]$	$[1, 2]$	1.50	0.29	1.70	0.16	$[1, 2]$	1.67	0.15
Axis ratio, f	$[0.5, 0.99]$	0.75	0.14	0.91	0.08	1		
Core radius, b_c	$[0, 0.5]$	0.26	0.14	0.35	0.12	$[0, 0.5]$	0.36	0.11
Position angle, $\theta_{LENS}[rad]$	$[0, \pi/2]$	0.78	0.45	0.64	0.48	0		
External shear, γ_1	$[-0.1, 0.1]$	0	0.06	0.07	0.03	$[-0.1, 0.1]$	0.07	0.02
External shear, γ_2	$[-0.1, 0.1]$	0	0.06	0.03	0.03	$[-0.1, 0.1]$	0.02	0.02
Sérsic Index, n				1.41	0.28		1.44	0.21
Effective Radius, $R_{eff}[arcsec]$				0.15	0.10		0.15	0.07
centroid, y_1				-0.20	0.08		-0.21	0.04
centroid, y_2				0.06	0.04		0.09	0.03
Intensity, I_e				6.73	5.41		6.11	3.22
Likelihood				0.0023	0.0029		0.01	0.01

The horizontal line in the middle of the table separates the lens parameters (top) from the source parameters (bottom).

II.4.3.2 Posterior distribution for lens and source parameters of SLACS lenses Set–1

In this section, we present the results for the SLACS lenses that gave acceptable results for the lens and source parameters. In table II.4.3 we present the posterior distribution for the lens and source parameters for 5 SLACS lenses - J0737+3216, J0959+0410, J1205+4910, J1420+6019 and J1627-0053. The lenses are modelled as nonsingular isothermal ellipsoids (NIE) with external shear. In table II.4.4 we present the posterior distribution for the lens and source parameters of the same lenses when modelled as a nonsingular isothermal sphere (NIS) with external shear.

Posterior distribution of the lens parameters for the NIE model

The Einstein radius is rigorously constrained for J0737+3216 (1.44±0.14″), J0959+0410 (1.23±0.20″), J1205+4910 (1.24±0.15″) and J1627–0053 (1.24±0.15″). For J1420+6019 (1.33±0.23″) the Einstein radius is only weakly constrained, because the number of pixels available for inversion is low (∼50). Consult section II.3.4.2 for the effect of the number of pixels on the posterior distribution.

The axis ratio is rigorously constrained for all the lenses. The posterior distributions do not suggest circular lenses but the mean value is in the order of 0.88 for all the lenses.

The core radius is not rigorously constrained for all the lenses. The correlation coefficient between the Einstein radius and core radius is in the order of 0.97 for all the lenses. Nevertheless the shift in the mean of the posterior distribution compared to the prior suggest that J0737+3216 (0.39±0.09″) and J1627-0053 (0.32±0.10″) have a flat core and J1205+4910 (0.14±0.10″) has a cuspy core. The nature of J0959+0410 (0.19±0.12″) and J1420+6019's (0.26±0.15″) core cannot be determined.

Since the axis ratio of all lenses are in the order of 0.9, it will be difficult to constrain the position angle. The posterior distribution is not distinguishable from the prior distribution of the position angle for any of the lens.

The shear is well constrained for 3 of the lenses. The lens J0737+3216 (0.06±0.03, 0.04±0.02) prefers a non negligible amount of external shear. While, J1205+4910 (-

0.02±0.04, 0.04±0.03) and J1627–0053 (-0.01±0.02, 0.02±0.02) require only a small amount of shear which can be omitted if the shear, axis ratio, position angle correlation is lifted. For the lens J0959+0410 (0.01±0.05, 0.02±0.04) and SLACS J1420+6019 (0.02±0.05, 0.03±0.05) the shear is not rigorously constrained because the posterior distribution cannot be distinguished from the prior.

Posterior distribution of the source parameters for the NIE model

The posterior variance of the centroid of the source is reasonably small for all the lenses. The position of the source is constrained within a couple of pixels for all the lenses. The source is not very far from the center of the lens for any of the cases.

The effective radius is well constrained for all the lenses. The value is in the order of 0.15″. The effective radius of J1627–0053 is strongly constrained because the posterior variance is 0.02 for this case.

The Sérsic index is well constrained for all the lenses. But the posterior distribution cannot be taken at face value because we know from our study of simulated arcs (cf. section II.3.3.3) that the Sérsic index is not rigorously estimated by our method. Nevertheless, the mean of the posterior distribution robustly suggests that the sources are more likely to follow an exponential profile.

The intensity at effective radius is reasonably constrained for 3 of the lenses viz. J1205+4910. J1420+6019 and J1627–0053. The value is not constrained for J0959+0410 and J0737+3216 because the posterior variance is too large to infer a meaningful value.

Table II.4.3: Posterior distribution of lens and source parameters for SLACS lenses set – 1 using NIE lens model with external shear

Parameter	Prior Distribution			Posterior Distribution									
				J0737+3216		J0959+0410		J1205+4910		J1420+6019		J1627-0053	
	Uniform	μ	σ	μ'	σ'	μ'	σ'	μ'	σ'	μ'	σ'	μ'	σ'
R_{Ein}	$[1, 2]$	1.50	0.29	1.44	0.14	1.23	0.20	1.24	0.15	1.33	0.23	1.58	0.14
f	$[0.5, 1]$	0.75	0.14	0.88	0.06	0.84	0.10	0.88	0.08	0.85	0.09	0.92	0.05
b_c	$[0, 0.5]$	0.26	0.14	0.39	0.09	0.19	0.12	0.14	0.10	0.26	0.15	0.32	0.10
θ_{LENS}	$[0, \pi/2]$	0.78	0.45	1.16	0.45	0.77	0.43	0.65	0.42	0.71	0.39	1.06	0.48
γ_1	$[-0.1, 0.1]$	0	0.06	0.06	0.03	0.01	0.05	-0.02	0.04	0.02	0.05	-0.01	0.02
γ_2	$[-0.1, 0.1]$	0	0.06	0.04	0.02	0.02	0.04	0.04	0.03	0.03	0.05	0.02	0.02
Sérsic Index, n				1.27	0.28	1.04	0.19	1.14	0.13	1.36	0.22	0.90	0.07
Effective Radius, R_{eff}				0.13	0.09	0.20	0.12	0.19	0.08	0.17	0.11	0.13	0.02
centroid, y_1				0.00	0.01	0.28	0.07	0.29	0.07	-0.03	0.04	-0.03	0.02
centroid, y_2				0.07	0.07	0.19	0.08	-0.07	0.03	0.11	0.06	-0.18	0.02
Intensity, I_e				7.72	4.16	7.75	4.45	6.58	2.00	2.97	2.14	4.84	1.32
Likelihood				1.5e-4	2.6e-4	0.16	0.10	0.09	0.08	0.01	0.02	6.1e-4	5.6e-4

The horizontal line in the middle of the table separates the lens parameters (top) from the source parameters (bottom).

Table II.4.4: Posterior distribution of lens and source parameters for SLACS lenses set – 1 using NIS lens model with external shear

Parameter	Prior Distribution			Posterior Distribution									
				J0737+3216		J0959+0410		J1205+4910		J1420+6019		J1627-0053	
	Uniform	μ	σ	μ'	σ'	μ'	σ'	μ'	σ'	μ'	σ'	μ'	σ'
R_{Ein}	$[1, 2]$	1.50	0.29	1.35	0.21	1.28	0.22	1.23	0.13	1.28	0.20	1.59	0.12
b_c	$[0, 0.5]$	0.26	0.14	0.35	0.14	0.26	0.14	0.14	0.09	0.26	0.14	0.35	0.09
γ_1	$[-0.1, 0.1]$	0	0.06	0.05	0.06	0	0.04	-0.03	0.02	0.01	0.03	0.01	0.01
γ_2	$[-0.1, 0.1]$	0	0.06	0.01	0.02	0	0.04	0.01	0.02	-0.01	0.03	0	0.01
Sérsic Index, n				1.58	0.13	1.09	0.22	1.13	0.12	1.43	0.15	0.88	0.09
Effective Radius, R_{eff}				0.24	0.17	0.22	0.10	0.19	0.08	0.22	0.12	0.12	0.02
centroid, y_1				-0.01	0.02	0.29	0.08	0.30	0.06	-0.04	0.03	-0.03	0.02
centroid, y_2				0.13	0.11	0.18	0.09	-0.08	0.03	0.14	0.06	-0.16	0.02
Intensity, I_e				3.25	1.08	6.90	5.05	6.63	1.76	2.45	0.99	4.59	1.22
Likelihood				1.5e-5	2.2e-5	0.30	0.19	0.08	0.06	0.01	0.01	4e-4	4e-4

The horizontal line in the middle of the table separates the lens parameters (top) from the source parameters (bottom).

Comparison between the NIE and NIS model

We do not discuss in detail how rigorously each parameter is constrained by the NIS model. Instead we provide our reasons for choosing NIE or NIS model for each lens in Set–1.

In case of J0737+3216, the posterior variance of the lens parameters and source parameters are smaller for the NIE model compared to the NIS model. Also, the likelihood of the NIE model (1.5e-4±2.6e-4) is larger than the likelihood of the NIS model (1.5e-5±2.2e-5). Hence, we opt the **NIE** model for **J0737+3216**.

For J0959+0410, the posterior distribution of all the lens and source parameters are similar for both the NIE and NIS model. The likelihood of the NIS model (0.3±0.19) is higher than that of the NIE model (0.16±0.10) so we choose the **NIS** model for **J0959+0410**.

In the case of J1205+4910, we find that the posterior distribution of all the lens and source parameters are similar for both the NIE and NIS model. Also, the likelihood of both the models are in the same order. There is no strong reason to chose one model over the other, so we stick to the **NIE** model for **J1205+4910** because the luminous part of the lensing galaxy has an elliptic shape.

For J1420+6019, we find that the posterior distribution of all the lens and source parameters are similar for both the NIE and NIS model. The external shear is more rigorously constrained by the NIS model, where the degeneracy between axis ratio, position angle and shear is lifted. Hence, we choose the **NIS** model for **J1420+6019**.

For J1627-0053, the posterior distribution of all the lens and source parameters are similar for both the NIE and NIS model. The likelihood is slightly larger for the NIE model but since the observed image is shaped like a ring, we prefer the **NIS** model for **J1627-0053**.

II.4.3.3 Posterior distribution for lens and source parameters of SLACS lenses Set–2

In this section, we present the results of the lenses for which we obtained unfeasible results. In table II.4.4 we present the posterior distribution for the lens and source

parameters for 3 SLACS lenses - J0956+5100, J2302+1422 and J2321-0939. The lenses are modelled as a nonsingular isothermal ellipsoid (NIE) with external shear. We do not discuss each parameter in detail for these lenses. Instead we present the reasons for rejecting the posterior distribution we obtained for each of these lenses.

For J0956+5100, the posterior distribution is not distinguishable from the prior for any of the lens parameters. This could imply that the parametric model we chose for the lens or source or both were not the right choice to model this lens. Therefore, we rejected the parameters we computed for this lens.

For J2302+1422, the Einstein radius, axis ratio and core radius are constrained in the posterior distribution. For the remaining lens parameters, the posterior distribution is not distinguishable from the prior. All source parameters are also strongly constrained by the method. The reason we had to reject the model is because the effective radius of the source ($1.85\pm0.15''$) is larger than the Einstein radius of the lens. This configuration should give rise to unusually large bright arcs in the observed image. Since, we do not find any such arcs, we rejected the parameters we computed for this lens. One of the reasons for computing such unfeasibly high effective radius is because, the counter images observed converge to two different regions in the source plane. When a Sérsic fit is made in that case, one would compute similar effective radii.

For J2321-0939, the posterior variance is smaller than the prior variance for Einstein radius and axis ratio. For the remaining lens parameters the posterior distribution cannot be distinguished from the prior. The posterior distributions of all the source parameters have a small variance. But similar to J2302+1422, we find the effective radius of the source ($1.51\pm0.19''$) to be larger than the Einstein radius of the lens. Hence, we reject the computed posterior distributions for this lens.

Table II.4.5: Posterior distribution of lens and source parameters for SLACS lenses set – 2 using NIE lens model with external shear

Parameter	Prior Distribution			Posterior Distribution					
				J0956+5100		J2302+1422		J2321–0939	
	Uniform	μ	σ	μ'	σ'	μ'	σ'	μ'	σ'
R_{Ein}	$[1, 2]$	1.50	0.29	1.27	0.34	1.06	0.05	1.36	0.13
f	$[0.5, 1]$	0.75	0.14	0.70	0.12	0.79	0.12	0.9	0.07
b_c	$[0, 0.5]$	0.26	0.14	0.38	0.14	0.46	0.03	0.40	0.09
θ_{LENS}	$[0, \pi/2]$	0.78	0.45	0.60	0.46	0.67	0.40	0.88	0.45
γ_1	$[-0.1, 0.1]$	0	0.06	0.02	0.05	-0.03	0.05	0.03	0.05
γ_2	$[-0.1, 0.1]$	0	0.06	0.02	0.06	0.02	0.05	0.03	0.04
Sérsic Index, n				1.74	0.62	1.44	0.04	1.31	0.05
Effective Radius, R_{eff}				1.12	0.36	1.85	0.15	1.51	0.19
centroid, y_1				-0.67	0.34	-0.71	0.09	0.06	0.07
centroid, y_2				0.10	0.09	-0.97	0.09	0.85	0.1
Intensity, I_e				4.88	3.17	11.95	1.44	14.62	2.77
Likelihood				0.03	0.03	2.9e-6	1.8e-6	1.3e-8	1.3e-8

II.4.4 Summary

In this chapter we inverted 9 observed gravitational arcs and obtained a posterior distribution of the lens and source parameters. We find that our method yields rigorous constraints for 6 of the lenses. The posterior distribution of remaining 3 lenses were not accepted on grounds of the reasons given in II.4.3.3. For the lens parameters, we find that our method can constrain the Einstein radius, axis ratio and shear rigorously. But the core radius and position angle were only weakly constrained. We constrained the position of the source, Sérsic index and effective radii rigorously. In the next chapter we use the lens parameters obtained in here to answer some open questions related to the extragalactic universe.

Chapter II.5

Discussions and Conclusion

In previous chapter we obtained the lens and source parameters for six observed gravitational lenses. In this chapter we use these parameters to probe the cosmology in galaxy scale dark matter halos and high–redshift sources. We discuss the lens and source parameters separately and we compare our results with the results obtained by previous works for the same lenses.

II.5.1 Physical Properties of the Lenses

In this section we compute the physical properties of the lens viz. size of the lens, dispersion velocity, total mas within the Einstein radius, total mass within the core radius, stellar mass within the Einstein radius and fraction of dark matter within the Einstein radius. The results compiled from previous works are given in table II.5.1 (Tu et al., 2009; Koopmans et al., 2006; Auger et al., 2009, 2010), and the results obtained using our method are given in table II.5.2.

Physical size of the lens

We compute the Einstein radius in units of kilo-parsecs to infer the size of the lenses relative to one and another. In the top left panel of figure II.5.1 we show the values obtained by our method and previous works. The results are also given in column

2 of the tables II.5.1 and II.5.2. We compute a noticeably larger Einstein radius compared to Tu et al. (2009) for the SL2S lens and Koopmans et al. (2006) for the SLACS lens. The results obtained by us are within the 1σ deviation of the distance between the centre of the lens and the position of the arcs.

Dispersion velocity

We compute the dispersion velocity from the Einstein radius using the equation II.1.17. The results are shown in the top right panel of figure II.5.1 and also given in column 3 of the tables II.5.1 and II.5.2. We find that the dispersion velocity measured by our method is higher than that measured by Koopmans et al. (2006) for the SLACS lenses. But the values we computed are within the 2σ deviation of the measured stellar dispersion velocities given in table II.5.1.

Total Mass within the Einstein radii

Using the lens parameters computed in the previous chapter we determine the mass within the Einstein radius using the equation given below. The mass within the Einstein radius M(R_{ein}) is the product of surface mass density $\Sigma(r)$ (cf. equation II.1.15) and the projected surface area.

$$M(R_{Ein}) = \Sigma(D_d R_{Ein})\, \pi (D_d R_{Ein})^2 \quad [M_\odot] \tag{II.5.1}$$

We compute the $M(R_{Ein})$ for all the lens parameters of the posterior distribution and give the mean and 1σ deviation in column 4 of table II.5.2. Results from Koopmans et al. (2006) are given in column 5 of table II.5.1 for comparision. On average we compute lesser mass than Koopmans et al. (2006) for the SLACS lenses.

Table II.5.1: Physical properties of the lenses compiled from literature

Lens Name	R_{Ein}[kpc]	r_{eff}[kpc]	σ_v $[km\,s^{-1}]$	M(R_{Ein})$[10^{11}M_\odot]$	$M_*[10^{11}M_\odot]$	$f_{DM}(r_{eff})$
SL2S J0217–0513	13.61	na	na	na	$3.4^{+0.5}_{-0.7}$	$0.41^{+0.09}_{-0.06}$
SLACS J0737+3216	4.66	14.10	297	3.12	2.15±0.36	0.49±0.09
SLACS J0959+0410	2.24	3.34	216	0.76	0.34±0.05	0.54±0.08
SLACS J1205+4910	4.27	9.04	na	2.5	1.08±0.15	0.63±0.06
SLACS J1420+6019	1.27	2.56	204	0.39	0.58±0.08	0.30±0.10
SLACS J1627–0053	4.18	6.87	271	2.22	1.29±0.25	0.54±0.10

Column 1 presents the Einstein radius for the lenses in units of kilo parsecs (Auger et al., 2009). Column 2 presents the effective radius corrected to rest frame V–band (Auger et al., 2010). Column 3 presents the best fit value for the dispersion velocity (Koopmans et al., 2006). Column 4 presents the mass within the Einstein radii (Koopmans et al., 2006). Column 5 presents the stellar mass within the Einstein radii (Auger et al., 2009). Column 6 presents the stellar mass within the Einstein radii for a Chabrier IMF (Auger et al., 2009). Column 7 presents the fraction of dark matter within the effective radii (Auger et al., 2010). For SL2S the given values are taken from Tu et al. (2009).

Table II.5.2: Physical properties of the lenses compiled from our results

Lens Name	R_{Ein}[kpc]	σ_v $[km\,s^{-1}]$	M(R_{Ein})$[10^{11}M_\odot]$	$M_{core}[10^{11}M_\odot]$	$f_{DM}(R_{Ein})$
SL2S J0217–0513	16.23±1.46	275±12	4.42±0.73	0.22±0.11	0.23±0.11
SLACS J0737+3216	7.90±0.77	320±16	2.69±0.47	0.20±0.07	0.20±0.12
SLACS J0959+0410	3.06±0.53	263±21	1.23±0.44	0.06±0.05	0.72±0.07
SLACS J1205+4910	4.80±0.58	270±15	1.19±0.28	0.02±0.03	0.09±0.17
SLACS J1420+6019	1.60±0.25	222±17	0.29±0.08	0.01±0.01	-1.02±0.44
SLACS J1627–0053	5.97±0.45	294±11	1.86±0.27	0.10±0.04	0.30±0.09

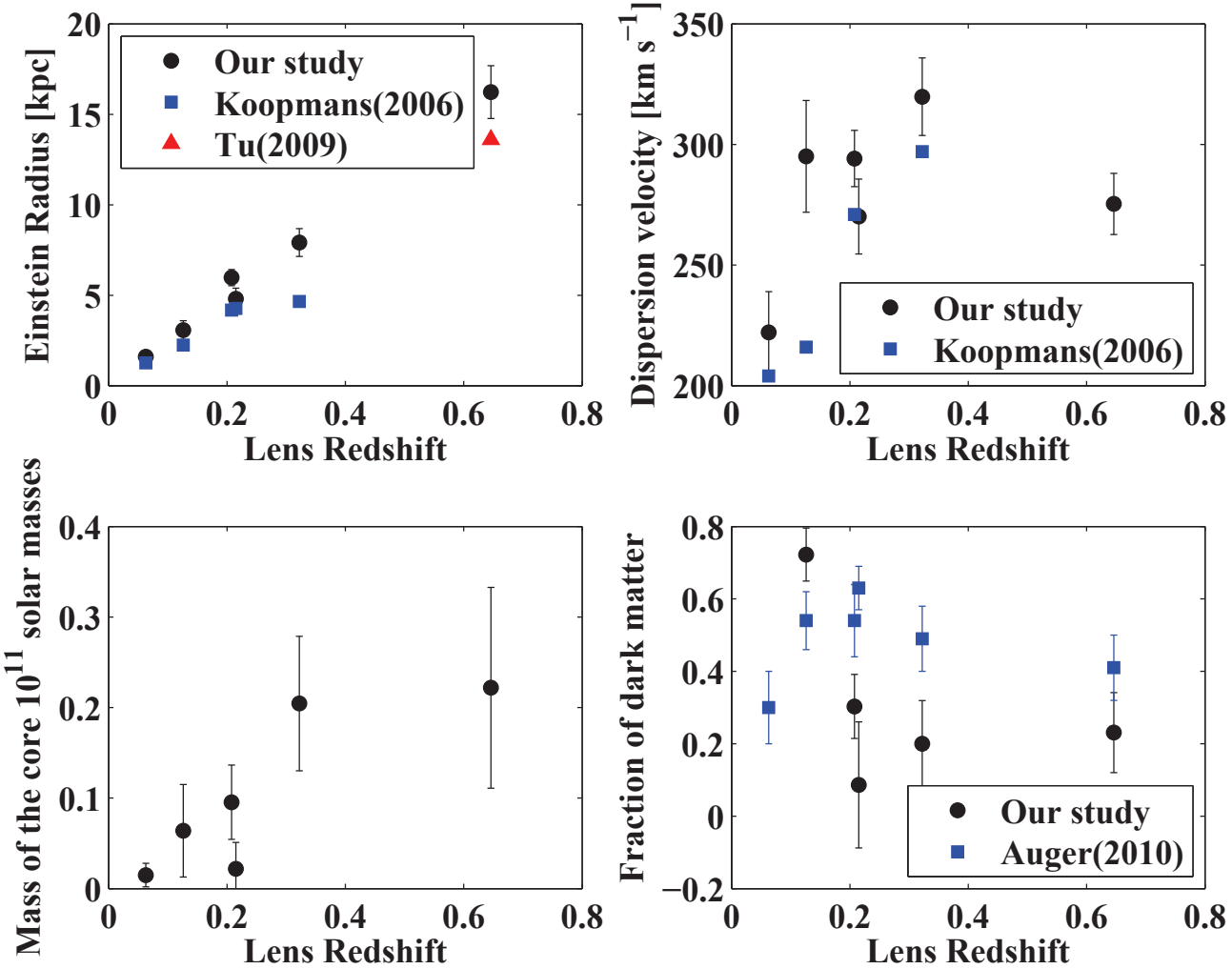

Figure II.5.1: **Properties of the lenses:** The figures show the physical properties of the lenses as a function of the lens redshift. The top left panel shows the Einstein radius in kpc as a function of redshift. We also present the values computed by Koopmans et al. (2006) and Tu et al. (2009) for comparison. The top right panel shows the dispersion velocity as a function of redshift. The bottom left panel shows the mass of the lens core as a function of redshift. The bottom right panel shows the fraction of dark matter within the Einstein radius as a function of redshift.

Mass of the lens core

We compute the mass of the lens core M(b_c) using equation II.5.1. In the bottom left panel of figure II.5.1 we show the mass of the lens core as a function of the redshift. The same values are tabulated in column 5 of table II.5.2. This mass of the lens core was not computed in earlier works so we cannot provide a comparison against any. For all the lenses studied in this work, we find that around 5% of the lens mass is present in the core. Except for J1420+6019 the core mass of all other lenses are only weakly constrained.

Stellar Mass within the Einstein radii

In column 5 of table II.5.1 we present the stellar mass within the Einstein radii given by Tu et al. (2009) for the SL2S lens and Auger et al. (2009) for the SLACS lenses. We use their values to compute the fraction of dark matter in the lens. Auger et al. (2009) used Chabrier and Salpeter IMF to find the total stellar mass in the lenses. They also give the fraction of the stellar mass within the Einstein radii. The value of the Einstein radii computed by Auger et al. (2010) is always lesser than the value computed by us (cf. column 2 of tables II.5.1 and II.5.2). Therefore, we do not know the exact amount of stellar mass within the Einstein radii we computed. The task of computing the stellar mass is a nontrivial task so we use the stellar mass value given by Auger et al. (2010) as lower estimate in our calculation. Hence the fraction of dark matter we compute in the next section is an upper limit on the same.

Fraction of dark matter within the Einstein radii

The total mass of dark matter within the Einstein radii is the difference between the total mass within the Einstein radii and the stellar mass within the Einstein radii. We use the total mass computed by our method (cf. column 3 table II.5.2) and stellar mass described in the section above for computing the fraction of dark matter. In bottom left panel of figure II.5.1 we show the fraction of dark matter (f_{DM}) present in the lenses as a function of redshift.

In column 6 of table II.5.2 we give the values for the fraction of dark matter within the Einstein radii. For comparison we also give the value of f_{DM} within the effective radii computed by Auger et al. (2010) in column 7 of table II.5.1. We remind the reader that the effective radius is a few times larger than the Einstein radius (cf. columns 2 & 3 of table II.5.1) for all the lenses. We also present the results as function of lens redshift in the bottom right panel of figure II.5.1.

For SLACS J0959+0410 we measure a large fraction of dark matter within the Einstein radius (0.72±0.07). This is because we do not know the accurate amount of stellar mass within the Einstein radius we computed. For SLACS J1420+6019 the total mass we measure is lesser than the stellar mass given by Auger et al. (2009). Other parametric models can be applied for the lens to resolve this discrepancy. For the remaining lenses the average value we compute for the fraction of dark matter is 0.2±0.1. This value is in agreement with the average projected dark matter fraction given by Koopmans et al. (2006) for the SLACS lenses, 0.25±0.06.

II.5.2 Properties of the Sources

The light profile of the background sources in these lenses has not been studied before. In this section we present some of the interesting results we obtained about the background sources. The redshift of the SL2S source is 1.847 and the average redshift of the SLACS sources is 0.53.

We recall that we reconstructed the sources with a Sérsic profile. The two interesting results we learned from the background sources are as follows. We learned that the reconstructed background sources have an exponential profile, i.e. the Sérsic index $n \sim 1$.

We computed the effective radius of the sources. The values are tabulated in table II.5.3. We find that the size of the SLACS sources are in the order of 1.45±0.39 kpc. The SL2S source at redshift 1.847 has a radius of 3.54±1.65 kpc. In figure II.5.2 we show the effective radius as a function of redshift. We also show the effective radius of the galaxies in the same redshift range for comparison (cf. Scarlata et al., 2007, COSMOS). We find that the sources reconstructed in the study have

Table II.5.3: Properties of the Sources

Lens Name	R_{eff}''	R_{eff}[kpc]
SL2S J0217–0513	0.15±0.07	3.54±1.65
SLACS J0737+3216	0.13±0.09	1.16±0.80
SLACS J0959+0410	0.22±0.10	1.84±0.83
SLACS J1205+4910	0.19±0.08	1.45±0.61
SLACS J1420+6019	0.22±0.12	1.84±1.00
SLACS J1627–0053	0.12±0.02	0.98±0.16

R_{eff} is the effective radius of the source.

similar effective radius compared to the sources at the same redshift in the COSMOS (survey). We note that the effective radius of the reconstructed sources in our study are systematically smaller than the average value of the same in COSMOS. The number of data points in our study are not sufficient enough to conclude whether this is a systematic effect of our method.

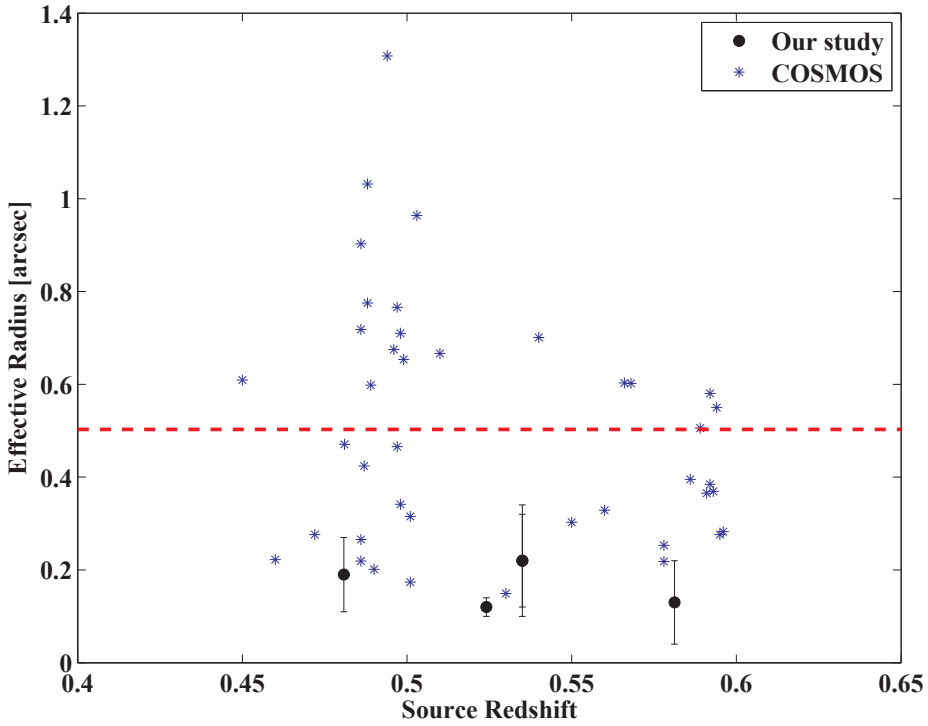

Figure II.5.2: **Properties of the Sources:** This figure shows the effective radius of the reconstructed sources as a function of their redshift. We also present the effective radius of the sources from the `Zurich Structure & Morphology Catalog v1.0` (cf. Scarlata et al., 2007, COSMOS) for comparison. The red–dashed line is the mean of the effective radius for the galaxies in the catalog. The data points for the COSMOS are taken from the field 150.2<RA<150.3 and 2.2<DEC<2.3.

II.5.3 Future Work

To begin with we tested our method only on a small set of lenses in the SL2S and SLACS database. We would like to apply our method to other lenses with high S/N arcs to obtain a better understanding of the lensing galaxies and the distribution of dark matter in them.

In this work we used only one parametric model for the lens namely the nonsingular isothermal ellipsoid. Since this model could not satisfactorily explain some of the lenses we studied, we would like to add more models for the lens (e.g. power law model) and repeat the MCMC analysis to obtain new constraints on the lens and source properties. This direction of study will allow us to find the most likely model for the lens mass profile. In the source reconstruction method developed in our work, we always approximate the reconstructed source to a circle with Sérsic profile. We would like to explore the possibility to reconstructing sources with 2–D profile.

We reckon that future missions like *Euclid* will discover thousands of new strong gravitational arcs and the methods developed in this thesis will be useful to compute the lens and source parameters of these arcs. The increase in number of gravitational lenses will allow us to answer questions related to the nature of evolution of galaxies and dark matter halos. MCMC routines are time consuming in general and to apply them for a large number of arcs we need to optimise our routines to perform the desired calculations using least possible time.

II.5.4 Conclusion

In this work we improved the existing method used to solve the inverse problem in lens modelling. We parametrically model both the lens and the source in conjunction using Bayesian inference. We tested our method on simulated gravitational arcs and were able to recover the lens and source parameters rigorously. We also applied our method on real gravitational lenses in the SL2S and SLACS database and computed the lens and source parameters for these lenses. The computed parameters allow us to study the extragalactic universe in new light. The significant results of our study

are as follows.

We find that isothermal models are sufficient to describe most of the observed lenses. We were able to model six out of the nine lenses we studied using either a nonsingular isothermal ellipsoid (NIE) or nonsingular isothermal sphere (NIS) model for the lens. We find that some models require a non negligible amount of external shear to explain the observed images. We also find that Sérsic light profile is sufficient to describe to most of the background sources in the observed lenses.

Using the computed lens parameters we obtained the physical size of the lens, the dispersion velocity, total mass within the Einstein radius, mass of the lens core and the fraction of dark matter within the Einstein radius. For all the lenses studied in this work around 20±5% of the lens mass is found to be in the core. We find the fraction of dark matter within the Einstein radius to be 0.2±0.08. The high redshift background sources we studied show an exponential light profile.

Part III

Obstructed Telescopes Versus Unobstructed Telescopes for Wide Field Surveys – A Quantitative Analysis

Chapter III.1

Three Mirror Anastigmat Telescopes

We stated in section I.2.3 that our aim is to quantify with what precision telescopes having unobstructed pupils can deliver measurements of weak lensing observables. We compare the precision with which unobstructed telescopes and obstructed telescopes measure the axis ratio and position angle of galaxies. In order to quantify the precision of both the telescopes, we design and optimise an obstructed and an unobstructed telescope with same characteristics. Before we present our methods and results, we would like to remind the reader about some basic facts regarding telescopes.

We begin this chapter with a short introduction to telescopes in general and *Three Mirror Anastigmat* (TMA) telescopes in particular. Next, we recall the difference between obstructed and unobstructed TMA telescopes. Then, we put forth the arguments that favour an unobstructed TMA for weak lensing surveys. Finally, we list the main objectives which we will test to quantify the difference in the precision measurements of weak lensing observables between obstructed and unobstructed TMA telescopes.

III.1.1 A Brief Introduction to Telescopes

Telescopes are instruments that gather and focus electromagnetic radiation from distant astronomical objects. The intensity, wavelength, polarization state and other properties of the gathered electromagnetic radiation help us to study these astronomical objects in great detail. Telescopes are mainly classified depending upon the wavelength (radio, submillimeter, infrared, visible, ultraviolet, x-ray, γ-ray, etc.) they observe. Telescopes observing in radio wavelength have very little in common with telescopes observing in γ-ray. In this study we restrict ourselves to telescopes observing in visible band of the electromagnetic spectrum. These are called optical telescopes and they are either space–based or ground–based. Hereafter we use the word *'telescope'* to refer to space–based optical telescopes. The final conclusion of our study can also be extended to telescopes observing in infrared band of the electromagnetic spectrum, because the design characteristics of infrared and optical telescopes are similar.

Modern space–based optical telescopes are reflecting telescopes which use a combination of curved mirrors to reflect light and form an image. Nowadays, telescopes designs based on three aspheric mirrors also called *Three Mirror Anastigmat* (hereafter TMA) are favoured for wide field surveys e.g *Euclid*. The TMA configuration minimizes three main optical aberrations (spherical aberration, coma and astigmatism) and provides the widest possible diffraction limited field–of–view for a given pupil size. Depending on the position of the secondary mirror with respect to the primary mirror, TMA telescopes are classified into obstructed TMA and unobstructed TMA. We distinguish between these two types in the next section.

III.1.2 Obstructed and Unobstructed TMA Telescopes

Obstructed TMA – OTMA

Conventionally, the primary reflecting surface of TMA telescopes focuses light to a common point in front of its own reflecting surface. A secondary reflecting surface is placed before or after the focal point of the primary mirror. This arrangement partially obstructs the light travelling to the primary surface. Hence, we call these type of telescopes *Obstructed TMA* telescopes (hereafter OTMA telescopes). The OTMA design was proposed by Paul (1935) and developed by Baker (1969) and Korsch (1972). The obstruction caused by the secondary mirror and its supporting structure reduces the light gathering area of OTMA telescopes and produces diffraction spikes on the focused image. Regardless of these limitations a vast majority of space–based telescopes are OTMA type because of their low-cost and compact design e.g. *Hubble Space Telescope*, *Herschel space observatory* and etc.

Unobstructed TMA – UTMA

Telescopes in which the secondary mirror is offset from the path of the incoming light are generally called *Unobstructed TMA* telescopes (hereafter UTMA telescopes). The design of UTMA telescopes was first discussed by Cook (1979) and Korsch (1980), but a practical design was only built in the recent years. GAIA (Perryman, 2005) is a UTMA telescope designed by ESA for stellar spectrophotometry. Serabyn et al. (2010) have shown that unobstructed ground based telescopes can image exoplanets close to bright stars with high contrast compared to obstructed telescopes. Hence, UTMA designs have been proposed for exoplanet characterization missions like EChO (Tinetti et al., 2012) and SPICES (Boccaletti et al., 2012).

III.1.3 Arguments in Favour of UTMA Design

In this section we present theoretical arguments that favour a UTMA design in general. The main advantages of a UTMA telescope are increased light gathering area and cleaner PSF. We elaborate on these arguments below.

III.1.3.1 Light Gathering Power

The light gathering power of a telescope depends on the amount of area available for collecting light. For a given pupil size, the effective light gathering area of an obstructed pupil is lesser than that of an unobstructed pupil. The limiting flux observable for a given pupil is directly proportional to the light gathering area. Hence, more light gathering area implies faint astronomical sources can be observed using an unobstructed pupil for a given exposure time. For a circular pupil, the ratio of the radius of the primary mirror to the radius of the central obstruction is called obscuration ratio (ϵ). And the fractional decrease in light gathering area of an OTMA telescopes is given by ϵ^2. For reasonable obscuration ratio like 0.2, OTMA telescopes have 4% less area than a UTMA telescopes. The obscuration ratio is 0.125 (0.3/2.4) for *Hubble Space Telescope* and 0.1 (0.35/3.5) for *Herschel space observatory*. Even though UTMA telescopes have increased light gathering area than OTMA, it is not a severe draw back for OTMA telescopes.

III.1.3.2 PSF and Encircled Energy

The main disadvantage of OTMA telescopes is the blur size introduced in the image plane. The focal image of a point source at infinity is the Fourier transform of the pupil shape. This image is called the *point spread function* (hereafter PSF). For a circular pupil, the shape of the PSF is the Airy pattern with a bright central disc and faint concentric rings. We know from the studies of Taylor and Thompson (1958) that in the Airy pattern of an annular aperture there is significant transfer of energy from the central disc to the outer rings.

Encircled Energy (hereafter EE) is the fraction of energy encircled within a radius

r from the centre of the PSF peak. Using theoretical relations from Schroeder (1987), we show how the EE of an obstructed pupil differs from an unobstructed pupil for increasing values of obscuration ratio. For a given wavelength λ, and primary mirror focal ratio F_{pri}, EE(x), where $x \approx \pi r/(\lambda F_{pri})$ is given by Equation II.1.1 (cf. Schroeder, 1987).

$$\begin{aligned} EE(x) &= \frac{1}{1-\epsilon^2}\Big[1 - J_0^2(x) - J_1^2(x) + \epsilon^2[1 - J_0^2(\epsilon x) - J_1^2(\epsilon x)] \\ &\quad -4\epsilon \int_0^x \frac{J_1(x)J_1(\epsilon x)}{x}\mathrm{d}x\Big] \end{aligned} \tag{III.1.1}$$

Where $J_n(x)$ are Bessel functions of the first kind. Figure III.1.1 shows how the EE changes for increasing values of obscuration ratio. The plots corresponds to a circular pupil $r = 0.6$ m, the operating wavelength $\lambda = 550$ nm and the obscuration ratios are $\epsilon = \{0, 0.2, 0.5\}$. Figure III.1.1 shows the EE plot of the central field–of–view. The airy disk radius is 13.69 μm for the chosen configuration. For $\epsilon = 0.2$ at least 10% of the energy is transferred from the Airy disk to the first bright ring. For $\epsilon = 0.5$ almost half the energy lies outside the Airy radius. Our objective is to study how this transfer of energy affects the weak lensing observables.

III.1.3.3 Diffraction due to Spider Support Structure

OTMA designs require mechanical support to hold the secondary mirror in front of the primary. Usually there are four vanes at right angles holding the secondary mirror in position, these vanes are collectively referred to as the spider support structure. This arrangement of the vanes gives rise to four diffraction spikes in the PSF of OTMA design which are absent in UTMA. Hence, the PSF of UTMA telescopes are cleaner than OTMA telescopes. Consult figure III.2.5 for an example image of OTMA and UTMA PSF. One of our objective is to test whether the absence of these diffraction spikes improve the precision measurement of weak lensing observables in a UTMA design.

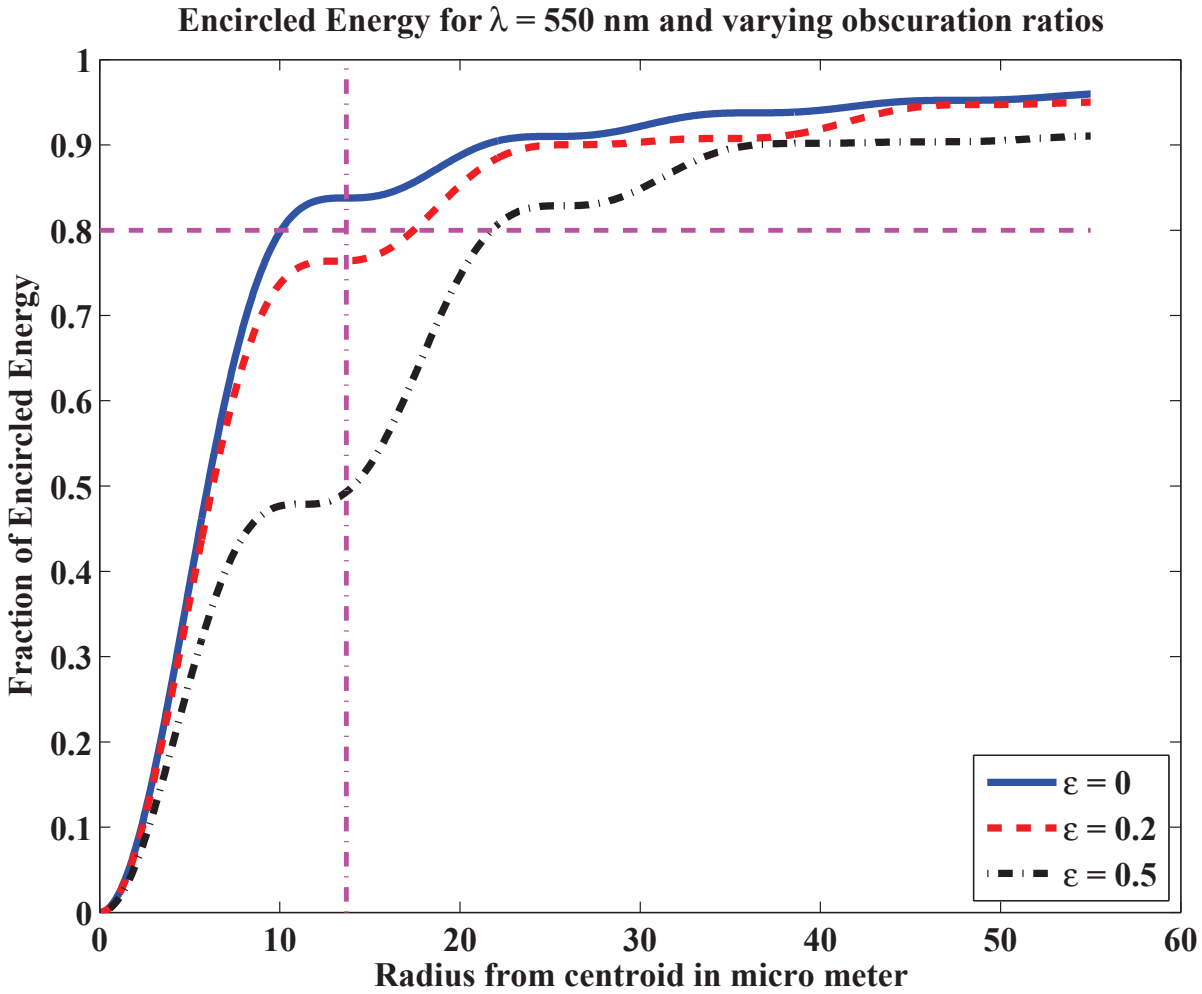

Figure III.1.1: **Encircled energy for various central obscuration ratios:**. The plot shows the encircled energy for a pupil having obscuration ratio $\epsilon = 0$ (unobstructed; blue-solid), 0.2 (red-dashed) and 0.5 (black-dotted). The operating wavelength of the setup is $\lambda = 550$ nm. The vertical line at 13.69 μm is the radius of the Airy disk. For increasing values of obscuration ratio ϵ , more energy is transferred from the central disk to the outer rings. Also the radius within which 80% of the energy is concentrated increases with the obstruction size.

III.1.4 Brief Account on Previous UTMA Designs

Based on the arguments stated above and other additional ones, Lampton et al. (2010) and Levi et al. (2011) proposed an unobstructed telescope for the *WFIRST* (Wide-Field Infrared Survey Telescope) space mission to study dark energy and exoplanets.

Lampton et al. (2010) showed that the diffraction pattern of an OTMA telescope can destroy or mimic the lensing signals we desire to study because of the larger blur size. Hence, the tighter PSF of UTMA telescopes should be beneficial for wide-field lensing missions.

Levi et al. (2011) define a quantity called survey rate, which is directly proportional to the light gathering area and inversely proportional to the blur size for a given S/N. Comparing a 1.4m OTMA with obscuration ratio 0.5 against a 1.1m UTMA design they argue that unobstructed telescopes have faster survey speed for a given S/N. They also demonstrate that for unobstructed telescopes there is an increased density of resolved galaxies for weak lensing analysis.

Since we find their OTMA obscuration large, in our work we compare a 1.2m OTMA with obscuration ratio 0.2 against a 1.2m UTMA. In spite of all the arguments in favour of UTMA design, there are certain challenges that exist today in adopting UTMA designs for real space missions. We discuss these in the next section.

III.1.4.1 Challenges in Adopting UTMA Design

The mirror surfaces of UTMA are not axis-symmetrical, this poses two problems for real designs. First, it is difficult to manufacture asymmetrical mirror surfaces compared to symmetrical ones. Second, the alignment errors in UTMA designs are tighter than that of OTMA designs, because small changes in alignment could drastically affect the characteristics of UTMA designs.

Lampton et al. (2010) find that the separation between the primary mirror and secondary mirror will always be large for a UTMA design. For a given pupil size and field-of-view this separation could be twice as large for a UTMA design compared to an OTMA design. This places tight constraints on the packaging envelop of a

UTMA design for launch. We discuss this challenge in section III.2.3.2.

In the next section, we set the objectives of our work, assuming the demerits of a UTMA design are trivial in comparison to its merits.

III.1.5 Objectives of our Work

In this work we quantify the precision with which UTMA telescopes can measure weak lensing observables compared to OTMA telescopes having same characteristics. The observables we are interested in are the axis ratio and position angle of galaxies. We investigate four questions which we reckon are sufficient to conclude whether UTMA designs are more suitable for measuring weak lensing observables when compared with OTMA designs. The questions are as follows

- In the PSF, does the transfer of energy from the central disk to the outer rings affect precision measurement of weak lensing observables?
- Does the presence of diffraction spikes in the PSF affect the precision measurement of weak lensing observables?
- How does the PSF change over the field–of–view? And how does the uncertainty in the knowledge of PSF affect the precision measurement of weak lensing observables?
- How does pixel scale of the images affect the measurement of weak lensing observables for both the OTMA and UTMA designs?

III.1.6 Outline

In order to answer the above questions we had to go through the following steps. First, we modeled and optimised in parallel an OTMA and a UTMA telescope, both having the same primary mirror, effective focal length and field–of–view. Next, we created an end-to-end semi-realistic samples of elliptical galaxies passed through the

full instrumental path, PSF convolution, CCD pixelisation, and noise effects. Then, we selected and controlled the biases of the fitting routine for measuring the axis ratio and position angle of galaxies. After that, we measured the axis ratio and position angle in simulated galaxies and calculated the error introduced by the PSF on the error budget. Finally, we compared the precision with which both the designs can perform the desired science measurements. Following chapters will explain each of these steps in detail.

Chapter III.2

Telescope Design Optimisation and PSF Computation

We recall from section I.2.3.1 that the PSF of a telescope can introduce non random errors into the weak lensing observables. The PSF of a telescope among other factors depends significantly on the telescope design parameters. The objective of this chapter is to compute the PSF for optimized designs of both the OTMA and UTMA telescopes. We then use the computed PSF to simulate galaxy images similar to real sky images observed using the telescopes.

To compute the PSF we need optimised designs of both OTMA and UTMA telescopes with similar characteristics. Since these designs are not readily available, we design and optimise an OTMA and a UTMA telescope with similar characteristics. The outline of the chapter is as follows. We begin with a brief introduction to telescope design parameters. Then, we present the procedure to compute and optimise the telescope design parameters for both the OTMA and UTMA telescopes. Finally, we compute the PSF for optimised OTMA and UTMA telescopes at desired regions in the field–of–view.

III.2.1 Telescope Design Parameters

By definition, *Three Mirror Anastigmat* telescopes consist of three conic reflecting surfaces (see Figure III.2.1). The characteristics of a TMA can be defined using two families of parameters. The fundamental design parameters, which define the optical configuration from an image perspective and the constructional parameters, which define the optical configuration from an engineering perspective.

III.2.1.1 Fundamental Design Parameters

The fundamental design parameters constrain the pixel scale, resolution limit, field–of–view and etc. We use the definition and convention given by Robb (1978) for the fundamental design parameters. We recall the definition of the fundamental design parameters below.

F_3 Focal length of the three mirror system, always positive.

Y_1 Height or radius of the primary mirror.

F_{pri} Focal ratio of the primary mirror, which is Y_1/F_p where F_p is the focal length of the primary mirror.

F_2 Focal length of the two mirror system, set to be positive for Cassegrain type, and negative for Gregorian type. We choose the Cassegrain type telescopes because they are more compact than Gregorian type.

B Location of the two mirror focus with respect to the vertex of the primary mirror, positive if beyond the vertex of the primary mirror and negative if inside.

D_3 Location of the tertiary mirror with respect to the two mirror focus, positive if beyond the focus, negative if inside.

$\bar{u}_0$ Slope of the paraxial chief ray entering the system. This defines the field–of–view.

III.2.1.2 Constructional Parameters

If the fundamental design parameters defined above are fixed, the constructional parameters can be obtained using the relations given in Robb (1978). The constructional parameters allow us to model the telescope in an optical design program. We recall the definition of each constructional parameter from Robb (1978) below.

$\{\mathbf{c_1}, \mathbf{c_2}, \mathbf{c_3}\}$ the radius of curvature of the reflecting surface

$\{\mathbf{k_1}, \mathbf{k_2}, \mathbf{k_3}\}$ conic constants of the reflecting surfaces

$\{\mathbf{d_1}, \mathbf{d_2}, \mathbf{d_3}\}$ the separation between the reflecting surfaces.

$\{\mathbf{h_1}, \mathbf{h_2}, \mathbf{h_3}\}$ the decenter distances that correspond to offset of the centre of the reflecting surfaces from the axis perpendicular to the focal plane. This parameter is only applicable for UTMA designs.

The subscripts $\{_{\mathbf{1}}, _{\mathbf{2}}, _{\mathbf{3}}\}$ denote the three reflecting surfaces of the TMA. A few of the fundamental and constructional parameters are shown in Figure III.2.1.

The equation describing the surface sagitta of the reflecting surfaces is given below.

$$z = \frac{cr^2}{1 + \sqrt{1 - (1+k)c^2r^2}} + \sum_{n=1}^{N} \alpha_n r^{2n} \tag{III.2.1}$$

In the equation above, c is the radius of curvature of the reflecting surface, k is the conic constant and z is the sagitta at the radius r. The α_ns are higher order aspheric coefficients. These coefficients are used to constrain higher order aberrations. We compute the curvatures and conic constants using relations given in Robb (1978). The optimal values for the α_ns are computed using an optical design tool.

Our next task is to set the fundamental design parameters and compute the constructional parameters of both the OTMA and UTMA design. We set the fundamental design parameters using *Euclid* mission as a reference.

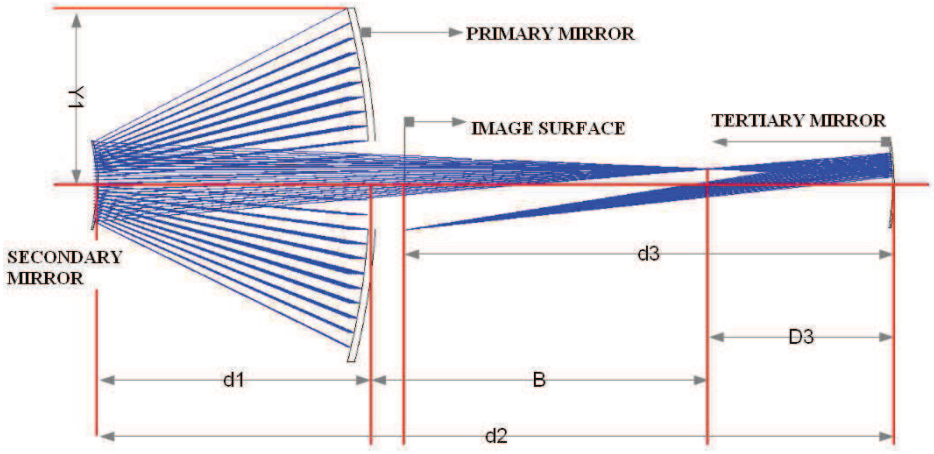

Figure III.2.1: **Nomenclature for a TMA telescope:** Figure showing the naming convention of the fundamental and constructional parameters associated with TMA telescopes in this work (convention is same as Robb (1978)).

III.2.2 Constraints for the Fundamental Design Parameters

Since we are interested in measuring weak lensing observables, we use the fundamental design parameters chosen by the *Euclid* mission as the starting point for our telescope designs. The *Euclid* mission is optimised to probe weak lensing and make a decisive statement on the nature of dark energy. The *Euclid* collaboration has carefully chosen the fundamental design parameters for their design after thoroughly considering the science and engineering constraints. In table III.2.1 we show the fundamental design parameters we set using the constraints given by Euclid Collaboration (2011).

The fundamental design parameters impose a theoretical upper limit on the image quality. The major limits are given in Table III.2.2. For the chosen range of optical wavelength (550–900 nm), effective focal length ($F_3 = 24.5$m) and radius of primary mirror ($Y_1 = 0.6$m), we find the Airy radius varies from $0.12''$ to $0.19''$. This implies

Table III.2.1: Fundamental design parameters set by Euclid Collaboration (2011)

Parameter	Value
Y_1	0.6 m
F_3	24.5 m
Field-of-view	0.787×0.709 deg^2
Wavelength, λ	550–900 nm

Table III.2.2: Theoretical limits for image quality

Parameter	Equation	Value
Image scale	$\frac{360*60*60}{2*\pi*F_3}$	8.47 arcsec/mm
Airy radius (λ =550 nm)	$1.22\frac{\lambda F_3}{2Y_1}$	13.69 μm (or 0.12″)
Airy radius (λ =900 nm)	$1.22\frac{\lambda F_3}{2Y_1}$	22.41 μm (or 0.19″)

that we cannot distinguish features which are smaller than 0.19″ in observed images. The PSF effects will not be distinguishable if the pixel size is larger than the Airy radius. Therefore, to study the impact of PSF we need to pixellate the images to some pixel size less than 0.19″. Nyquist–Shannon sampling theorem suggests that 0.19/2∼0.1″is the optimal sampling frequency. We choose 0.025″ and 0.1″ pixel scales for our simulated galaxy images in the next chapter. The former value denotes oversampling and the latter is Nyquist sampled.

III.2.3 Procedure to Obtain the Constructional Parameters

The constructional parameters can be obtained from the fundamental design parameters using the relations given in Robb (1978). We recall these relations in table III.2.3. In the previous section we have set only three $\{Y_1, F_3, \text{FoV}\}$ of the seven

Table III.2.3: Constructional parameters for TMA design expressed in terms of the fundamental parameters

Surface#	Curvature	Distance to next surface
1 Primary	$c_1 = \frac{-1}{2F_p}$	$d_1 = -\frac{F_2 - B}{1+A_2}$
2 Secondary	$c_2 = -\frac{1-A_2}{2F_2(2d_1c_1-1)}$	$d_2 = -d_1 + B + D_3$
3 Tertiary	$c_3 = \frac{-1}{2D_3}[1 - \frac{S_0S_1F_2}{F_3}]$	$d_3 = \frac{\|D_3\|S_1F_3}{F_2}$
4 Image	$c_4 = -2(c_1 - c_2 + c_3)$	na

Focal length of the primary mirror $F_p = 2Y_1F_{pri}$
Focal length amplification of the two mirror system $A_2 = \frac{F_2}{F_p}$
Logical variables defined $S_0 = \frac{\|D_3\|}{D_3}$ and $S_1 = -\frac{\|F_2\|}{F_2}$

$\{Y_1,\ F_3,\ F_{pri},\ F_2,\ \mathrm{B},\ D_3,\ \mathrm{FoV}\}$ fundamental design parameters. We need to set the remaining parameters so that we can solve for the constructional parameters. We explain in detail the procedure we used to set the remaining parameters for both the OTMA and UTMA design.

III.2.3.1 Constructional Parameters for OTMA design

The fundamental design parameters which are to be set are $\{F_{pri},\ F_2,\ \mathrm{B},\ D_3\}$. We begin with F_{pri}. The focal length of the primary mirror $F_p = 2Y_1F_{pri}$. Since we are interested in a Cassegrain type telescope d_1 (distance between the primary and secondary mirror) should be less than F_p. Small values of F_p are preferred for efficiently packing the design. There is no best value for F_{pri}, so we choose a range of values for F_{pri} like $0.5<F_{pri}<1.5$.

For each F_{pri} in this range, we need to constrain the allowable values for d_1. If $d_1 << F_p$ the secondary mirror will have a large size resulting in large obstruction and if $d_1 \sim F_p$ secondary mirror starts to depart from the conic surface defined. So we constrain d_1 between $0.8F_p<d_1<0.9F_p$. Next, for every combination of F_{pri} and d_1 we find the minimum value for F_2 such that $F_2 > 0$ and B$= 0$ using the equation given below.

Table III.2.4: Fundamental design parameters of the chosen OTMA and UTMA designs

Design	Y_1[m]	F_{pri}	F_2[m]	B[m]	D_3[m]
OTMA1	0.60	1.00	10.25	0.96	0.46
scaled OTMA1	1.50	0.40	10.25	0.96	0.46
OTMA2	0.60	4.50	22.00	0.99	4.58
scaled OTMA2	1.56	1.73	22.00	0.99	4.58

F_3 = 24.5 m for all the above
scaled OTMA is used as UTMA

$$F_{2min} = \frac{-d_1}{1 + d_1/F_p} \tag{III.2.2}$$

The value of F_2 is positive for Cassegrain type telescope and B> 0 implies the tertiary mirror is beyond the vertex of the primary mirror. Now, F_2 can be chosen to be any number greater than F_{2min} and the corresponding value of B can be found using equations given in table III.2.3. For some arbitrary combination of $\{F_{pri}$, F_2, B$\}$, the value of D_3 can be found using the Petzval condition for flat focal plane. There are two possible solution for D_3, positive or negative. We choose the positive value so that the the design can be folded.

Using the method detailed above we can obtain a large family of solutions for the fundamental design parameters. In this large family of solutions, all the designs can be optimised to be diffraction limited in the desired field–of–view. Therefore, we arbitrarily chose one set of fundamental design parameters to serve as our OTMA telescope. For a given set of fundamental design parameters, the constructional parameters can be obtained from the equations given in table III.2.3. The fundamental design parameters of the chosen OTMA design are given in table III.2.4 and the constructional parameters for the same are given in table III.2.5.

Table III.2.5: Constructional parameters of the chosen OTMA and UTMA designs

Parameter†	OTMA1	UTMA1	UTMA2
c_1	$-1/2399$	$-1/2399$	$-1/10800$
c_2	$-1/513$	$-1/513$	$-1/3339$
c_3	$+1/652$	$+1/652$	$-1/4834$
d_1*	-973	-973	-4140
d_2*	$+2038$	$+2038$	$+9722$
d_3*	-1105	-1105	-5108
k_1	-0.995	-0.995	-0.929
k_2	-1.561	-1.561	-2.108
k_3	-0.756	-0.756	-0.425
h_1*	na	900	1050
h_2*	na	180	267
h_3*	na	0	0
Primary Mirror diameter*	1200	1200	1200
Secondary Mirror diameter*	246	246	331
Tertiary Mirror diameter*	276	150	876

† cf section 2.1 for explanation

* in units of mm

III.2.3.2 Constructional Parameters for UTMA design

The designs of UTMA telescopes were discussed by Cook (1979) and Korsch (1980). The work by Cook (1979) illustrates two examples of UTMA telescopes, but no analytical or numerical methods are provided to obtain those designs. The work by Korsch (1980) gives a rigorous numerical technique to determine the shape of the mirror surfaces. Though, the method proposed by Korsch (1980) is very general it has two caveats. First, it is not straightforward to study the design with modern ray-tracing softwares because this method uses non-conic surfaces. Second, the design is optimised to be diffraction limited only for the central field-of-view. In contrast to these approaches, we propose here a simple method to design an UTMA telescope from an OTMA telescope.

Procedure To Design a UTMA Telescope From an OTMA Telescope

The basic idea of the procedure is illustrated in Figure III.2.2. We design an OTMA telescope using the method described in section III.2.4 and then we select an unobstructed sub–pupil from the primary mirror of the OTMA telescope. This unobstructed portion is used as a stand-alone UTMA telescope. The resulting telescope has a smaller primary mirror compared to the original OTMA telescope. To obtain an UTMA telescope with the desired aperture, we scale the OTMA telescope before selecting the sub-pupil. We explain our procedure to compute the scale–factor below.

Procedure to compute scale–factor

We use the paraxial ray-trace equations and the condition that no rays incident on the primary surface should be obstructed by the secondary surface and tertiary surface (no vignetting) to obtain the scale–factor. This ensures that the UTMA pupil is uniformly illuminated. Let y_j, d_j, i_j, u_j be the paraxial ray height, separation from the next surface, angle of incidence and angle after reflection.

Figure III.2.2: **Procedure to design a UTMA telescope:** A step-by-step pictorial representation for designing an UTMA telescope from an OTMA telescope is shown in this figure. Left panel is the initial OTMA1 telescope. Central panel is a scaled-OTMA1 telescope (here, scale factor $s \approx 2.5$). Right panel is a sub-part of the scaled telescope that is used as a stand-alone UTMA telescope. The fundamental parameters for all the telescopes are given in table III.2.4. The lines in the figure correspond to the light rays traced.

We already defined Y_1 to be the height of the primary mirror, let the height of the scaled mirror be $Y_1'(= sY_1)$, where s is the scale–factor. Similarly, we denote the heights of the secondary mirror and the scaled secondary mirror by Y_2 and $Y_2'(= sY_2)$. Using the ray trace equations in Born and Wolf (1965) we obtain the scale–factor as follows.

$$
\begin{aligned}
y_j &= y_{j-1} + d_{j-1}u_{j-1} && \text{(III.2.3)}\\
i_j &= y_j c_j + u_{j-1} && \text{(III.2.4)}\\
u_j &= u_{j-1} - 2i_j && \text{(III.2.5)}\\
y_2 &= y_1 + d_1 u_1 && \text{(III.2.6)}\\
u_1 &= -2i_1 && \text{(III.2.7)}\\
&= -2y_1 c_1 &&\\
y_2 - y_1 &= d_1(-2y_1 c_1) && \text{(III.2.8)}\\
Y_1' - Y_2' &= 2Y_1' c_1 d_1 && \text{(III.2.9)}\\
\text{aperture of the UTMA} &= 2sY_1 c_1 d_1 && \text{(III.2.10)}\\
s &= \frac{\text{aperture of the UTMA}}{2Y_1 c_1 d_1} && \text{(III.2.11)}
\end{aligned}
$$

We find that scaling does not change constructional parameters, but it does change fundamental design parameters. Keeping the primary mirror focal length invariant requires us to adjust the primary mirror focal ratio ($F_p = 2F_{pri}Y_1 = 2F'_{pri}Y_1'$). Or in other words scaling Y_1 by a factor s decreases F_{pri} by the same factor. We explain below how the decrease in F_{pri} affects some critical characteristics of the UTMA design.

Constructional parameters of UTMA1 design

Using the procedure detailed above, we scaled the OTMA1 design and obtain the scaled–OTMA1 design whose fundamental design parameters are shown in Table III.2.4. The scale-factor calculated using equation III.2.11, is approximately 2.5.

From the scaled design we select an unobstructed sub-pupil and call it our UTMA1 design. The constructional parameters of the UTMA1 design are same as the OTMA1 design. Unfortunately, this UTMA1 design has an intrinsically narrow diffraction-limited field–of–view. We compute the FoV to be 0.3×0.2 deg^2 (computed using ZEMAX). The reason for this narrow FoV is the decrease in F_{pri} when we scaled the OTMA1 design, because F_{pri} is the only fundamental design parameter which changed when we scaled the design. The UTMA1 design is not suitable for a wide field survey because of its narrow FoV, but science requirements less demanding in field size may find this design as a compact solution.

Constructional parameters of UTMA2 design

A convenient way of increasing the UTMA FoV, is to start with an OTMA telescope having a large F_{pri}. This is done at the expense of compactness of the final design. We use the same procedure in section III.2.4, but the initial range we set for the F_{pri} is now $4<F_{pri}<5$. With this starting point we again obtain a large family of OTMA designs. The crucial difference is in these designs the distance between the primary mirror and secondary mirror is increased by four fold. Lampton et al. (2010) mention the same when discussing the challenges in adopting a UTMA designs. Similar to OTMA design, we generate a large family of fundamental design parameters and arbitrarily choose one design to model the UTMA telescope. We call the chosen design OTMA2 and its fundamental design parameters are given in table III.2.4. The OTMA2 design is scaled by a scale-factor 2.6 to obtain the UTMA2 design. The constructional parameters for UTMA2 are shown in Table III.2.5. Hereafter, we call the chosen obstructed design OTMA and unobstructed design UTMA.

III.2.4 Design Optimisation Using ZEMAX

In the previous section we set the fundamental design parameters and computed the constructional parameters for an OTMA and a UTMA design. The parameters were chosen to minimise three main aberrations in the desired field–of–view. We model

these designs in an optical design tool and optimise the constructional parameters to reduce higher order aberrations. The optical design tool we chose for this purpose is ZEMAX[1].

ZEMAX inputs

The inputs for ZEMAX are the constructional parameters of the designs given in table III.2.5. We also set the field–of–view of the telescope in ZEMAX, by assigning 12 regions as shown in figure III.2.3. Besides the constructional parameters and the FoV, we also need to specify the operating wavelength for both the telescopes. Important properties like the PSF and EE depend on the operating wavelength of the telescope. ZEMAX accepts discrete wavelengths as inputs to compute the PSF and EE. Later it extrapolates the results to include all wavelengths between the minimum and maximum value.

Spot Diagram

Using the constructional parameters in Table III.2.5, we model the telescope designs in ZEMAX. We compute the spot diagram at various regions in the field–of–view to verify whether the design in diffraction limited. In left panel of figure III.2.4 we show the spot diagram of field–of–view point labeled '1' in figure III.2.3 for the OTMA design before optimisation. We find the design is still aberration limited at the chosen location in the field–of–view. We need to optimise the constructional parameters to make the design diffraction limited in the desired field–of–view.

Design Optimisation

The optimisation feature of ZEMAX has the capability to transform an aberration limited design into a diffraction limited one given a reasonable starting point and a set of variable parameters. In our case the variable parameters are the constructional parameters given in table III.2.5 and the higher order aspheric coefficients in equation III.2.1. The optimisation algorithm is ZEMAX uses a merit function to represent how

[1] www.zemax.com

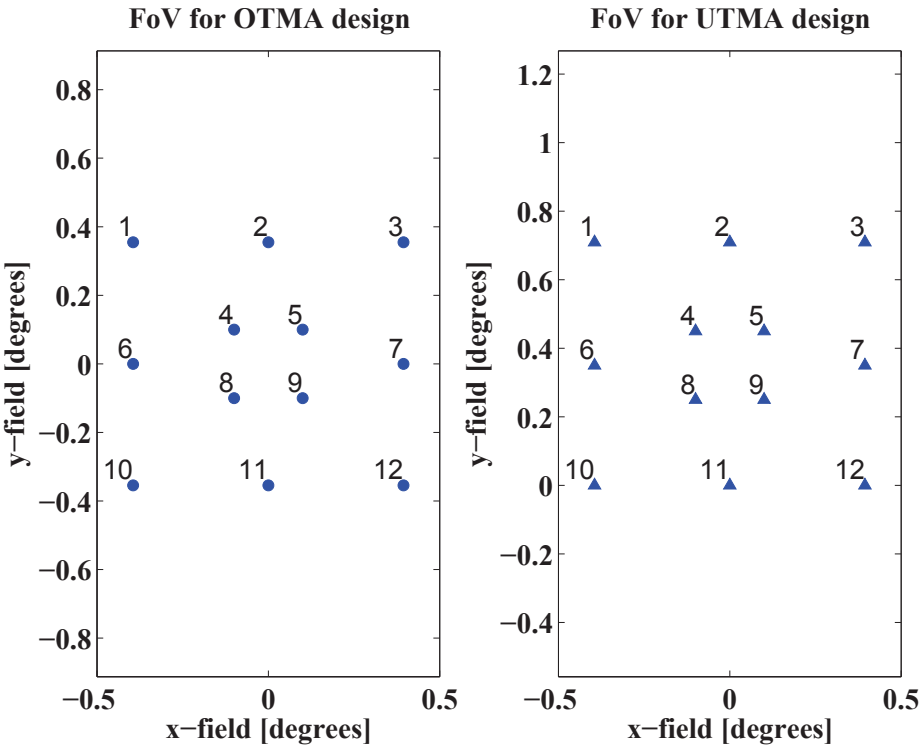

Figure III.2.3: **Field–of–View for the OTMA and UTMA design:** The fiel–of–view points for the chosen OTMA and UTMA telescopes are shown. Both the designs have a FoV of 0.787×0.709 deg^2. For the OTMA design on the left panel light rays with angle $\bar{u}_0$ and -$\bar{u}_0$ are brought to focus. To achieve the same field of view in an UTMA design light rays with $\bar{u}_0$ and $2\bar{u}_0$ are brought to focus.

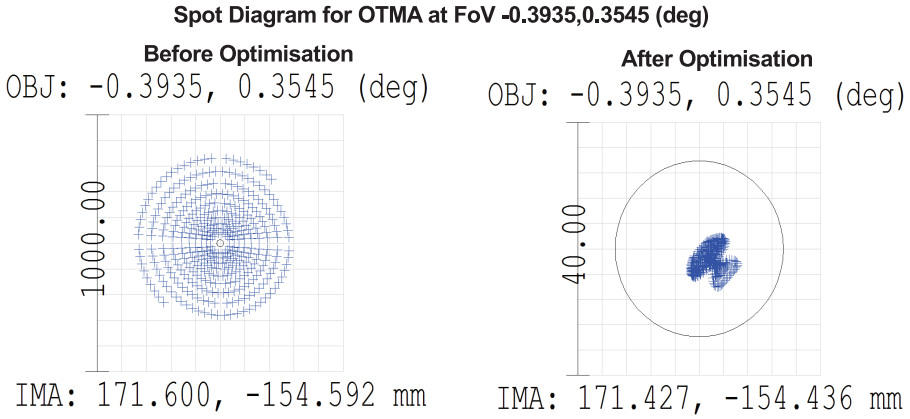

Figure III.2.4: **Spot diagram for TMA design before and after optimisation:** Both panels show the spot diagram for the field–of–view point labaled '1' in figure III.2.3 of the OTMA design. The left panel is before optimisation and right panel is after optimisation. In the right panel the telescope is diffraction limited at the this location in the field–of–view. We can see that the aberrations are contained within the Airy disk. We achieve similar spot diagrams at all other locations shown in figure III.2.3.

closely an optical system meets the specified requirements. The merit-function value is the square root of the weighted sum of the squares of the difference between the actual and desired value of the list of constraints. We constrained the spot radius to a diffraction limited value and run the optimisation algorithm of ZEMAX to find the best values for the constructional parameters.

After optimisation we compute the spot diagrams to verify whether the optimised design is indeed diffraction limited. In right panel of figure III.2.4 we show the spot diagram of field–of–view point labeled '1' in figure III.2.3 for the OTMA design after optimisation. We can see that the aberrations are contained within the Airy radius. We check the spot diagram at all the field–of–view points to verify that the design is diffraction limited everywhere. Thus the constructional parameters of both the OTMA and UTMA designs are optimised. In the next section we compute the PSFs of these optimised designs at various locations in the field–of–view.

III.2.5 PSF Computation Using ZEMAX

We compute the PSF at the desired locations in the field–of–view for the optimised OTMA and UTMA telescopes. ZEMAX computes the PSF using direct integration of Huygens wavelet. This approach is the most sophisticated method available in ZEMAX to compute the PSF. We recall that the PSF of a telescope depends on the operating wavelength. ZEMAX computes the PSF for a discrete set of wavelengths and extrapolates the results to the whole range of operating wavelength.

In figure III.2.5 we show the PSF for OTMA and UTMA telescope at field location labelled '1' in Figure III.2.3. The PSFs have a pixel scale of $0.025''$. We use the same pixel scale to simulate quasi-realistic galaxy images in section III.3.2.3. At first glance, we can see that the the UTMA PSF on the right panel (Figure III.2.5) is rotationally invariant and does not show any features. On the other hand the OTMA PSF shows distinct spikes, which are caused by the secondary mirror support structure. We computed the PSFs at all locations in the field–of–view shown in figure III.2.3. Then, we normalised the total intensity of the PSF to unity and converted them into FITS images.

Variation of PSF over the field–of–view

It is not possible to distinguish between the PSFs at various locations in the field–of–view by naked eye so we computed the correlation coefficient between the PSFs at various locations. For the OTMA design the mean value of the correlation coefficient is 0.9851 and for the UTMA design the mean value is 0.9999. These values indicate that the OTMA PSF changes significantly over the field–of–view compared to the UTMA case. In chapter III.4 we study how the variation of the PSF and uncertainty in its knowledge affect the measurement of weak lensing observables.

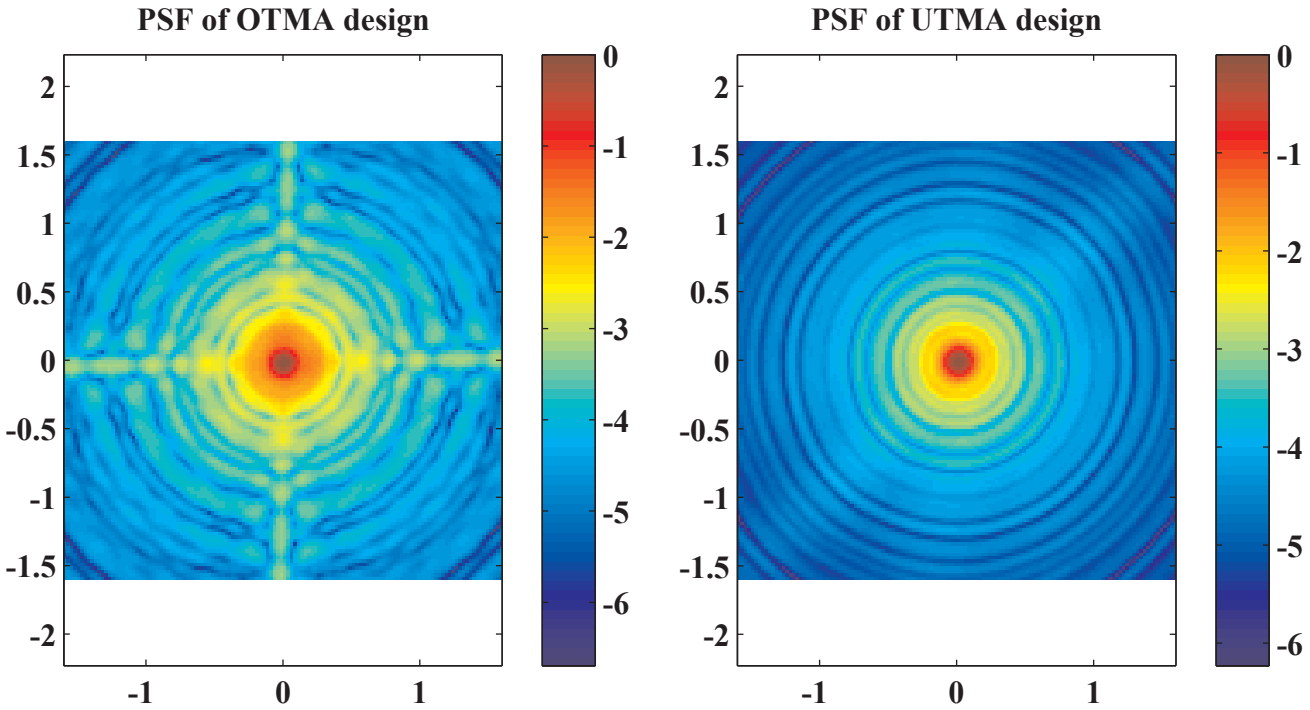

Figure III.2.5: **An example PSF for the OTMA and UTMA design:** A sample PSF for both the OTMA and UTMA designs at FoV location labelled '1' in Figure III.2.3. The pixel scale in the image is 0.025″. The OTMA PSF on the left panel shows diffraction spikes due to the presence of spider support structure. The scale to the right of the figure is logarithmic in powers of 10.

III.2.6 Summary

In this section we described the telescope design parameters, the procedure to set the fundamental design parameters and the procedure to compute the constructional parameters. Then, we obtained the constructional parameters for an OTMA and a UTMA design and optimised the parameters in an optical design program ZEMAX. Finally, we computed the PSF at various locations in the field–of–view for the optimised OTMA and UTMA telescope. In the next chapter we use the OTMA and UTMA PSFs to simulate galaxy images similar to ones observed using real telescopes.

Chapter III.3

Image Simulation And Model Fitting

We recall from section III.1.5 that our objective is quantify the precision with OTMA and UTMA telescopes can measure weak lensing observables. To perform this study we need galaxy images observed using both the telescopes and a rigorous method to measure the axis ratio and position angle of galaxies. In this chapter we first present the procedure we used to simulate quasi–realistic images of galaxies. next, we present a rigorous method to measure the axis ratio and position angle of galaxies from the simulated images.

III.3.1 Procedure to Simulate Quasi–Realistic Galaxy Images

The final focused image of a telescope is the convolution of the astronomical object and the PSF of the telescope at the field of view. This image is pixellated due to the nature of the imaging system. In addition to the flux obtained from the astronomical source, there is a non negligible amount of noise present in the images. We need to take into account all the factors mentioned above in order to produce a quais–realistic galaxy image as observed through the telescope.

The pipeline we used to simulate galaxy images is shown in figure III.3.1. First we simulated galaxy images with no PSF artefacts using ASTROMATIC[1] tools developed by Bertin (2009). Next, we convolve these images using the PSF computed in section III.2.5. This gives us PSF convolved images with desired pixel size. Then, we add sky background noise (poissonian noise) to the pixellated images. Finally, we obtain a quasi-realistic images, which are equivalent to real images observed with a telescope. We explain each step in the pipeline below.

III.3.1.1 Step 1 - Create a catalogue of galaxies

In this section we describe our procedure to simulate a catalogue of galaxies. We use a tool called STUFF developed by (Bertin, 2009) to create a catalogue of galaxies. Using STUFF one can create a realistic catalogue of astronomical sources with a desired apparent magnitude, spectral energy distribution and galaxy luminosity function. The output of the STUFF catalogue generator is a list of galaxies with their coordinates, effective radius, apparent magnitude, axis ratio, position angle and redshift.

To simulate our catalogue of galaxies we set the allowed range of apparent magnitude between 23 mag and 24 mag. We recall that the *Euclid* mission is magnitude limited at 24.5 mag in visual band. For the spectral energy distribution we choose only elliptical galaxies because the axis ratio and position angle is well defined only for these galaxies. Since we are primarily interested in comparison of two designs, elliptical galaxies will serve as a good starting point. We can later include all other galaxies to increase the robustness of our results. The important inputs for STUFF routine are given in table III.3.1.

The catalog generated using STUFF contains the morphological parameters of a large number of galaxies with a wide range of axis–ratios. For simplicity, we divide the sample into 8 bins according to the galaxy axis–ratio. Table III.3.2 shows the bins, they are labelled Q1 through Q8. Binning allows us to study how galaxies with different axis-ratio are affected by the PSF of the telescopes. We include 100 galaxies

[1] www.astromatic.net

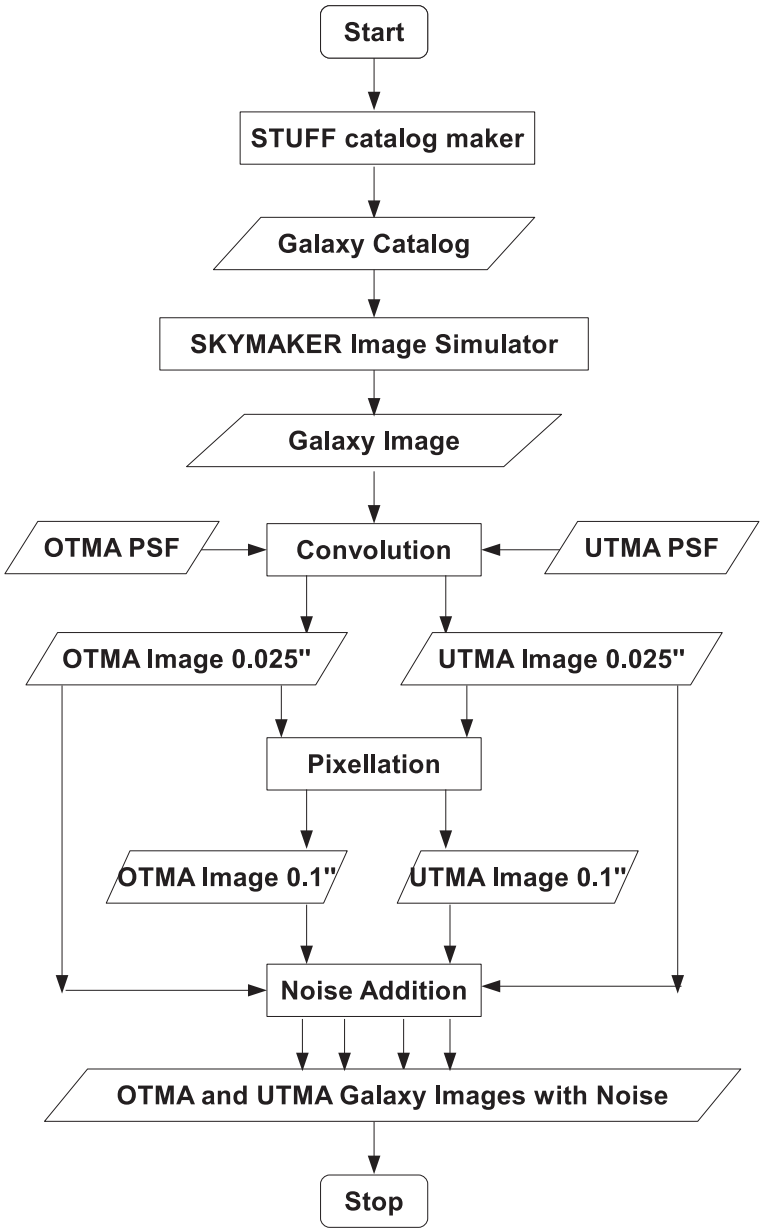

Figure III.3.1: **Flowchart showing the pipeline used to simulate galaxy images:** Consult section III.3.1 for detailed description.

Table III.3.1: Essential inputs for STUFF – galaxy catalog generator

Input parameter	Value
Range of apparent magnitudes	23-24
Pixel size (arcsec)	$0.025''$
Effective collecting area (m^2)	78.53[1] (corresponds to 10m aperture)
Cosmological parameters	$\{\Omega_M = 0.3, \Omega_\Lambda = 0.7, H_0 = 70\}$
SEDs for galaxy components	E (only elliptical galaxies)

[1] Initial image is simulated for a large telescope so that the PSF effects are negligible.

Table III.3.2: Binning of the simulated galaxies with respect to axis ratio

Bin Name	Axis ratio	Half-light Radius [arcsec]	
		Mean	Variance
Q1	<0.3 (*slender*)	0.2038	0.0014
Q2	0.3-0.4	0.1956	0.0010
Q3	0.4-0.5	0.1915	0.0007
Q4	0.5-0.6	0.1980	0.0022
Q5	0.6-0.7	0.2063	0.0028
Q6	0.7-0.8	0.1974	0.0010
Q7	0.8-0.9	0.1922	0.0007
Q8	>0.9 (*circular*)	0.2076	0.0042

in each bin to perform statistical analysis in our precision measurement.

III.3.1.2 Step 2 - Simulate Galaxy Images

We use the tool SKYMAKER (Bertin, 2009) to simulate FITS images of the galaxies. SKYMAKER creates FITS image of astronomical sources for a given catalogue (generated using STUFF) and telescope characteristics. SKYMAKER can take care of all factors like PSF convolution and noise which affect real observed images. We did not use those features of SKYMAKER because we computed more sophisticated PSFs using ZEMAX, which are specific for our design. We use SKYMAKER to simulate

Table III.3.3: Essential inputs for SKYMAKER – galaxy image simulator

Input parameter	Value
M_1 *PM* diameter (m)	10
Exposure time (seconds)	58[1]
Magnitude Zeropoint (mag)	30.7
Pixel size ($arcsec$)	0.025
Background surface brightness ($mag/arcsec^2$)	50

[1] The Exposure time is for a 10m telescope. To obtain the same flux a 1.2-m telescope should have an exposure time in the order of 4050 seconds (Schroeder, 1987).

galaxy images with no PSF artifact or noise.

The essential inputs we used for the SKYMAKER are given in table III.3.3. We use the characteristics of a 10m telescope to minimise the PSF effects on the simulated image. To prevent SKYMAKER from adding noise to the image, we set the readout noise to 0 e^{-1} and the background surface brightness to a very low 50 mag/arcsec^2. For each galaxy in our catalogue, we create 512×512 pixels FITS image centred on galaxies. The pixel size used in the images is 0.025″. The galaxies have a de–Vaucouleur profile whose apparent magnitude, effective radius, axis ratio and position angle are defined in the catalog. Next, we need to convolve the images with OTMA and UTMA PSF to obtain images equivalent to ones observed using these telescopes.

III.3.1.3 Step 3 - PSF Convolution

The images simulated in the previous section contain no PSF artifacts. To introduce the PSF effects of the OTMA and UTMA design we convolve the output images of SKYMAKER with the PSFs computed in section III.2.6. The SKYMAKER images and the computed PSF have the same pixel scale of 0.025″. After convolution, we split the PSF convolved images into two pipelines. In the first pipeline we have images with pixel scale 0.025″ and in the second the images are pixellated to pixel scale 0.1″.

This allows us to test how the pixel scale affects the precision measurement of weak lensing observables. We use PYTHON's SCIPY library to perform the convolution.

We have 100 images in 8 axis ratio bins, which totals 800 galaxies. We need to convolve these 800 galaxies with both the OTMA and UTMA PSF to obtain PSF convolved images. Since PSF convolution is computationally time consuming, we choose one PSF for both the designs and convolve the images with this PSF. We chose the PSF from the FoV location labeled '1' in the figure III.2.3 for convolution. This is equivalent to saying the images are located in the top left corner of the image plane. Our method of analysis ensures that the final results should not vary if this PSF is replaced by any other in the FoV.

III.3.1.4 Step 4 - Noise addition

The PSF convolved images obtained in the previous step have an infinite S/N. We need to bring the S/N to a finite value because real observed images contain a variety of noise. The major noises present in an image are the sky background noise and readout noise. The sky background noise is a Poissonian and increases proportional to exposure time. The readout noise is Gaussian, intrinsic to CCDs and is given by the manufacturer in units of number of electrons. Besides these real images have dark current noise and shot noise, but their contribution is minimal and can be corrected for. Dark current noise can be subtracted from the image by analysing dark frames and shot noise can be lowered by increasing exposure time or number of exposures.

To lower the S/N of the simulated images to a finite value, we add poissonian noise equivalent to sky background of 30 mag/arcsec^2 to the PSF convolved images. For realistic sky background (Leinert et al., 1998) we need to increase the exposure time to obtain the same S/N. We do not add the readout noise because we assume it will affect the both the OTMA and UTMA design in the same way. If the precision measurement of weak lensing observables are dominated by noise and not by PSF, then there is no rational reason to compare the two designs. Therefore, testing with just a low hypothetical sky background noise is a good starting point.

The end product of this procedure is a set of 800 FITS images of faint elliptical

galaxies in 2 different pixel scales (0.025″ and 0.1″) for both the OTMA and UTMA designs. In the next section we will fit the morphological properties for each galaxy and compare the precision with which the OTMA and UTMA can deliver those measurements.

III.3.2 Procedure to measure galaxy morphology

In previous section we simulated realistic images of galaxies for both the OTMA and UTMA design. Now we would like to measure the axis ratio and position angle of these galaxies and compare them with the simulated values in our STUFF generated catalogue. There are several methods available to measure the axis ratio and position angle of a galaxy from an observed image. We use two methods SEXTRACTOR by Bertin and Arnouts (1996) and GALFIT by Peng et al. (2010) for measuring the weak lensing observables. In sections III.3.2.1 and III.3.2.2 we show how to use these methods to compute the desired morphological parameters from simulated images. We also list the advantages and disadvantages of using these methods to compute the desired parameters.

III.3.2.1 Method 1 - SEXTRACTOR

The SEXTRACTOR routine can extract astronomical sources from images and perform photometry, astrometry and image moments. We use SEXTRACTOR to compute the axis ratios and position angles of the simulated galaxies. SEXTRACTOR uses a threshold value to distinguish between the background and the astronomical source. Then, it measures image moments and performs required photometry on the extracted source. The advantage of using SEXTRACTOR are it takes only a trivial amount of time to run on a large set of images. The disadvantage of using SEXTRACTOR is it does not take the PSF of the telescope into account when computing the axis ratio and position angle.

We computed the axis ratio and position angle for all the simulated galaxies using SEXTRACTOR. Then, we compared the simulated axis ratio with computed axis ratio

to quantify the error. We find that SExtractor systematically overestimates the axis ratio for all the simulated galaxies. We observe this for both extremes of the threshold value chosen for SExtractor. For increasing values of the threshold SExtractor extracts only the core of the galaxy considering the outer regions as noise. This results in severe error in axis ratio measurement because the core smeared by the PSF is almost circular for all the galaxies. For decreasing values of the threshold SExtractor includes random noisy pixels as a part of the image, which along with PSF smearing prevents us from computing the exact value. There is no best value for the threshold parameter if we want to perform measurements on a large set of images. For this reason we don't find SExtractor as a rigorous method to compare the precision of the two telescopes. Nevertheless, SExtractor does provide a good first order approximation of the axis ratio and position angle measurement, which we use as initial values for our next method.

III.3.2.2 Method 2 - GALFIT

GALFIT is a data analysis algorithm that fits 2-D analytic functions to galaxies by optimising a set of morphological parameters over an input image. The 2-D analytic function we fit for the galaxies is 'de Vaucouleur' function because we simulated the galaxy images using the same. The morphological parameters defining a 'de Vaucouleur' function are apparent magnitude, effective radius in pixels, axis ratio and position angle.

Advantages of GALFIT

The two main advantages of using GALFIT to compute the axis ratio and position angle are as follows. First, GALFIT includes the PSF of the telescope in its fitting process, which allows us to answer the questions we posed in section III.1.5. Second, GALFIT computes a reduced chi-squared to indicate the goodness of fit. This value can be used to reject solutions which are over fitted ($\chi^2 < 1$) or under fitted ($\chi^2 > 1$). We accept the values computed by GALFIT only if $\chi^2 \sim 1 \pm 0.2$. The disadvantage of using GALFIT is it is computationally expensive when compared with SExtractor.

Inputs for GALFIT

The inputs for the GALFIT routine are the input image, the PSF, magnitude zeropoint, exposure time, sky background and initial values for the 2-D analytic function we wish to fit for the galaxies. The galaxy image is a straight forward input for GALFIT. We discuss the input PSF in section III.4.2. For a 1.2m telescope the magnitude zeropoint given by STUFF is 26.1 mag. The GALFIT results are sensitive to the sky background value and GALFIT allows the user to either set the values as a constant or leave it as a free parameter for the fit. For the simulated images we added a sky background noise of 30 $mag/arcsec^2$ but GALFIT requires the sky background to be set in ADU counts. Since we do not know the exact value of our hypothetical sky background in ADU, we find the best fit value for the sky manually. We fit all the 100 galaxies in the Q5 bin (cf. table III.3.2) by varying the sky value. We then compute the mean and variance of the χ^2 obtained for all the galaxies. The best sky value is one for which the the mean is close to 1 and the variance is smallest.

Next, we set the initial values for parameters of the 'de Vaucouleur' function we wish to fit for the galaxies. GALFIT allows the user to fit all the parameters or only a selected few leaving the others fixed. In this study we fixed the apparent magnitude and fit all the other parameters of the 'de Vaucouleur' function. The reason we fix the apparent magnitude is we do not want the fitting method to dominate the measurement of weak lensing observables. The initial values for the axis ratio and position angle are set by the values computed using SEXTRACTOR. We set the initial value of the effective radius as $\sim 0.2''$, because this is the average value of the effective radii of the simulated galaxies (cf. table III.3.2). Finally, we run GALFIT to compute the best fit values for the axis ratio and position angle for a given galaxy.

III.3.3 Summary

In this chapter we showed how to simulate quasi-realistic galaxy images equivalent to ones observed using real OTMA and UTMA telescopes. Then, we explained two methods which we use to measure the axis ratio and position angle of the simulated

galaxies. We explained the workings of these methods and their advantages and disadvantages. We use SExtractor to get an initial estimate on the axis ratio and position angle. Then, we use GALFIT to get a rigorous estimate of the same. In the next chapter we present the results obtained using GALFIT on the simulated galaxy images.

Chapter III.4

Results for Axis Ratio and Position Angle Measurements

In chapter III.2 we designed and optimised an OTMA and a UTMA telescope with similar characteristics. Then, we computed the PSFs of these telescopes at various locations in the field–of–view. In chapter III.3 we used the PSFs to simulate quasi-realistic galaxy images equivalent to images observed using the telescopes. Then, we explained the method we use to measure the axis ratio and position angle of the simulated galaxies. Now we have all the tools necessary to answer the questions we posed in section III.1.5.

The outline of the chapter is as follows. First, we present the procedure to quantify the precision with which the observables are measured. Next, we present three case studies and quantify the precision of both the OTMA and UTMA designs.

III.4.1 Procedure to Quantify Precision

Following the procedure in III.3.2.2 we measure the axis ratio and position angle of all the simulated images. The error in measured value is the difference between the simulated value and measured value. This error is computed for both the axis ratio and position angle. We recall that the images were divided into 8 axis ratio bins. For

the error measurement in each bin we compute the mean and 1σ standard deviation. The precision of a design is quantified by the 1σ standard deviation in the error. The design with the smallest value of 1σ standard deviation is the best design for measuring weak lensing observables. We perform 3 case studies and compute the mean and 1σ standard deviation of the errors.

III.4.2 Case Studies

In section III.3.2.2 we explained the procedure to run the GALFIT algorithm. We recall the inputs for GALFIT, which are the input image, the PSF, magnitude zeropoint, exposure time, sky background and initial values for the 'de Vaucouleur' function we wish to fit for the galaxies. We already explained how to set all the inputs for GALFIT. In these case studies we focus on the input PSF for the GALFIT routine. In real life scenarios there is always in uncertainty in the knowledge of the PSF, which affects the measurements of weak lensing observables. A brief description of each case study is as follows.

Case Study # 1 We assume there is no uncertainty in the knowledge of PSF. We input the exact same PSF we used for convolution to measure the axis ratio and position angle.

Case Study # 2 We assume a large uncertainty in the knowledge of PSF. We input a PSF which is 0.8 degrees away from the PSF we used for convolution.

Case Study # 3 We assume varying levels of uncertainty in the knowledge of PSF. We input PSFs which are $\{0.05,0.1,0.2,0.4\}$ degrees from the PSF used for convolution.

We present the results for each case study below.

III.4.2.1 Case Study # 1 – No Uncertainty in PSF

In this case study we use the same PSF (computed at point labeled '1' in Figure III.2.3) for both simulating the images and GALFIT fitting process. In tables III.4.1

and III.4.2 we present the mean error and 1σ error-bar for axis ratio and position angle measurements. We show error–bar plots for both the telescopes in figures III.4.1 and III.4.2. In both the Figures the x-axis runs from axis–ratio bin Q1(q < 0.3) through Q8(q >0.9). The results are presented for two different pixel scales $0.025''$ and $0.1''$.

Results for images with pixel scale $0.025''$

Figure III.4.1 shows the error-bar plot for axis–ratio and position–angle measurements for images with pixel scale $0.025''$. The results are almost same for both the OTMA and UTMA design. The mean error is close to zero for axis ratio measurement but the 1σ error-bar is high for slender galaxies and is negligibly small for circular galaxies. This is a consequence of the fact that the PSF of both the OTMA and UTMA designs smears the minor axis of the slender galaxies. In case of the position angle measurement the mean error is close to zero for both the designs and the 1σ error-bar is small for slender galaxies and increases as galaxies get circular. The PSF smearing makes all objects circular and this affects the precision with which position angle can be measured for intrinsically circular objects. The last bin Q8(q >0.9) is not shown for position angle plots because these objects are almost circular and there is no sense in measuring their position angle.

Results for images with pixel scale $0.1''$

Figure III.4.2 shows the error-bar plot for axis ratio and position angle measurement for images with pixel scale $0.1''$. The results similar to the case above. The only difference is in the case of large pixels, the mean error in axis ratio measurements are biased towards negative values. This implies that the axis ratio is always over estimated. This over estimation can be attributed to both the PSF smearing and large pixel size.

Conclusion for case study # 1

From the results obtained above we conclude that if the PSF is accurately reconstructed, we can perform the science measurements with the same precision using both the designs. The transfer of energy from the Airy disk to the outer rings and the diffraction spikes (cf. figure III.2.5) present in an OTMA PSF do not affect the science measurements of OTMA design if they are reconstructed accurately. Therefore, OTMA and UTMA design can measure weak lensing observables with same precision if the PSF can be accurately reconstructed.

Table III.4.1: The mean error in axis–ratio measurement and the 1σ error-bar for the same for case study #1

Axis–ratio bin	Pixel Scale 0.025″				Pixel Scale 0.1″			
	OTMA		UTMA		OTMA		UTMA	
	Mean error	1σ error-bar	Mean error	1σ error-bar	Mean error	1σ error-bar	Mean error	1σ error-bar
Q1	-0.0404	0.2056	-0.0869	0.1981	-0.3712	0.253	-0.3609	0.2549
Q2	0.045	0.0721	0.0177	0.0648	-0.1556	0.0519	-0.1474	0.0536
Q3	0.0523	0.0416	0.0333	0.0367	-0.1016	0.0266	-0.0949	0.0282
Q4	0.0401	0.0257	0.0292	0.0245	-0.0656	0.0155	-0.0612	0.0181
Q5	0.0355	0.0216	0.0296	0.0208	-0.0425	0.0121	-0.0389	0.0128
Q6	0.024	0.0189	0.0198	0.0197	-0.027	0.0107	-0.0249	0.0109
Q7	0.0133	0.0206	0.0121	0.0203	-0.0151	0.0091	-0.0135	0.009
Q8	0.0127	0.017	0.0138	0.0187	-0.0004	0.0097	0.0004	0.0102

Table III.4.2: The mean error in position–angle measurement and the 1σ error-bar for the same for case study #1

Axis–ratio bin	Pixel Scale 0.025″				Pixel Scale 0.1″			
	OTMA		UTMA		OTMA		UTMA	
	Mean error	1σ error-bar	Mean error	1σ error-bar	Mean error	1σ error-bar	Mean error	1σ error-bar
Q1	-0.0006	0.3289	-0.0165	0.2709	-0.0181	0.2982	-0.0038	0.3939
Q2	-0.065	0.4563	-0.0697	0.3959	-0.015	0.3288	-0.0056	0.4352
Q3	0.0046	0.7227	-0.0167	0.6791	-0.0597	0.4013	-0.0691	0.4913
Q4	-0.0389	1.0421	-0.0569	1.0044	-0.0845	0.4966	-0.0938	0.5733
Q5	0.1375	1.1953	0.1358	1.2191	0.0195	0.6845	0.0534	0.7226
Q6	-0.0004	1.8753	-0.058	1.8711	0.0575	0.896	0.0507	0.9819
Q7	-0.3974	3.6504	-0.33	3.5373	-0.1562	1.8145	-0.1337	1.8951
Q8	-0.3685	21.4918	-1.0727	27.5538	-1.4601	16.4343	0.9883	19.3395

III.4.2.2 Case Study # 2 – Large Uncertainty in PSF

In this case study we use different PSFs for simulation and fitting process. This is equivalent to real life cases where the PSF used for fitting has to reconstructed from the PSF computed at some other location in the field–of–view. To simulate such a scenario we use the PSF computed at the point labeled '1' (cf. figure III.2.3) for simulation and the PSF computed at the point labeled '11' for fitting. These two PSFs are 0.8 degrees apart in the field–of–view. In tables III.4.3 and III.4.4 we present the mean error and 1σ error-bar for axis ratio and position angle measurements. We show error–bar plots for both the telescopes in figures III.4.3 and III.4.4.

Results for images with pixel scale $0.025''$ and $0.1''$

For the OTMA design the error–bar in axis ratio and position angle measurements have increased when compared compared with case study # 1. The error–bar has increased by a factor of 2–4 depending on the axis ratio bins. For the UTMA design there is no significant change in the error–bars of both axis ratio and position angle when compared with case study # 1. For pixel scale $0.1''$ we again find the systematic error in axis ratio measurements of slender galaxies.

Conclusion for case study # 2

From the results obtained above we conclude that in the presence of PSF reconstruction errors, the UTMA design can perform science measurements with better precision when compared with OTMA design. In other words, even in the presence of PSF reconstruction errors the 1σ error–bars of the UTMA design do not change, but that of the OTMA increase for both the axis ratio and position angle measurements. Another important conclusion we draw from these results is that the UTMA PSF does not change significantly over the field–of–view when compared with the OTMA design. We discuss the reason for this in detail in section III.5.1.1.

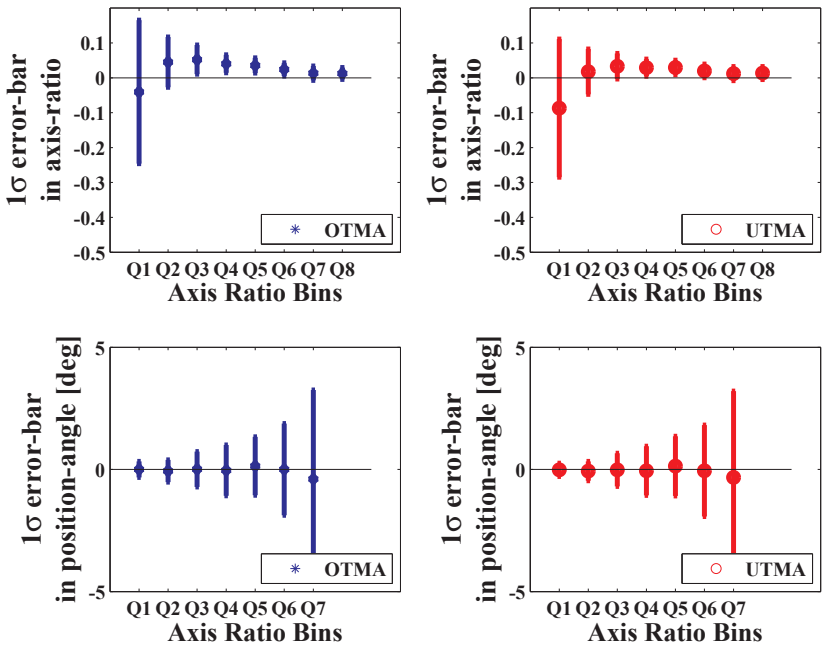

Figure III.4.1: **Error–bar plots for case study #1 - pixel scale 0.025″:** The error–bar plots corresponding to case study # 1 for axis ratio and position–angle measurements. The simulated images have a pixel scale of 0.025″.

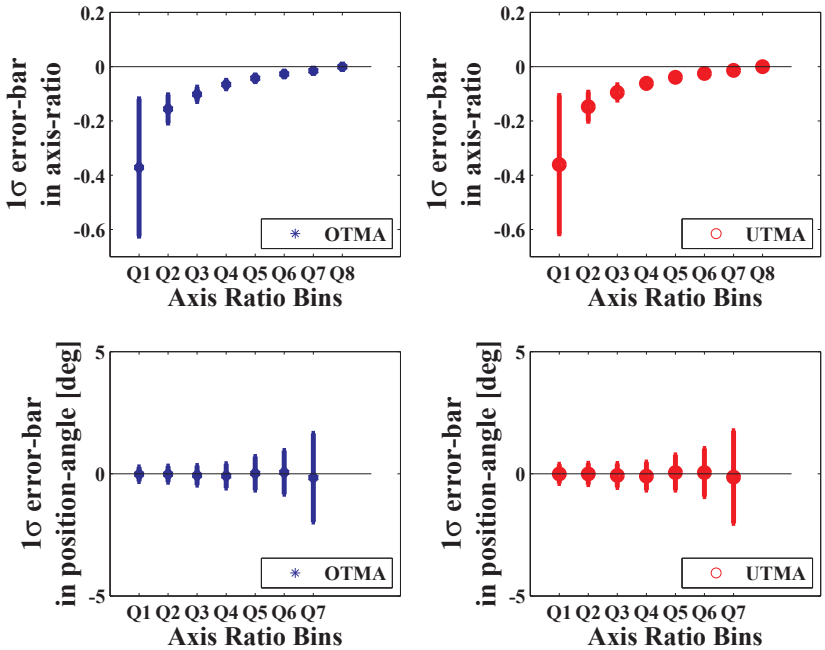

Figure III.4.2: **Error-bar plots for case study #1 - pixel scale 0.1″:** The error-bar plots corresponding to case study #1 for axis ratio and position angle measurements. The simulated images have a pixel scale of 0.1″. The large pixel size introduces a systematic bias in the axis ratio measurement for both the designs.

Table III.4.3: The mean error in axis–ratio measurement and the 1σ error-bar for the same for case study #2

Axis–ratio bin	Pixel Scale 0.025″				Pixel Scale 0.1″			
	OTMA		UTMA		OTMA		UTMA	
	Mean error	1σ error-bar	Mean error	1σ error-bar	Mean error	1σ error-bar	Mean error	1σ error-bar
Q1	0.082	0.288	-0.1001	0.1985	-0.2982	0.2297	-0.3805	0.2628
Q2	0.0944	0.176	0.009	0.065	-0.1267	0.1108	-0.1569	0.0513
Q3	0.1109	0.1383	0.026	0.0369	-0.0696	0.0765	-0.1037	0.0296
Q4	0.0709	0.1332	0.0251	0.0245	-0.051	0.0749	-0.0664	0.0181
Q5	0.075	0.1127	0.0269	0.0195	-0.0226	0.0591	-0.0438	0.0154
Q6	0.0481	0.1114	0.0177	0.018	-0.0191	0.0578	-0.0275	0.0143
Q7	0.0636	0.0885	0.0109	0.0183	-0.0011	0.0512	-0.0149	0.0118
Q8	0.1078	0.049	0.012	0.0175	0.039	0.0354	0.0022	0.0115

Table III.4.4: The mean error in position–angle measurement and the 1σ error-bar for the same for case study #2

Axis–ratio bin	Pixel Scale 0.025″				Pixel Scale 0.1″			
	OTMA		UTMA		OTMA		UTMA	
	Mean error	1σ error-bar	Mean error	1σ error-bar	Mean error	1σ error-bar	Mean error	1σ error-bar
Q1	0.2494	2.4463	-0.0195	0.2412	0.1196	1.578	-0.0173	0.4011
Q2	-0.1053	3.0449	-0.072	0.3546	-0.0004	2.0329	-0.0018	0.4576
Q3	-0.3525	3.8699	-0.0466	0.5481	-0.2501	2.4371	-0.0559	0.5421
Q4	-0.1876	5.386	-0.0899	0.8272	-0.0634	3.1799	-0.1272	0.657
Q5	0.8968	7.107	0.0479	1.0383	0.552	4.1362	-0.0234	0.935
Q6	-0.3629	11.1505	-0.0641	1.64	0.042	6.1979	0.0555	1.2076
Q7	-1.0651	24.6023	-0.3125	3.1533	-0.5958	12.8972	-0.0202	2.3305
Q8	-3.7607	46.6307	-0.8581	28.2858	-3.7111	42.5253	-5.7275	23.0076

III.4.2.3 Case Study # 3 – For Varying Levels of Uncertainty in PSF

In this case study we use PSFs computed at intermediate points between the PSF used for simulation (labeled '1' in the figure III.2.3) and the furthest PSF (labeled '11' in the Figure III.2.3) as the input PSF for GALFIT routine. The PSFs are sampled at 4 positions {0.05,0.1,0.2,0.4} degrees from the PSF used for simulation. Since the precision of the UTMA is not affected in case study # 2, we perform this study only for the images from OTMA design. We studied only the images in axis ratio bin Q5 (cf. table III.3.2) with pixel size $0.025''$ and we extrapolate the results to all the axis ratio bins in general. In figure III.4.5 we show the mean error and 1σ error–bar for axis ratio and position angle measurement for various level of uncertainty in the PSF. The mean error and 1σ error-bar for the same are also given in table III.4.5.

Conclusion for case study # 3

From figure III.4.5 we conclude that the error–bar for axis ratio and position angle is increases as the distance between the PSF used for simulation and the PSF used for fitting increases. We find that the precision of the OTMA design is equivalent to that of the UTMA design when the PSF used for fitting is computed within 0.2 degrees or 12 arc-minutes from the simulated PSF. This implies that for real galaxy images if the PSF can be reconstructed within 12 arc-minutes from the galaxy's position in the field–of–view, both OTMA and UTMA will deliver the same precision.

III.4.3 Summary

In this chapter we computed the axis ratio and position angle of the simulated images using GALFIT. We changed the input PSF for GALFIT to emulate real life scenario where there is always an uncertainty in the PSF. We briefly discussed the results obtained for each case study. In the next chapter we present in detail the answers to the questions we posed in section III.1.5.

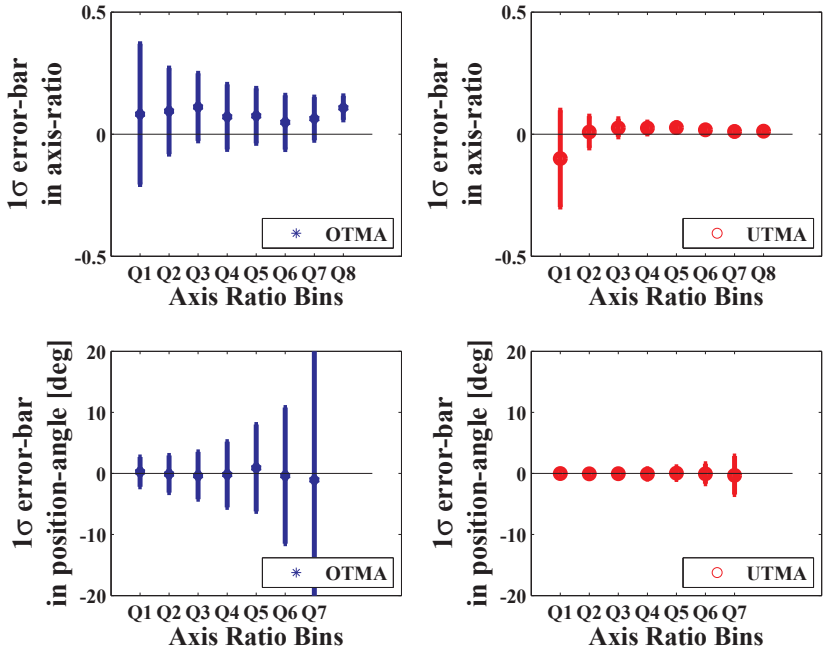

Figure III.4.3: **Error–bar plots for case study # 2 - pixel scale 0.025″:** The error-bar plots corresponding to case study #2 for axis ratio and position angle measurement. The simulated images have a pixel scale of 0.025″.

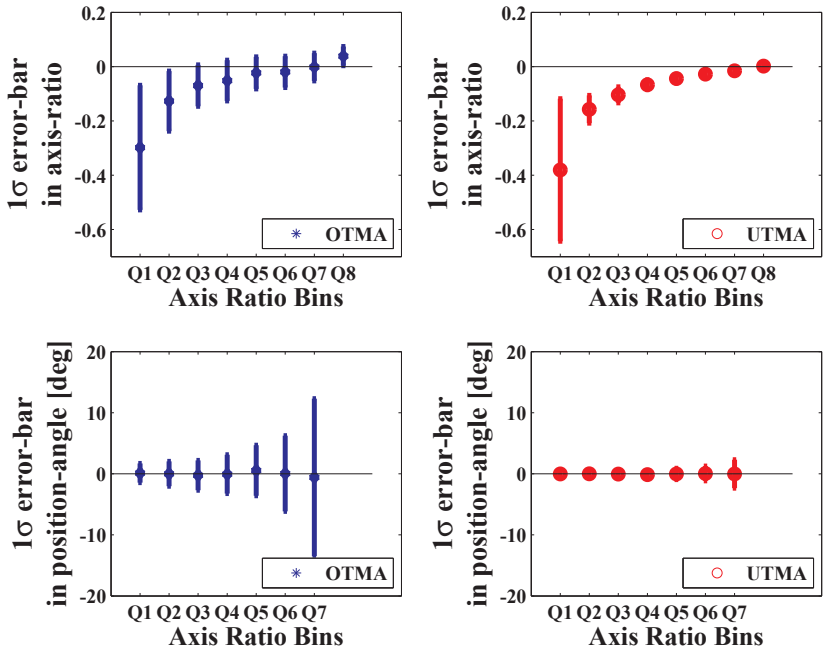

Figure III.4.4: **Error–bar plots for case study # 2 - pixel scale 0.1″:** The error-bar plots corresponding to case study #2 for axis ratio and position angle measurement. The simulated images have a pixel scale of 0.1″.

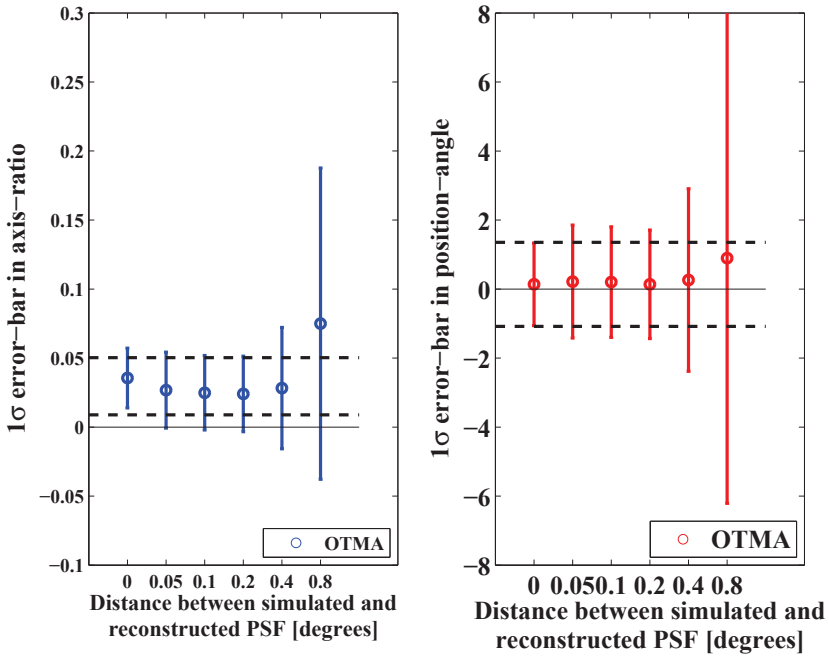

Figure III.4.5: **Error–bar plots for case study # 3 - pixel scale 0.025″:** The error-bar plot corresponding to case study #3 for axis ratio and position angle measurement. The images have a pixel scale of 0.025″. The dotted bounding line is the worst case error-bar for UTMA design.

Table III.4.5: The mean error and the 1σ error-bar for axis–ratio and position–angle measurement for case study #3

PSF distance*	Axis–ratio		Position–Angle	
[in degrees]	Mean error	1σ error-bar	Mean error	1σ error-bar
0.0	0.0355	0.0216	0.1374	1.1953
0.05	0.0267	0.0275	0.2167	1.6345
0.1	0.0248	0.0269	0.2018	1.6002
0.2	0.0240	0.0273	0.1377	1.5710
0.4	0.0282	0.0439	0.2596	2.6446
0.8	0.07496	0.1127	0.8968	7.1069

* Distance between the simulated PSF and reconstruted PSF

Chapter III.5

Discussions and Conclusion

We computed the precision with which both the OTMA and UTMA designs can measure weak lensing observables under various scenarios. In this chapter we present additional insight into the results obtained in the last chapter. We recall the questions we posed in section III.1.5 and answer them briefly at first and in detail if necessary.

III.5.1 Discussion of the Results

In the PSF, does the transfer of energy from the central disk to the outer rings affect precision measurement of weak lensing observables?

We use the results of case studies # 1 and # 3 to answer the above question. Both the OTMA and UTMA design measure the axis ratio and position angle of galaxies with the same precision if the reconstructed OTMA PSF is within 10 arcminutes of the point of interest. Therefore, the transfer of energy from the central disk to the outer rings do not affect the precision measurement of weak lensing observables, if the OTMA PSF is reconstructed accurately.

Does the presence of diffraction spikes in the PSF affect the precision measurement of weak lensing observables?

We again use the results of case studies # 1 and # 3 to answer the above question. If the diffraction spikes in the OTMA PSF are reconstructed within 10 arcminutes from the point of interest, both the OTMA and UTMA design measure weak lensing observables with same precision.

How does the uncertainty in the knowledge of PSF affect the precision measurement of weak lensing observables?

We use the results of case studies # 2 and # 3 to answer the above question. We showed in section III.2.5 that the PSFs of an OTMA design change over the field–of–view significantly when compared with a UTMA design. For the UTMA design the weak lensing observables can be measured with same precision no matter how far the reconstructed PSF is from the point of interest. For the OTMA design the precision suffers as the distance between the point of interest and the reconstructed PSF increases. The precision delivered by the OTMA design as the distance between the point of interest and the reconstructed PSF increases. We discuss the main reason for the variation of PSF over the field–of–view for the OTMA design in section III.5.1.1.

How does pixel scale of the images affect the measurement of weak lensing observables for both the OTMA and UTMA designs?

We simulated galaxy images with two pixel scales namely $0.025''$ and $0.1''$. The former pixel scale is equivalent to oversampling and the latter is Nyquist sampled. We find that we recover the axis ratio and position angle with desired precision in both pixel scales. For images with $0.1''$ pixel scale, there is a systematic error in the axis ratio measurements for slender galaxies. This systematics disappear as the galaxies become circular. Contemporary designs use pixel scales of the order $0.1''$ and this systematics should be addressed.

III.5.1.1 Encircled Energy Plots

Figure III.5.1 shows the EE plot at 2 different regions in the FOV for both the designs. These 2 regions correspond to the region of interest in the above case studies (labeled '1' and '11' in Figure III.2.3). The EE varies over the field–of–view for the OTMA design but it is uniform for the UTMA design. Since EE is a quantity derived from the PSF we can conclude that the PSF of the UTMA design is homogeneous over the entire field–of–view. The same is not true for the OTMA design.

The OTMA design studied here is only a representative of a family of OTMA designs (cf. section III.2.3). Therefore, one can argue that it is possible to design other OTMA telescopes that have uniformly same EE over the entire field–of–view. We assert that the presence of spider obstruction will not allow OTMA designs to have homogenous PSF over a wide FoV. We modeled the OTMA1 telescope in ZEMAX without the spider support structure and computed the EE at different FOV locations. The EE plot of this design without spider support is reasonably uniform over the entire FoV. Therefore, the spider support structure is the significant contributor to the inhomogeneity of the PSF. Hence, in theory the UTMA PSFs are homogenous over a wider FoV compared to OTMA PSFs.

III.5.1.2 PSF Reconstruction

For an OTMA design, the correlation between neighboring PSFs can be used to construct a metric, which tell us how the PSF varies over the FoV. If sufficient number of unsaturated point sources are available in the FoV, the PSF can be computed at any point with desired S/N for an OTMA design. In case of UTMA design the PSF is uniform over the FoV and hence the PSF can be extracted without extensive knowledge of the metric. In practice the PSF for OTMA design can be extracted with desired S/N if there are a sufficient number of unsaturated point sources in the full field. If the PSF is known with desirable SNR, then both the designs will measure the weak lensing observables with same precision as shown in case study #1.

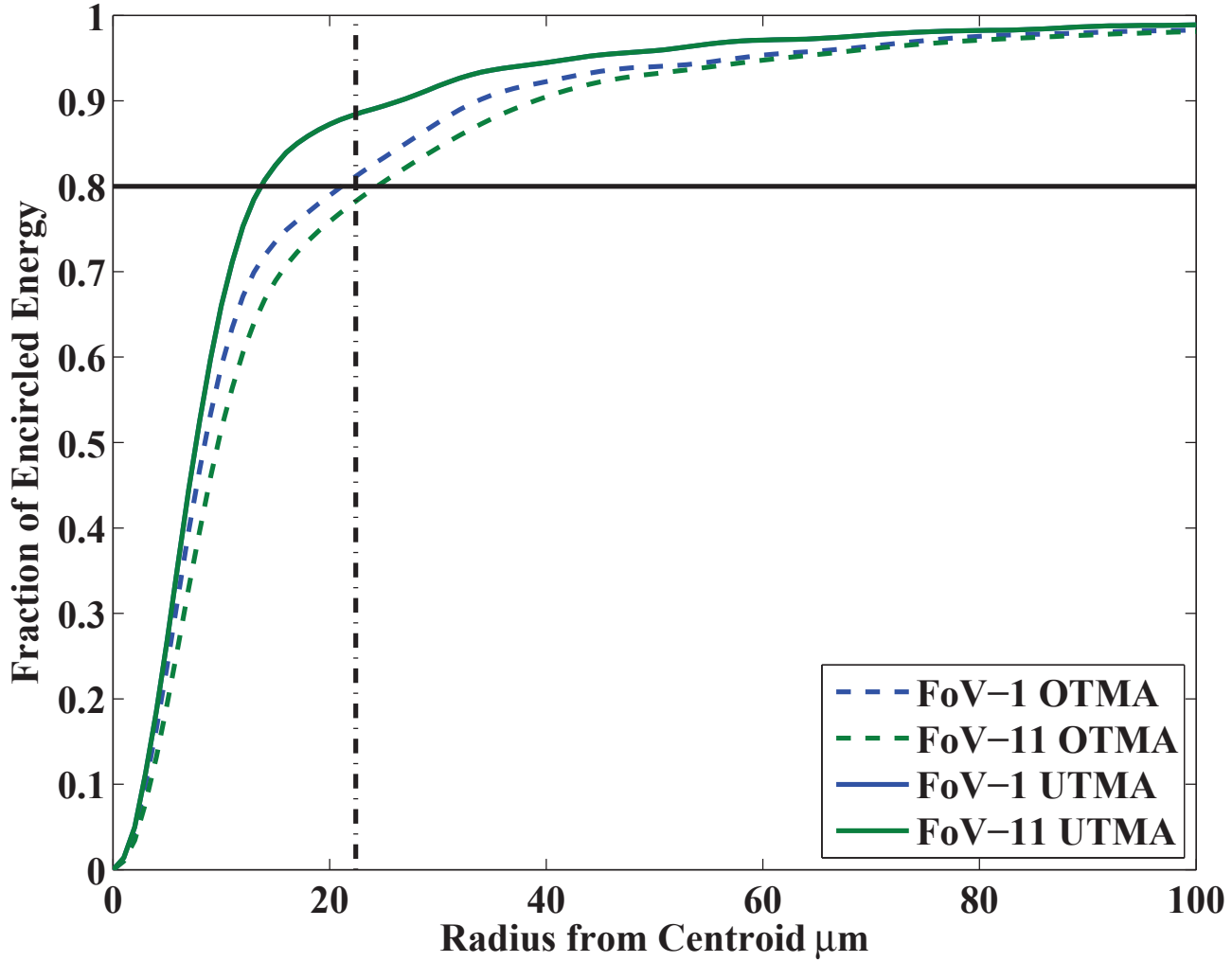

Figure III.5.1: **Encircled Energy plot at 2 different field–of–view locations for both the OTMA and UTMA design:** The EE plot is shown for the OTMA and the UTMA for 2 different FOV locations. The EE is calculated for wavelengths between 550 nm and 900 nm. The labels for the FOV correspond to the labels in Figure III.2.3. Lampton et al. (2010) have shown that the radius for EE = 80% level is greater for the OTMA design. We also show EE plot does not change for the UTMA design (solid line) over the FOV and it changes considerably for the OTMA design (dashed line).

III.5.1.3 Systematic Errors

In this study we did not include the following systematic errors because they affect both the OTMA and UTMA design in the same way. First, studies of the photometric evidence by King (1978) suggests that axis ratio and position angle change with isophotal radius in elliptical galaxies due to their triaxial nature. Second, studies by Voigt et al. (2012) show that the impact of color gradients, which are intrinsically present on the image can affect the morphology measurements. Third, studies by Rhodes et al. (2010) show that CTI effects are a dominant factor which affect the precision of aging CCDs. We assumed that these errors are not dominant compared to the PSF effects.

III.5.1.4 Tolerancing

Tolerancing or sensitivity analysis computes the change in a given property for a change in the constructional parameters. We do not perform a full scale tolerancing analysis to measure the change in the science results for tolerances in all the constructional parameters. Instead of such an exhaustive analysis, we did some defocussing to see how it affects the RMS wavefront error. For reasonable defocussing of $\pm$ 0.01 mm, both the designs show an RMS wavefront error less than 0.07 waves, which is the diffraction limit of the system. The sensitivity of the constructional parameters and the manufacturing and alignment errors will affect the PSFs of real telescopes.

III.5.2 Future Work

From the results obtained in out study we find that both the OTMA and UTMA designs will deliver similar precision when measuring weak lensing observables for a mission similar to *Euclid*. We believe the intrinsically homogeneous PSF of the UTMA design will be a better choice for other science missions like EChO (Tinetti et al., 2012) and SPICES (Boccaletti et al., 2012).

The methods we developed in this work to compare the OTMA and UTMA designs will serve as a good starting point for quantifying the performance of both

the designs for other science goals.

We also identified some critical challenges in constructing UTMA designs, which needs to be addressed from a theoretical stand point. First, we find the separation between the primary mirror and secondary mirror large for a UTMA design when compared with a OTMA design. Second, the pupil size of the tertiary mirror is large for a UTMA design when compared with a OTMA design. We would like to compute the theoretical limit on the separation between the primary and secondary mirror for a UTMA design and the relationship between the pupil size of the tertiary mirror and other design parameters. We note that these challenges arise only for designs with large effective focal length and wide field–of–view.

We would also like to study the tolerances in constructional parameters for the UTMA design to better understand the possibility of building a real working model. The tolerances for a UTMA design are believed to be tighter than that of an OTMA design.

III.5.3 Conclusion

We presented a simple method to design a UTMA telescope that is diffraction limited in the desired field–of–view. We find that the physical size of UTMA designs are larger than that of OTMA designs for a given pupil size and diffraction limited field–of–view.

We find that the OTMA PSF in spite of the presence of diffraction spikes or the transfer of energy to the outer rings measures axis ratio and position angle of galaxies with same precision as that of a UTMA design, if the PSF is reconstructed accurately. This implies that the intrinsic defects in the OTMA PSF do not affect its precision if the defects are known.

The PSF of UTMA design is uniform over the field–of–view when compared with that of a OTMA design. We showed that the variation of the OTMA PSF is due to the presence of the spider support structure. When measuring the axis ratio and position angle of galaxies if the reconstructed PSF is within 10 arc-minutes of the source, both the OTMA and UTMA designs measure with same precision. If the

reconstructed PSF is more than 10 arc-minutes from the source, the performance of the OTMA design begins to drop but the performance of the UTMA design remains the same.

From these results we conclude that for present day weak lensing missions obstructed TMA telescopes are sufficient to meet the science goals. The problem with the variation of OTMA PSF is overcome by studying the correlation between the PSFs at different regions in the field–of–view. Also at any given field in 0.6 degree squared there should be sufficient number of unsaturated stars to reconstruct the OTMA PSF with desired S/N. Hence, the weak lensing observables can be measured with desired precision using an OTMA design.

III.5.4 Conclusion en Français

Partie I

Dans ce travail, nous avons amélioré la méthode actuelle utilisée pour résoudre le problème inverse de modélisation des lentilles gravitationnelles simples. Nous modélisons paramétriquement à la fois les lentilles et les sources en même temps en utilisant l'inférence bayésienne.

Nous avons testé notre méthode sur des arcs gravitationnels simulés et avons été en mesure de récupérer les paramètres de la lentille et la source avec précision. Nous avons également appliqué notre méthode sur de véritables lentilles gravitationnelles brillantes extraites des bases de données SL2S et SLACS. Nous avons calculé les paramètres des lentilles et sources. Les résultats significatifs de l'étude sont les suivants:

Nous constatons que les modèles isothermes sont suffisants pour décrire la plupart des lentilles observées. Nous avons pu modéliser six des neuf lentilles du SL2S et SLACS que nous avons étudiés en utilisant soit un profil ellipsoïde isotherme non-singulier (NIE en anglais) ou une sphère isotherme non-singulière (NIS en anglais). Nous constatons que certains modèles nécessitent une quantité non négligeable de cisaillement externe pour expliquer les images observées.

Nous constatons également que le profil de la lumière de Sersic est adéquat pour décrire la plupart des sources magnifiées reconstruites.

En utilisant les paramètres calculés des lentilles, nous avons obtenu leur taille physique, leur vitesse de dispersion, leur masse totale à l'intérieur du rayon d'Einstein, leur masse de coeur et la fraction de matière sombre à l'intérieur du rayon d'Einstein.

Pour toutes les lentilles étudiées dans ce travail, environ 20±5% de la masse totale se trouve dans leur noyau. Nous trouvons que la fraction de la matière sombre comprise dans le rayon d'Einstein est de 0,2±0,08. Les sources que nous avons étudiés à grand redshift montrent toutes un profil de lumière exponentielle.

Partie II

Nous avons présenté une méthode simple pour concevoir un télescope TMA non-obstrué (UTMA) limité par la diffraction dans le champ de vision souhaité. Nous confirmons que la taille physique des designs UTMA est intrinsèquement plus grande que celle des designs classiques (TMA obstrué ou OTMA) pour une taille de pupille et de champ de vision donnés.

Nous constatons que les PSF des OTMA, en dépit de la présence de pics de diffraction et du transfert d'énergie vers les anneaux d'Airy, sont capables de mesurer les rapports axiaux et angle de position de galaxies faible avec autant de précision que les designs UTMA, si la PSF des OTMA est reconstituéer précisément. CEn d'autres termes, les défauts intrinsèques des PSF des OTMA n'affectent que marginalement la précision des mesures si les défauts sont bien quantifiés.

La PSF des designs UTMA est uniforme sur tout le champ de vision, contrairement aux OTMA. Nous avons montré que la variation de la PSF OTMA est principalement due à la présence de l'araignée de support du secondaire. Lors de la mesure de l'angle de position et rapport axiaux des galaxies, si la PSF OTMA est reconstruite à moins de 10 minutes d'arc de la source, les deux designs offrent des performances avec la même précision. Si la PSF est reconstruite à davantage que 10 minutes d'arc de la source, la performance des OTMA commence à diminuer, alors que la performance des UTMA reste la même.

De ces résultats, nous concluons que, pour les missions spatiales d'aujourd'hui, les télescope TMA obstruées sont suffisantes pour répondre aux objectifs scientifiques des mesures de lentilles faibles. Le problème avec la variation de la PSF OTMA est surmontée par la construction d'une PSF variable sur le champ de vision du plan focal et l'étude de la corrélation entre les PSF sur différentes régions dans le champ de vision. De plus, le nombre d'étoiles brillantes disponibles pour l'étalonnement de la PSF sera suffisant sur 0,6 degré carré. Par conséquent, l'effet de lentilles faibles peut être mesuré avec la précision requise avec un OTMA.

Appendices

Appendix A

Description of the MATLAB routines

The MATLAB[1] routines we wrote for lens modelling can be found at GITHUB. In this appendix we describe inputs and outputs the important top level routines. The routines we discuss in detail are the following.

simulateArc This routines allows the user to simulate gravitational arcs.

invertImageVerify This routine allows the user to reconstruct the source and the arcs for given set of lens parameters and an observed gravitational arc.

invertImageMCMC This routine computes the likelihood for randomly sampled lens parameters.

analysisMCMC This routine computes the posterior distribution for the lens and source parameters.

We describe the inputs and outputs for each of the routines below. If necessary we also describe some of the sub-routines we used.

[1] https://github.com/balaonspace/invertStrongLens–Matlab

A.1 Description of the High Level Routines

simulateArc

The inputs for this routine are the image characteristics, the lens parameters and the source parameters. The mean and standard deviation for the gaussian noise are optional. The output of the routine is the lensed images for the given lens and background source.

The image characteristics are

- pixsz – The pixel size in arcseconds.
- npix – The number of pixels in both the axis of the image. We only allow square images.

The lens parameters are entered in a array in the following order – The Einstein radius, the axis ratio, the core radius, the orientation of the lens, complex shear along first axis and the complex shear along second axis. For a detailed description of the parameters refer to section II.1.4. For a spherical lens the axis ratio $f = 1$ but we set the value as $1 - \epsilon$, because the equation to compute the deflection angle (equation II.1.16) is singular at $f = 1$.

The source parameters are entered in a array in the following order – The centroid of the source along first axis, the centroid of the source along second axis, radius of the source, effective radius of the source, ellipticity of the source and the position angle of the source. For a detailed description of the parameters refer to section II.1.5.

invertImageVerify

The inputs for this routine are the observed image, the arc image, psf (optional), mask image, the image characteristics, the lens parameters, the source parameters and the standard deviation of the noise in the image. The outputs of this routine are the reconstructed source, the reconstructed arcs and parameters related to them. The images are input in CSV format.

- observed image – The observed gravitational arc with the lensing galaxy and the obscure pixels masked.
- arc image – Pixels in the extracted arc.
- psf – The reconstructed arcs can be convolved with the PSF of the telescope.
- masked image – The image where the unmasked pixels are set to 0 and the masked pixels are set to any value greater than 0.

The remaining parameters are set similar to the above routine. This routine is used to visually see the reconstructed source and images for a given set of lens parameters.

invertImageMCMC

The inputs for this routine are the observed image, the arc image, psf (optional), mask image, the image characteristics, prior for the lens parameters, the standard deviation of the noise in the image and the number of samples for the prior.

If the lens parameters are constrained in the range $[a, b]$, the random samples are generated using

$$randomValue = a + (b - a) * rand(nsamples, 1) \tag{A.1}$$

The above command generates random numbers in the interval $[a, b]$, where a and b constrain the range for each lens parameter.

The outputs of this routine are the lens parameters sampled, the parameters of the reconstructed source, the chi-squared and summed square errors.

analysisMCMC

The inputs for this routine are the output files given by 'invertImageMCMC' and the number of chains in the MCMC process. The default number of chains is set at 100.

This implies the Metropolis–Hastings algorithm will run on the lens prior 100 times and each time a posterior is computed for the lens and source parameters. Since this algorithm depends on random numbers, we run this algorithm multiple times and the final values are the average of all the posteriors computed.

This routine also computes the dispersion velocity, the mass within the Einstein radius and the mass of the lens core.

Appendix B

List of Publications

The results obtained in part II of this thesis are awaiting publication. The results obtained in part III of this thesis were published in a refereed journal. The details of the publication are given below.

Title: Obstructed Telescopes Versus Unobstructed Telescopes for Wide Field Survey-A Quantitative Analysis
Télescope obstrués versus télescopes non-obstrués pour grands sondages du ciel: analyse quantitative

Authors: Singaravelu, Balasubramanian; Cabanac, Remi A.

Publication: Publications of the Astronomical Society of the Pacific, Volume 126, issue 938, pp.386-397

Publication Date: 04/2014

Astronomy Keywords: Astronomical Instrumentation

Abstract

Telescopes with unobstructed pupil are known to deliver clean point spread function (PSF) to their focal plane, in contrast to traditional telescopes with obstructed pupil. Recent progress in the manufacturing aspheric surfaces and mounting accuracy favors

unobstructed telescopes over obstructed telescopes for science cases that demand stable and clean PSF over the entire field–of–view. In this paper we compare the image quality of an unobstructed Three–Mirror–Anastigmat (TMA) design with that of an obstructed TMA. Both the designs have the same primary mirror, effective focal length, field–of–view and detector characteristics. We demonstrate using simulated images of faint elliptical galaxies imaged through the two designs, that both the designs can measure morphological parameters with same precision, if the PSF is reconstructed within 12 arc-minutes of the source. We also demonstrate that, the unobstructed design delivers desirable precision even if the PSF is reconstructed 50 arc-minutes away from the source. Therefore the PSF of unobstructed design is uniform over a wider field–of–view compared to an obstructed design. The precision of the designs is given by the 1σ error-bars (68% confidence level) in the fitted values of the axis–ratio and position–angle of the simulated galaxies.

Résumé article en français

Les télescopes avec pupille non-obstruée peuvent délivrer des fonctions d'étalement ponctuel (PSF) propre de leur plan focal, contrairement aux télescopes traditionnels avec pupille obstruée. Les récents progrès de fabrication et d'assemblage des surfaces asphériques favorisenten théorie les télescopes non-obstrués sur les télescopes obstruées pour les cas scientifiques qui exigent une PSF stable et propre sur tout le champ de vision. Dans cet article, nous comparons la qualité d'image d'un design anastigmatique à trois miroirs (TMA) non-obstrué, avec celle d'un TMA obstrué. Les deux modèles ont le même miroir primaire, la longueur focale effective, le même champ de vue et des détecteurs identiques. Nous démontrons en utilisant des images simulées de galaxies elliptiques faibles imagées par les deux modèles, que les deux modèles peuvent mesurer les paramètres morphologiques avec la même précision, dans le cas du TMA obstrué uniquement si la PSF est reconstruite dans les 12 minutes d'arc de la source. Nous démontrons également que, le design non-obstrué offre la même précision, même si la PSF est reconstruite à 50 minutes d'arc de la source parce que la PSF du design non-obstrué est uniforme sur un champ de vision plus

large par rapport au design obstrué. Les précisions optenues sur les rapports axiaux et les angles de positions des galaxies faibles sont présentées (enveloppes d'erreur de 1-sigma)1-sigma niveau de confiance de 68%.

Bibliography

Auger, M., Treu, T., and Bolton, A. (2009). The sloan lens acs survey. ix. colors, lensing, and stellar masses of early-type galaxies. *The Astrophysical Journal*, 705(2):1099–1115.

Auger, M., Treu, T., and Bolton, A. (2010). The sloan lens acs survey. x. stellar, dynamical, and total mass correlations of massive early-type galaxies. *The Astrophysical Journal*, 724(1):511–525.

Baker, J. G. (1969). On improving the effectiveness of large telescopes. *IEEE Trans. Aerosp. Electron. Syst.*, AES-5(2):261–272.

Bartelmann, M. and Schneider, P. (1996). Weak gravitational lensing. *Physics Reports*, 340(4-5):291–472.

Bertin, E. (2009). Skymaker: astronomical image simulations made easy. *Memorie della Societa Astronomica Italiana Supplement*, 80:422.

Bertin, E. and Arnouts, S. (1996). Sextractor: Software for source extraction. *Astronomy & Astrophysics Supplement*, 117:393–404.

Blanford, R. D. and Narayan, R. (1992). Cosmological applications of gravitational lensing. *Annu. Rev. Astron. Astrophysics*, 30.

Boccaletti, A., Schneider, J., and Traub, W. (2012). Spices: Spectro-polarimetric imaging and characterization of exoplanetary systems. *Experimental Astronomy*.

Bolton, A., Burles, S., and Koopmans, L. (2008). The sloan lens acs survey. v. the full acs strong-lens sample. *The Astrophysical Journal*, 682(2):964–984.

Bolton, A., Burles, S., Koopmans, L., Treu, T., and Moustakas, L. (2006). The sloan lens acs survey. i. a large spectroscopically selected sample of massive early-type lens galaxies. *The Astrophysical Journal*, 638(2):703–724.

Born, M. and Wolf, E. (1965). *Principles of Optics*. Pergamon, Bath.

Bourassa, R. and Kantowski, R. (1975). The theory of transparent gravitational lenses. *The Astrophysical Journal*, 195(1):13–21.

Brewer, B., Lewis, F., and Belokurov, V. (2012). Modelling of the complex cassowary/slugs gravitational lenses. *MNRAS*, 412(4):2521–2529.

Cabanac, R., Alard, C., and Dantel-Fort, M. (2007). The cfhtls strong lensing legacy survey. i. survey overview and t0002 release sample. *Astronomy and Astrophysics*, 461(3):813–821.

Chae, K., Khersonsky, V., and Turnshek, D. (1998). Gravitational lensing by power-law mass distributions: A fast and exact series approach. *The Astrophysical Journal*, 506(1):80–92.

Ciotti, L. (1991). Stellar systems following the r^1/m luminosity law. *Astronomy and Astrophysics*, 249(1):99–106.

Coles, J. (2008). A new estimate of the hubble time with improved modeling of gravitational lenses. *The Astrophysical Journal*, 679.

Cook, L. G. (1979). Three-mirror anastigmat used off-axis in aperture and field. *Proc. Soc. Photo-Opt. Instrum. Eng.*, 183:207–211.

Dalal, N. and Kochanek, C. (2002). Direct detection of cold dark matter substructure. *The Astrophysical Journal*, 572(1):25–33.

Dye, S. and Warren, S. J. (2005). Decomposition of the visible and dark matter in the einstein ring 0047-2808 by semilinear inversion. *The Astrophysical Journal*, 623(1):31–41.

Eigenbrod, A., Courbin, F., and Dye, S. (2005). Cosmograil i: How to sample the light curves of gravitationally lensed quasars to measure accurate time delays. *Astronomy and Astrophysics*, 436.

Einstein, A. (1936). Lens-like action of a star by the deviation of light in the gravitational field. *Science*, 84(2188):506–507.

Euclid Collaboration (2011). Euclid definition study report. *ESA/SRE*.

Fabbianno, G. (1989). X-rays from normal galaxies. *Annual review of astronomy and astrophysics*, 27.

Friedmann, A. (1924). ´Uber die m´oglichkeit einer welt mit konstanter negativer kr´ummung des raumes. *Zeitschrift f´ur Physik*, 21.

Gavazzi, R., Treu, T., and Koopmans, L. (2008). The sloan lens acs survey. vi. discovery and analysis of a double einstein ring. *The Astrophysical Journal*, 677(2):1046–1059.

Gavazzi, R., Treu, T., and Marshall, P. (2012). The sl2s galaxy-scale gravitational lens sample. i. the alignment of mass and light in massive early-type galaxies at z = 0.2-0.9. *The Astrophysical Journal*, 761(2):11pp.

Gavazzi, R., Treu, T., and Rhodes, J. (2007). The sloan lens acs survey. iv. the mass density profile of early-type galaxies out to 100 effective radii. *The Astrophysical Journal*, 667(1):176–190.

Gelman, A., Carlin, J., Stern, H., and Rubin, D. (1995). *Bayesian Data Analysis*. Chapman & Hall, Boca Raton.

Gorenstein, M. V., Shapiro, I. I., and Falco, E. E. (1988). Degeneracies in parameter estimates for models of gravitational lens systems. *Astrophysical Journal*, 327.

Hastings, W. K. (1969). Monte carlo sampling methods using markov chains and their applications. *Biometrika*, 57.

Hoekstra, H., Franx, M., and Kuijken, K. (2003). 2016+112: a gravitationally lensed type ii quasar. *MNRAS*, 340(2):609–622.

Hubble, E. (1929). A relation between distance and radial velocity among extra-galactic nebulae. *Proceedings of the National Academy of Sciences of the USA*, 15(3):168–173.

Jullo, E., kneib, J. P., Limousin, M., Eliasdottir, A., Marshall, P. J., and Verdugo, T. (2007). A bayesian approach to strong lensing modelling of galaxy clusters. *New Journal of Physics*, 9(12):447.

Keeton, C. (2001). A catalog of mass models for gravitational lensing. *arXiv:astro-ph/0102341v2*.

Keeton, C. (2010). On modeling galaxy-scale strong lens systems. *General Relativity and Gravitation*, 42(9):2151–2176.

Keeton, C., Kochanek, C., and Seljak, U. (1997). Shear and ellipticity in gravitational lenses. *The Astrophysical Journal*, 482(2):604–620.

Kim, J., Park, C., and Gott, J. (2009). The horizon run n-body simulation: Baryon acoustic oscillations and topology of large-scale structure of the universe. *The Astrophysical Journal*, 701(2):1547–1559.

King, I. R. (1978). Surface photometry of elliptical galaxies. *Astrophysical Journal*, 222:1–13.

Kochanek, C. (2004). *Gravitational Lensing: Strong, Weak & Micro Part II*. Springer-Verlag, Berlin.

Koopmans, L., Garret, M., and Blanford, R. (2002). 2016+112: a gravitationally lensed type ii quasar. *MNRAS*, 334.

Koopmans, L., Treu, T., Bolton, A., Scott, B., and Moustakas, L. (2006). The sloan lens acs survey. iii. the structure and formation of early-type galaxies and their evolution since z $\tilde{1}$. *The Astrophysical Journal*, 649(2):599–615.

Kormann, R., Schneider, P., and Bartelmann, M. (1994). Isothermal elliptical gravitational lens models. *Astronomy & Astrophysics*, 284.

Korsch, D. (1972). Closed form solution for three-mirror telescopes, corrected for spherical aberration, coma, astigmatism, and field curvature. *Appl. Opt.*, 11:2986–2987.

Korsch, D. (1980). Design and optimization technique for three-mirror telescopes. *Appl. Opt.*, 19:3640–3645.

Kostrzewa-Rutkowska, Z., Wyrzykowski, L., and Auger, M. (2014). The evolution of late-type galaxies from cassowary lensing systems. *MNRAS*, 441(4):3238–3248.

Lampton, M. L., Sholl, M. J., and Levi, M. E. (2010). Na. *Proc. SPIE*, 7731.

Leinert, C., Bowyer, S., Haikala, L. K., and Hanner, M. S. (1998). The 1997 reference of diffuse night sky brightness. *Astronomy & Astrophysics Supplement*, 127:1–99.

Lemaître, G. (1927). Un univers homogène de masse constante et de rayon croissant rendant compte de la vitesse radiale des nébuleuses extragalactiques. *Annals of the Scientific Society of Brussels*, 47A.

Lemaître, G. (1933). L'univers en expansion. *Annals of the Scientific Society of Brussels*, A53.

Levi, M. E., Lampton, M. L., and Sholl, M. J. (2011). Na. *BAAS*, 43.

Limousin, M., Cabanac, R., Gavazzi, R., Jullo, E., and Kneib, J. (2009). A new window of exploration in the mass spectrum: strong lensing by galaxy groups in the sl2s. *Astronomy & Astrophysics*, 502.

Lynds, R. and Petrosian, V. (1986). Giant luminous arcs in galaxy clusters. *Bulletin of the American Astronomical Society*, 18.

Mandelbaum, R., Seljak, U., and Kauffmann, G. (2006). Galaxy halo masses and satellite fractions from galaxy-galaxy lensing in the sloan digital sky survey: stellar mass, luminosity, morphology and environment dependencies. *Monthly Notices of the Royal Astronomical Society*, 368(2):715–731.

Metropolis, N., Rosenbluth, A. W., Rosenbluth, M. N., Teller, A. H., and Teller, E. (1953). Equation of state calculations by fast computing machines. *Journal of Chemical Physics*, 21.

More, A., Cabanac, R., and More, S. (2012). The cfhtls-strong lensing legacy survey (sl2s): Investigating the group-scale lenses with the sarcs sample. *The Astrophysical Journal*, 749(1):19pp.

Newbury, P. R. and Spiteri, R. J. (2002). Inverting gravitational lenses. *SIAM Review*, 44.

Parker, L., Hoekestra, H., and Hudson, M. (2007). The masses and shapes of dark matter halos from galaxy-galaxy lensing in the cfht legacy survey. *The Astrophysical Journal*, 669(1):21–31.

Paul, M. (1935). Inverting gravitational lenses. *Revue d'Optique Theorique et Instrumentale*, 14(5):169–202.

Peebles, P. (1993). *Principles of Physical Cosmology*. Princeton University Press, Princeton.

Peng, C. Y., Ho, L. C., Impey, C. D., and Rix, H. W. (2010). Detailed decomposition of galaxy images. ii. beyond axisymmetric models. *Astronomical Journal*, 139(5):2097–2129.

Penzias, A. and Wilson, R. (1964). A measurement of excess antenna temperature at 4080 mc/s. *The Astrophysical Journal*, 142.

Perlmutter, S., Aldering, G., and Goldhaber, G. (1999). Measurements of ω and λ from 42 high-redshift supernovae. *The Astrophysical Journal*, 517(2):565–586.

Perryman, M. A. C. (2005). Na. *Proc. GAIA Symposium ESA*, 576:15–22.

Planck Collaboration (2014). Plank intermediate results. xvi. profile likelihoods for cosmological parameters. *Astronomy & Astrophysics*, 5666(A54):10pp.

Refsdal, S. (1964). The gravitational lens effect. *MNRAS*, 128.

Rhodes, J., Leauthaud, A., Stoughton, C., and Massey, R. (2010). The effects of charge transfer inefficiency (cti) on galaxy shape measurements. *PASP*, 122:439.

Riess, A., Filippenko, A., and Challis, P. (1998). Observational evidence from supernovae for an accelerating universe and a cosmological constant. *The Astronomical Journal*, 116(3):1009–1038.

Rix, H., de Zeeuw, P., and Cretton, N. (1997). Dynamical modeling of velocity profiles: The dark halo around the elliptical galaxy ngc 2434. *The Astrophysical Journal*, 488(2):702–719.

Robb, P. N. (1978). Three-mirror telescopes: design and optimization. *Appl. Opt.*, 17:2677–2685.

Rubin, V. and Ford, W. (1970). Rotation of the andromeda nebula from a spectroscopic survey of emission regions. *The Astrophysical Journal*, 159.

Rubin, V., Ford, W., and Thonnard, N. (1980). Rotational properties of 21 sc galaxies with a large range of luminosities and radii, from ngc 4605 (r = 4kpc) to ugc 2885 (r = 122 kpc). *The Astrophysical Journal*, 238.

Ruff, A., Gavazzi, R., and Marshall, P. (2011). The sl2s galaxy-scale lens sample. ii. cosmic evolution of dark and luminous mass in early-type galaxies. *The Astrohysical Journal*, 727(2):20pp.

Saha, P. and Williams, L. (1997). Non-parametric reconstruction of the galaxy lens in pg 1115+080. *Monthly Notices of the Royal Astronomical Society*, 292.

Scarlata, C., Carollo, C., and Lilly, S. (2007). Cosmos morphological classification with the zurich estimator of structural types (zest) and the evolution since z = 1 of the luminosity function of early, disk, and irregular galaxies. *The Astrophysical Journal Supplement Series*, 172(1):406–433.

Schneider, P., Ehlers, J., and Falco, E. (1992). *Gravitational Lensing*. Springer-Verlag, Berlin.

Schroeder, D. J. (1987). *Astronomical Optics*. Academic Press, San Diego.

Serabyn, E., Mawet, D., and Burruss, R. (2010). An image of an exoplanet separated by two diffraction beamwidths from a star. *Nature*, 464:1018–1020.

Sérsic, J. (1963). Influence of the atmospheric and instrumental dispersion on the brightness distribution in a galaxy. *Boletin de la Asociacion Argentina de Astronomia*, 6.

Sonnerfeld, A., Gavazzi, R., Suyu, S., Treu, T., and Marshall, P. (2013a). The sl2s galaxy-scale lens sample. iii. lens models, surface photometry, and stellar masses for the final sample. *The Astrophysical Journal*, 777(2):13pp.

Sonnerfeld, A., Treu, T., Gavazzi, R., Suyu, S., and Marshall, P. (2013b). The sl2s galaxy-scale lens sample. iv. the dependence of the total mass density profile of early-type galaxies on redshift, stellar mass, and size. *The Astrophysical Journal*, 777(2):15pp.

Soucail, G. (1987). Observations des arcs dans les amas de galaxies: mise en évidence d'un mirage gravitationnel dans abell 370. *Journal des Astronomes Francais*.

Springel, V., White, S., and Jenkins, A. (2005). Simulations of the formation, evolution and clustering of galaxies and quasars. *Nature*, 435(7042):629–636.

Suyu, S. H., Marshall, P. J., Hobson, M. P., and Blanford, R. D. (2006). A bayesian analysis of regularized source inversions in gravitational lensing. *MNRAS*, 371(2):983–998.

Taylor, C. A. and Thompson, B. J. (1958). Attempt to investigate experimentally the intensity distribution near the focus in the error-free diffraction patterns of circular and annular apertures. *JOSA*, 48:844–846.

Tinetti, G., Beaulieu, J. P., Henning, T., and Meyer, M. (2012). Echo - exoplanet characterisation observatory. *Experimental Astronomy*, 34:311–353.

Treu, T. (2010). Strong lensing by galaxies. *Annual Review of Astronomy and Astrophysics*, 48.

Treu, T., Gavazzi, R., and Gorecki, A. (2009). The slacs survey. viii. the relation between environment and internal structure of early-type galaxies. *The Astrophysical Journal*, 690(1):670–682.

Treu, T. and Koopmans, L. (2002). The internal structure and formation of early-type galaxies: The gravitational lens system mg 2016+112 at z = 1.004. *The Astrophysical Journal*, 575(1):87–94.

Treu, T. and Koopmans, L. (2004). Massive dark matter halos and evolution of early-type galaxies to z $\tilde{1}$. *The Astrophysical Journal*, 611(2):739–760.

Treu, T., Koopmans, L., Bolton, A., Brules, S., and Moustakas, L. (2006). The sloan lens acs survey. ii. stellar populations and internal structure of early-type lens galaxies. *The Astrophysical Journal*, 640(2):662–672.

Trujillo, I., Erwin, P., Asensio, A., and Graham, W. (2004). Evidence for a new elliptical-galaxy paradigm: Srsic and core galaxies. *The Astrophysical Journal*, 127(4):1917–1942.

Tu, H., Gavazzi, R., and Limousin, M. (2009). The mass profile of early-type galaxies in overdense environments: the case of the double source-plane gravitational lens sl2sj02176-0513. *Astronomy & Astrophysics*, 501(2):475–484.

Tyson, J., Wenk, R., and Valdes, E. (1990). Detection of systematic gravitational lens galaxy image alignments - mapping dark matter in galaxy clusters. *Astrophysical Journal*, 349.

Voigt, L. M., Bridle, S. L., Amara, A., Cropper, M., and Kitching, T. D. (2012). The impact of galaxy colour gradients on cosmic shear measurement. *MNRAS*, 421:1385–1398.

Walsh, D., Carswell, R. F., and Weymann, R. J. (1979). 0957 + 561 a, b: twin quasistellar objects or gravitational lens? *Nature*, 279.

Zwicky, F. (1937). On the masses of nebulae and of clusters of nebulae. *Astrophysical Journal*, 86.